University of Bucharest
Faculty of Physics
Doctoral School of Physics

Nicolae Filipoiu

Modeling Hybrid Perovskite Materials and Dynamic Behaviour of Perovskite Solar Cells

Doctoral Thesis

Scientific Coordinator

Prof. Dr. George Alexandru Nemnes

Bucharest, 2024

Acknowledgements

The three-year journey of my PhD passed so quickly, and I realize now that I haven't expressed enough gratitude for this incredible experience. Therefore, I want to take this opportunity to acknowledge the support and trust I have received, both professionally and personally.

There are many people and things to be grateful for, but I will start by expressing my deepest thanks to my supervisor, Professor George Alexandru Nemnes. Words cannot properly extend my profound gratitude for your wisdom, guidance and endless patience. Your mentorship has been instrumental in shaping this work and I am forever indebted to you.

I am also thankful to all the members of the PERLA project team (both experimentalists and theoreticians) who offered me the opportunity to contribute to the research on perovskite solar cells. I would like to extend special thanks to Professor Andrei Manolescu from Reykjavík University in Iceland for his mentorship and guidance, as well as for the two wonderful months I spent in Iceland. The fruitful collaboration during the project has been invaluable.

There are many other scientists, professors and friends I should mention, but due to space limitations, please do not feel disappointed if you are not mentioned here. You will always remain in my thoughts, and I deeply value your friendship and expertise.

On a personal note, I must acknowledge my partner, Diana, for the immense support and for always being there for me. Thank you for being my pillar of strength throughout this stage of our life.

I am also grateful for the support and encouragement I received from my parents, sisters, and other family members, with special thanks to my beautiful and intelligent nieces, Maria and Theodora.

Abstract

This study presents a comprehensive investigation into the optoelectronic properties, stability and performance of quasi-2D perovskites and perovskite solar cells (PSCs) through a combination of *ab initio* calculations, equivalent circuit modeling and device simulation. Our findings reveal that the electronic structure and stability of quasi-2D perovskites are significantly influenced by the choice of halogens and large alkylammonium cations, with band gaps increasing as the halogen atomic number decreases. Although quantum confinement in 2D perovskites leads to larger-than-optimal band gaps, bromine and chlorine-based perovskites demonstrate enhanced stability, suggesting that an optimal mixture of halogens and cations could balance efficiency and stability. Additionally, our circuit model effectively reproduces the capacitive and inductive effects observed in PSCs, offering a bridge between charge accumulation and charge collection models. We introduced a dynamical electrical model and linked both capacitive and inductive effects to recombination mechanisms of the photogenerated carriers. Finally, our analysis of PSCs with Cu_2O as the inorganic hole transport layer (HTL) identified critical vacancy defects that influence device performance, with SCAPS simulations emphasizing the importance of passivating specific vacancies to mitigate unintentional doping. This study provides key insights for optimizing the design and performance of perovskite-based solar technologies.

Abbreviations

PSC - Perovskite Solar Cell
PCE - Power Conversion Efficiency
SCAPS - Solar Cell Capacitance Simulator
PRV - Perovskite
HTL - Hole Transporter Layer
ETL - Electron Transporter Layer
DFT - Density Functional Theory
DOS - Density of States
PDOS - Partial Density of State
MAPI - Methylammonium Three Iodide Plumbate
MA - Methylammonium
MD - Molecular Dynamic
RP - Ruddlesden-Popper
DJ - Dion-Jacobson
ML - Machine Learning
J-V - Current Density-Voltage
DEM - Dynamic Electrical Model
m-DEM - multiscale Dynamic Electrical Model
SPM - Surface Polarization Model
EIS - Electrochemical Impedance Spectroscopy
SIESTA - Spanish Initiative for Electronic Simulations with Thousands of Atoms
LDA - Local Density Approximation
LSDA -Local Spin Density Approximation
GGA - Generalized-Gradient-Corrections
FTO - Fluorine doped tin oxide
ITO - Tin-doped indium oxide
CA - Charge Accumulation
CC - Charge Collection
IV - Current Voltage Simulations
CV - Capacitance Voltage Simulations

BA - Butylammonium
PA - Pentylammonium
HXA - Hexylammonium
FA - Formamidinium
EA - Ethylammonium
GA - Guanidinium
DZP - Double-Zeta Polarized
CB - Conduction Band
VB - Valence Band
R-F - Reverse-Forward Measurements
NM - Nelder-Mead
R-C - Resistor-Capacitor
IDL - Interface Defect Layers

Contents

Introduction

Contemporary society is increasingly focused on transitioning to a more sustainable and resilient energy system which offers numerous benefits for the environment, economy and overall individual well-being. In order to achieve this goal, there is an increasing demand for the production of green and renewable energy. Although the green energy and renewable energy are usually considered synonyms, the renewable energy stands for energy generated from natural sources which regenerate faster than the consume rate. While, on the other hand, the green or clean energy stands for energy produced from sources with zero pollution (CO_2) during the utilization or production of these sources.

According to H. Ritchie and P. Rosado (2020) [1], the global carbon dioxide emission (CO_2) is directly linked to the world electricity consumption. For this reason, the global mix of electricity production is transitioning towards low carbon sources driven by policy measures, technological advancements and increasing awareness of climate change. Based on these aspects, the world electricity production sources can be divided in two categories: high emitting CO_2 sources (coal, gas and oil) and the low carbon emission sources (hydropower, nuclear, wind, solar, bioenergy and other renewable). At the moment, high carbon sources are still controlling the global mix of electricity by producing more than 80% of the world energy.

Among the low carbon emission sources, the solar energy is abundant and renewable, as it relies on the sun which is an inexhaustible source of energy. Furthermore, solar power is environmentally friendly, as it does not emit harmful greenhouse gases or pollutants into the atmosphere during operation. By enabling on-site generation, solar cells reduce the need for extensive energy distribution infrastructure, making energy production more efficient and cost-effective. Lastly, solar energy enhances energy security by reducing dependence on imported fossil fuels, contributing to a more resilient energy system [2]. The global solar energy production increased with 5% [3] over the last decade and can be correlated with the global CO_2 decrease presented at the top of Figure 1.1.

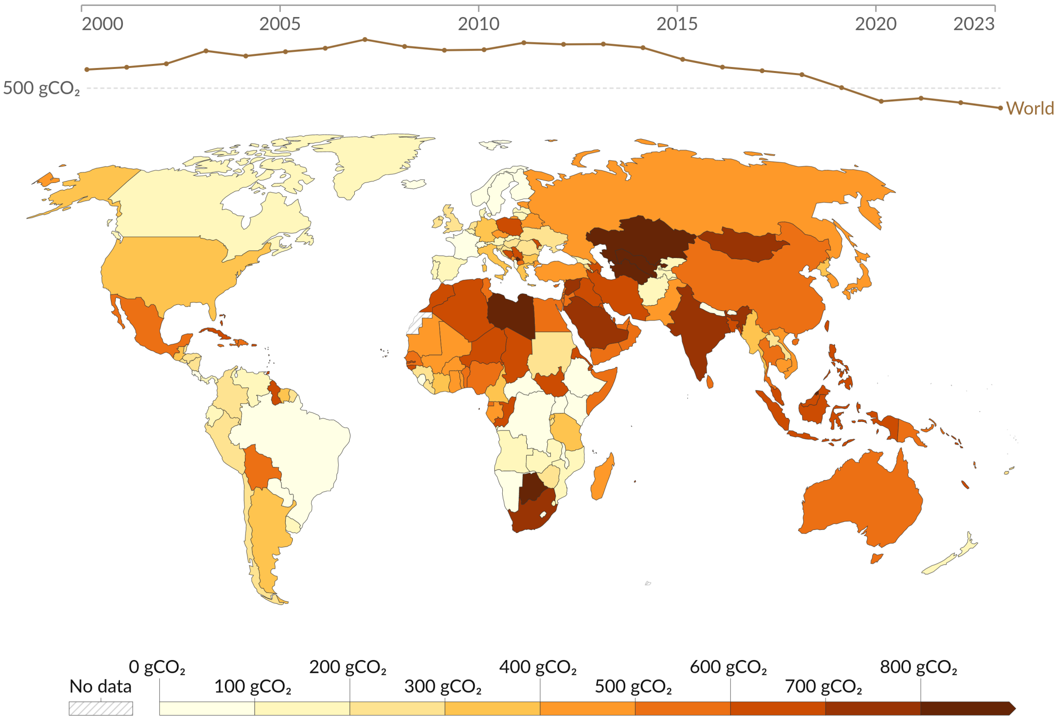

Figure 1.1: Global Carbon intensity map in grams of carbon dioxide-equivalents emitted per kilowatt-hour of electricity (for the year of 2023). At the top of the figure is depicted the CO$_2$ evolution over the last decades. Reproduced with permission from [1], based on the original data of Ember (2024); Energy Institute - Statistical Review of World Energy (2024).

Solar cells are crucial for renewable energy production for several reasons. Firstly, they serve as the primary technology for converting solar energy into electricity. Secondly, they are highly scalable, suitable for deployment in sizes ranging from small residential setups to large utility-scale projects [4]. Additionally, they can be incorporated into building materials, providing versatility in design and construction [5]. Solar cells can also be smoothly integrated into existing electricity grids, improving grid stability and reliability [6]. Continuous technological advancements through focused research and development efforts have consistently enhanced the efficiency and effectiveness of solar cells.

In the solar cell industry, the research is divided among six photovoltaic technologies, comprised of multijunction cells [7, 8], single junction GaAs [9], crystalline Si cells [10], thin-film technologies[11, 12], hybrid tandems [13] and perovskite solar cells [14, 15]. Among these, perovskite solar cells (PSC) have attracted the highest research focus, being considered the future generation of solar cells. Ongoing research aims to improve their stability and reduce production costs. In recent years, efforts have concentrated on commercial viability, with researchers achieving efficiencies over 25% in laboratory settings [16].

1.1 Background and Motivation

The calcium titanium oxide mineral ($CaTiO_3$) discovered by Gustav Rose in 1839 in the Ural Mountains was the first documented perovskite material [17]. Since then, any material with an ABX_3 chemical formula was associated with the perovskite structure. Among the perovskite materials, there are many important constituents such as $BaTiO_3$; $SrTiO_3$; $PbTiO_3$; $LaAlO_3$ and $RuTiO_3$, with applications ranging from: capacitors [18], gas sensors [19], photocatalysis [20], ceramics [21] and ferroelectric devices [22, 23].

In correspondence to the perovskite crystalline structure, emerged a new class of hybrid organic-inorganic halide perovskite materials. The typical ABX_3 site positions of the cell contains one A cation, one B cation and three X anions arranged in a specific geometry (Figure 1.2): A site position, in the center of the cube, is occupied by organic cations (methylammonium or formamidinium); B site, on the corners of the cube, is occupied by metallic cations (normally lead or tin) and on the X sites positions are typically anionic halogens (usually I, Br, Cl).

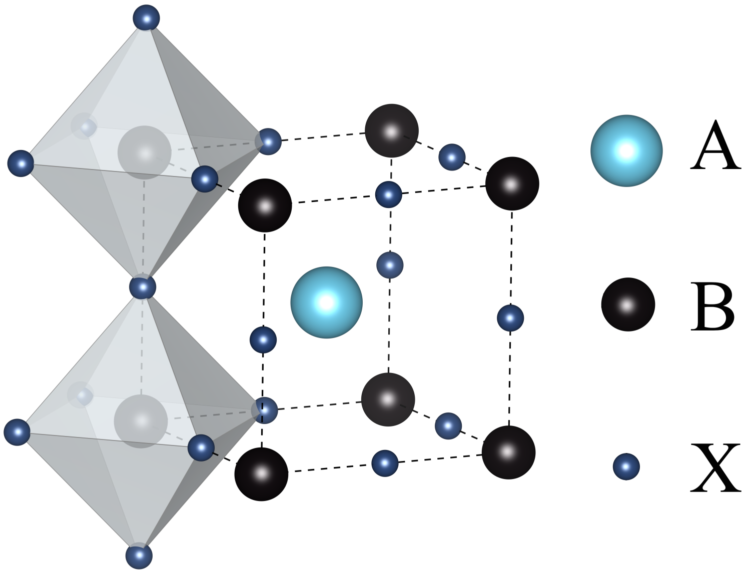

Figure 1.2: The ABX_3 organo-halide perovskite structure, where A is an organic cation(ex: CH_3NH_3), B is a metallic cation (ex: Pb) and X anion is a halogen (ex: I/Br/Cl).

In 2009, professor Tsutomu Miyasaka and his team from the Toin University of Yokohama Japan measured a power conversion efficiency (PCE) of 3.8% [24]. They have used the methylammonium lead iodide ($CH_3NH_3PbI_3$) as the light-harvesting layer in the photovoltaic cell, this way demonstrating that hybrid organic-inorganic lead halide perovskite material could efficiently convert sunlight into electricity, starting the competition with the performance of traditional silicon solar cells.

Nowadays, organo-halide perovskite solar cells (PSCs) are regarded as one of the most promising technologies in the field of photovoltaics [25, 26]. Tandem PSCs overpassed the classical silicon solar cells efficiencies locating themselves at 29% [27]. All these remarkable results are a consequence of the excellent optoelectronic properties of organo-halide perovskites, which include high absorption coefficients [28], long carrier diffusion lengths [29] and high charge carrier mobilities [30, 31]

A key advantage of PSCs is their solution procesability, the perovskite can be deposited from solutions [32], enabling low-cost and scalable manufacturing processes compared to traditional silicon-based solar cells, which require high-temperature and energy-intensive processing techniques. Another advantage is their tunable bandgap [33], by changing the composition of the perovskite material (organic molecules, metallic or halide species), researchers can adjust its optoelectronic properties to better match the solar spectrum [34], leading to enhanced light absorption and improved device performance.

PSCs have emerged as a promising photovoltaic technology because of their high efficiency, low-cost fabrication and scalability potential. However, they face several challenges that need to be addressed for widespread commercialization. Improving the stability of PSCs over time can be achieved by overcoming these challenges. Solutions include encapsulation to protect against moisture and other environmental factors, as well as optimizing device fabrication processes.

The main cause of perovskite material degradation is the ionic migration. PSCs generally contain several types of ions, including organic cations (methylammonium or formamidinium) and inorganic halide anions (such as iodide or bromide). These ions can migrate within the perovskite layer due to external factors like temperature, electric fields or illumination. This movement can result in undesirable effects such as doping, hysteresis or degradation.

Dynamic hysteresis effects are present in the current-voltage characteristics of all PSCs, leading to discrepancies in performance measurements depending on the direction of the voltage sweep [35]. To accurately characterize and optimize PSCs for practical applications, it is essential to understand and mitigate these dynamic hysteresis effects. Additionally, reducing ionic migration in perovskite solar cells requires engineering the composition and structure of perovskite materials, as well as interface engineering within the charge transporter layers. Given the complexity of the systems and materials involved, analyzing and characterizing the dynamic processes and PSCs devices are best achieved through a combined approach of computational calculations and *ab initio* techniques.

1.2 Objectives of the Study

This thesis is constructed around three principal goals: materials characterization, PSCs dynamic hysteresis effect calculations and PSC device simulations.

The materials characterization goal is comprised from simulation, characterization and optimizations of 2D or 3D materials of the perovskite interfaces. The central objectives for the materials characterization are:

- implement *ab initio* techniques (using the SIESTA code);
- perform geometrical relaxation of the structures (2D and 3D);
- optimize the electronic band structures (use DFT+U if required);
- employ materials structure engineering techniques (cations, halogens, vacancies);
- stability assessment (using the formation energy).

For reproducing the typical J-V hysteresis dynamic effect of PSCs, we set the following objectives:

- introduce a new dynamic hysteretic model (using simple electrical circuit elements);
- perform large signal analysis using the m-DEM simulations;
- introduce parameters calibration techniques for simulating the J-V characteristics;
- perform small signal analysis using the m-DEM model;
- investigate and explain the capacitive and inductive effects.

The PSC device simulation was achieved with the help of the SCAPS simulation program based on the DFT results provided by the SIESTA code when calculating the point defect influence on the (PDOS) band alignment of the two PRV interfaces. Therefore, the main objectives are:

- interface reconstruction (PRV-HTL, PRV-ETL) using DFT;
- analyze vacancy effects on the interfacial band alignment;
- perform SCAPS calculations on the reference PSC;
- for the band alignment observed with DFT introduce the corresponding effect in SCAPS using the IDLs;
- assess the device performance using the typical PSC parameters.

1.3 Structure of the Thesis

A seven-chapter architecture was chosen to present the results of the calculations. The thesis combines three computational methods with the goal to analyze the constituent materials of a PSC and to understand the peculiar dynamic behaviour of these new class of photovoltaic cells.

The first chapter provides the context of the research, including the importance of the study and the underlying reasons for conducting it. The second chapter introduces the first principles studies relevant to the research topic and reveal the explorations performed so far, related to the capacitive and inductive effects, which are foundational to understanding the phenomena investigated in the thesis.

The third chapter contains the theoretical details required for performing: material characterization, dynamic effect exploration and device simulations. These three goals will be incorporated in the results provided in chapters 4, 5 and 6.

Chapter four presents the *ab initio* investigation of the perovskite materials and interfaces. The electronic properties of layered perovskites (2D) combined with the stability assessment are followed by the interfaces analysis of the PRV-ETL and PRV-HTL and their constituent materials.

In chapter five, the results are based on a new equivalent circuit model to simulate the dynamic hysteresis effect of a PSC. This way, the large signal and small signal analysis are performed and the relevance of capacitive and inductive effects is discussed.

The device modeling and simulations of a PSC is completed in chapter six, where the SCAPS program is used in concordance with the DFT results from chapter four. The last chapter summarizes the findings of the research and discusses their implications, along with potential directions for future research.

Theoretical Background

In perovskite solar cells (PSCs), there are three key components: the active layer (PRV), the hole transporter layer (HTL) and the electron transporter layer (ETL). During the illumination, the main processes which occur inside the solar cell are: charge generation, charge separation, charge transport, charge collection and charge recombination (Figure 2.1).

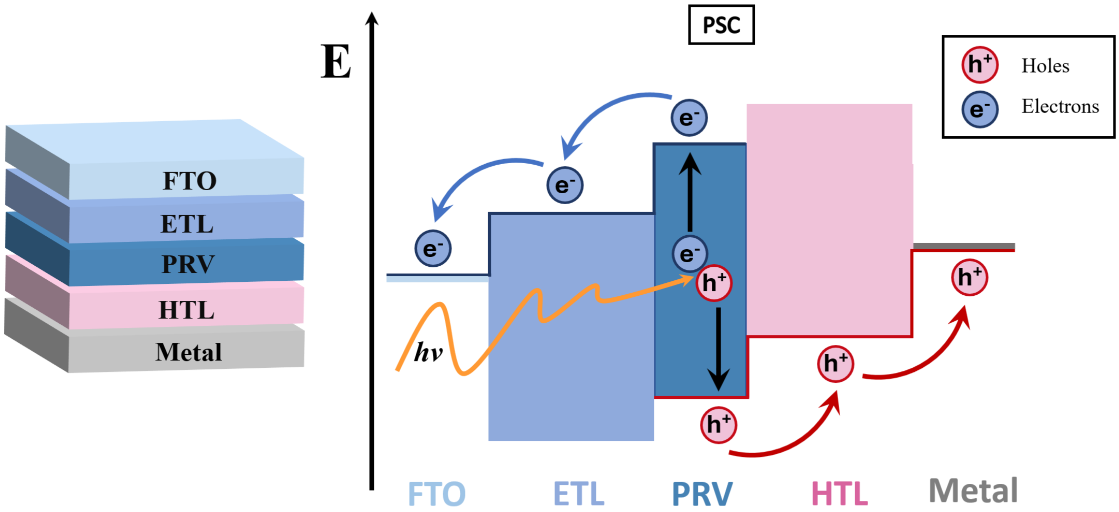

Figure 2.1: The working principle of an organo-halide perovskite structure, showing the processes which occur inside the solar cell during the illumination: charge generation, charge separation, charge transport, charge collection and charge recombination.

The perovskite active layer absorbs photons and generates electron-hole pairs, a process known as charge generation. The following process is charge separation, which occurs at the ETL-PRV and HTL-PRV interfaces. The separated electrons are injected into the ETL and then move toward the transparent electrode. Simultaneously, the holes are injected into the HTL and collected at the metallic contact. This separation and collection of electrons and holes at their respective electrodes generate an electrical current in the load resistance. The electrons flow through the external circuit, which can be used to power electronic devices or charge batteries. Finally, the recombination of electrons and holes occurs at the counter electrode, completing the electric circuit.

The performance of perovskite solar cells (PSCs) can be significantly influenced by their device architecture. Depending on which transporting layer (electron or hole) is closer to the incident light surface, PSCs are classified as either p-i-n (inverted PSCs) or n-i-p (regular PSCs). The n-i-p architecture is the most common and extensively studied configuration.

Additionally, considering that perovskite materials can be deposited either on mesoporous or in planar layers, these two architectures can be further subdivided into four distinct configurations. Moreover, due to the properties of perovskite materials, some studies have experimented with removing one of the transporter layers from the PSC architecture, resulting in two more configurations.

2.1 *Ab initio* Studies

First principle approaches can enhance the material performance in a device and the optoelectronic applications. By replicating the ground state of the material, fundamental properties can be obtained using the density functional theory (DFT). These include electronic properties such as the band gap magnitude and type, the band structure, density of states (DOS) and device band alignment through partial density of states (PDOS) analysis of the device interfaces.

At first, the $CH_3NH_3PbI_3$ (MAPI) perovskite refueled an old and appealing idea of a ferroelectric material used for solar cell applications [36], where the ferroelectric material provides the ideal conditions for charge separation (holes and electrons) due to the built-in electric field. When used as a photo-active material, the MAPI perovskite was considered as a ferroelectric absorber due to the high mobility of the free charge, with free paths exceeding 1 μm. For this reason, first studies considered that methylammonium (MA) electric dipole was a potential source for the ferroelectric behaviour. When the local polarization in hybrid perovskites was measured using piezoforce microscopy, it was revealed that ferroelectric domains are present and their size is comparable to the grain size of the MAPI layer.

By using first principles calculations, some studies investigated the ferroelectric polarization of hybrid MAPI perovskite. They found a small ferroelectric polarization of approximately 4.42 $\mu C/cm^2$ in Ref. [37] and approximately 8 $\mu C/cm^2$ in Ref. [38]. In a combined DFT and molecular dynamic (MD) study, Frost *et al.* (2014) studied the implication of ferroelectric contributions to the anomalous hysteretic effects, suggesting that local ferroelectric domains are influencing the electron-hole recombination, this way affecting the dynamic density current (J-V) measurements[39].

Goehry *et al.* (2015) excluded the hypothesis of macroscopic ferroelectricity by showing that the correlated motion of electric dipoles is of the order of tens of picoseconds [40]. The authors revealed that the rotation of the organic cations is correlated with the Pb-I cage deformation, which may lead to microscopic domains. Although the small ferroelectric domains are restricted to a limited space and time, they may still induce a beneficial charge separation.

Due to the versatility of the computational calculations, many recent studies focused on the layered 2D organo-halide perovskites [41]. Their key advantage stems from the organic component replacement, which revealed the opportunity of tuning the optoelectronic properties [42, 43]. Layered halide perovskites (2D) are regarded as natural multiple-quantum-wells [44] where the semiconducting inorganic layers act as potential "wells" and the organic insulating layer acts as potential "barriers". These layered structures are expected to be more stable[45] and induce higher exciton binding energys.

The embedded approach outlined in many studies of 2D perovskites while using *ab initio* methods is to produce the layered structure by cutting along the (100) crystallographic plane [46]. This new class of perovskites can be easily divided in two categories: Ruddlesden-Popper (RP) [47] and Dion-Jacobson (DJ) [48] perovskites.

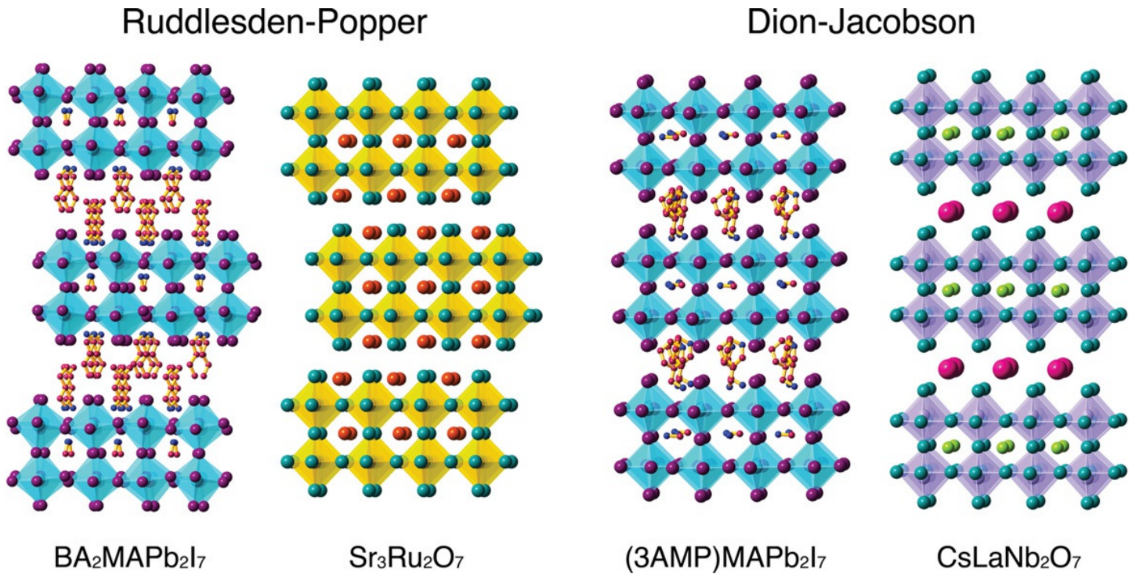

Figure 2.2: The two classes of layered perovskites (2D) for both organic and inorganic structures, showing the Ruddlesden-Popper (RP) (two configurations on the left side) and the Dion-Jacobson (DJ) (two configurations on the right side). Reproduced with permission from Ref.[46].

Due to the versatility of the Ruddlesden-Popper structures, which features long interlayer spacers between the two offset layers of the perovskite, this class received more research attention. Although less commonly studied, the Dion-Jacobson structures include only one long molecule per unit cell fitted between the two layers of the perovskite.

Another important aspect when conducting intensive *ab initio* simulations is their compatibility with the machine learning (ML) techniques [49] such as artificial neural networks, random forest and linear regression methods. For these reasons, some studies [34, 50] combined the framework of high-throughput DFT calculations and ML techniques, in order to investigate the structurally stable compositions of mixed-cation and mixed-halide perovskite materials which can be evaluated for the highest optical absorption and optimal stability.

2.2 Capacitive and Inductive Effects

From early studies, the dynamic hysteretic effect has been observed in illuminated perovskite solar cells [51, 52, 53]. This phenomenon is characterized by a discrepancy in the current density-voltage (J-V) characteristic between the forward voltage scan and the reverse voltage scan. During the forward scan, the voltage varies from short circuit to open circuit, while in the reverse scan, the voltage changes from open circuit to short circuit. W. Tress *et al.* [54] observed that the hysteresis effect becomes more pronounced at faster (intermediate) scan rates, they attribute this behavior to extraction barriers which are introduced by ion migration.

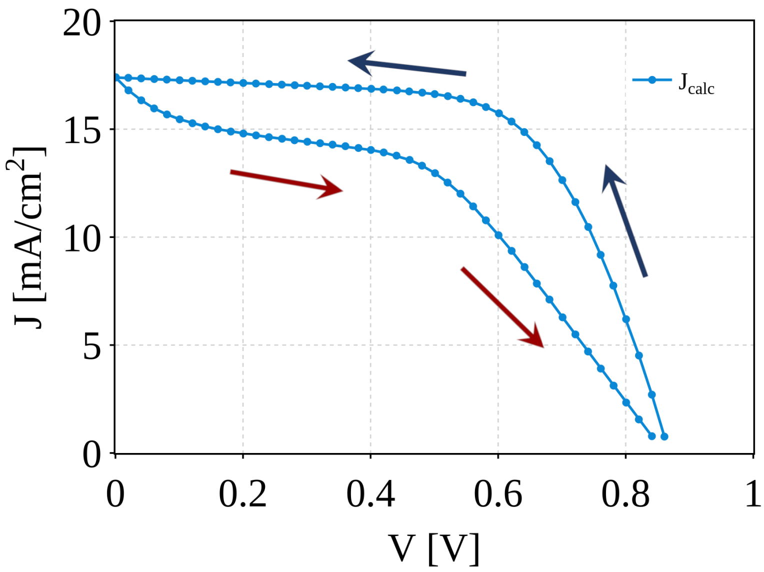

Figure 2.3: Simulation of the current density-voltage (J-V) for a PSC, showing the reverse-forward scan and the hysteresis effect.

It is essential to understand the dynamic phenomena that PSCs exhibit during exposure to solar spectrum in order to properly evaluate the solar cell PCE and to compensate for undesirable effects such as cell degradation. Regarded as a capacitive effect, many interpretations have been proposed for the apparition of dynamic hysteretic behaviour in PSCs. Some of these include ferroelectric polarization [55, 56], ion migration [54], trapping and detrapping of carriers [57], a giant dielectric constant [58] or large accumulations of charges at the interfaces [59].

Following the discovery of hysteretic effects, numerous models have been developed. These models primarily use drift-diffusion equations and equivalent circuits to describe the dynamic J-V characteristics and provide small signal analysis as well. One of the first drift-diffusion-based models which was used to reproduce dynamic J-V hysteresis was developed by Van Reenen *et al.* (2015) [60]. The model incorporated ionic migration and trapping through the use of a finite difference method. Similarly, G. Richardson *et al.* (2016) implemented a time-dependent drift-diffusion model [61] that includes ionic charge buildup, employing the method of matched asymptotic analysis in order to overcome the numerical challenges.

Based on an equivalent circuit, G. A. Nemnes *et al.* (2017) introduced a dynamic electrical model (DEM), assuming slow relaxation of the internal device polarization[62]. Likewise, S. Ravishankar *et al.* (2017) described a surface polarization model (SPM) [63] with large accumulation capacitances, which was later extended by E. Ghahremanirad *et al.* (2017) in order to include inductive effects [64]. The DEM was reformulated by D. V. Anghel *et al.* (2019) in terms of a non-linear capacitor [65], while N. E. Courtier *et al.* (2019) derived a simplified surface polarization model that replaced ion dynamics with non-linear capacitances [66], starting from the drift-diffusion model proposed by Richardson *et al.* (2016) [61].

A. J. Riquelme *et al.* (2022) analyzed the connection between drift-diffusion simulations and equivalent circuits, revealing how specific electronic and ionic contributions affect different circuit components [67],therefore enabling their correlation with ion-driven mechanisms. A drift-diffusion model coupling ionic migration to quasi steady-state electron and hole currents was developed by D. Jacobs *et al.* (2018), resulting in phase-delayed recombination of photogenerated carriers [68]. Based on ionically gated transistor behaviour, D. Moia *et al.* (2019) proposed an extensive equivalent circuit model [69].

By using electrochemical impedance spectroscopy (EIS), a peculiar large inductive behaviour has been observed in some PSCs. The inductive or negative capacitance behaviour has been attributed to several factors: a kinetic effect induced by ions causing a delay in surface voltage and charge accumulations[70, 71], phase-delayed recombination [68], electron injection effects [69, 72], ionic-mediated recombination [73] or the action of a chemical inductor [74] and a term used for a generic behaviour arising from two coupled processes describing fast-slow dynamics.

Based on the chemical inductor phenomenology, the capacitive and inductive effects have been described in halide PSCs and memristors under illumination [75]. Inductive effects of chemical origin have been observed in current transients under illumination [76] and were further modeled using a neuron-style model [77]. Using equivalent circuits [78], a comprehensive review on impedance spectroscopy of perovskite solar cells summarizes the models proposed for explaining the capacitive and inductive effects.

The significant capacitive and inductive effects that were reported have sparked debates regarding the underlying mechanisms, resulting in the development of two primary model categories. One category is based on substantial accumulation capacitances, while the other focuses on ionic modulation of the collected current. In this work, we present a new equivalent circuit model that interprets these phenomena through recombination current modulation, distinguishing between the contributions from ion current and ionic charge accumulations [79]. These contributions are linked to capacitive and inductive effects, respectively. We support our findings with numerical simulations and electrochemical impedance spectroscopy (EIS) measurements.

Computational Methods

For the properties analysis and calculations performed in this study, we have employed three different computational methods relevant for material characterization, dynamic effects exploration and device simulation. The first method relies on DFT calculations, which are implemented using the (Spanish Initiative for Electronic Simulations with Thousands of Atoms) SIESTA simulation code. The second method addresses the appearance of dynamic hysteretic effects in PSCs during illumination, reproduced by implementing a dynamic electrical model based on an equivalent circuit of a PSC. The third computational method involves PSC device modeling using a Solar Cell Capacitance Simulator (SCAPS).

3.1 Density Functional Theory (DFT)

Density Functional Theory (DFT) stands as a cornerstone in the field of computational chemistry and condensed matter physics, offering a robust and versatile framework for investigating the electronic structure of atoms, molecules and solids, including charge and spin transport, as exemplified in Refs. [80, 81, 49, 82]. Developed from the principles of quantum mechanics, DFT provides a practical and often remarkably accurate means to calculate the properties of many-body systems, avoiding the prohibitive computational cost associated with wavefunction-based methods.

The origins of DFT trace back to the important works of Hohenberg and Kohn in 1964 [83], followed by Khon and Sham in 1965 [84]. The Hohenberg-Kohn theorems laid the theoretical foundation by proving that the ground-state properties of a many-electron system are uniquely determined by its electron density, rather than the many-electron wavefunction. This marked a significant paradigm shift, as the electron density, a function of only three spatial coordinates, is vastly simpler to handle compared to the many-dimensional wavefunction.

Building upon this, Kohn and Sham introduced a practical approach to DFT, reformulating the complex many-body problem into a set of self-consistent single-electron equations. This Kohn-Sham scheme leverages an exchange-correlation functional to account for the many-body interactions, enabling accurate predictions of electronic properties with manageable computational resources.

Over the decades, DFT has evolved significantly, incorporating advanced functionals and techniques to enhance its accuracy and applicability. Its success is evident across a broad spectrum of applications, from understanding fundamental chemical reactions and material properties to designing new drugs and materials with tailored properties.

3.1.1 Fundamental Concepts

In order to understand the behaviour and properties of a system of nuclei and electrons, the theoretical approach [85] is to solve the Schrödinger equation [86]. For this reason, we introduce the Hamiltonian $\hat{H}$ for a system with N_e electrons and N_n nuclei which can be written as:

$$\hat{H} = \hat{T}_e + \hat{T}_n + \hat{V}_{ee} + \hat{V}_{nn} + \hat{V}_{en} \tag{3.1}$$

where:

- $\hat{T}_e$ is the kinetic energy of the electrons;
- $\hat{T}_n$ is the kinetic energy of the nuclei;
- $\hat{V}_{ee}$ is the potential energy due to electron-electron interactions;
- $\hat{V}_{nn}$ is the potential energy due to nucleus-nucleus interactions;
- $\hat{V}_{en}$ is the potential energy due to electron-nucleus interactions.

The kinetic energy of the electrons in the system is represented by ($\hat{T}_e$):

$$\hat{T}_e = -\sum_{i=1}^{N_e} \frac{\hbar^2}{2m_e} \nabla_i^2$$

where $\hbar$ is the reduced Planck's constant, m_e is the electron mass and ∇_i^2 is the Laplacian operator acting on the i-th electron.

The kinetic energy of nuclei ($\hat{T}_n$) is:

$$\hat{T}_n = -\sum_{I=1}^{N_n} \frac{\hbar^2}{2M_I} \nabla_I^2$$

where M_I is the mass of the I-th nucleus and ∇_I^2 is the Laplacian operator acting on the I-th nucleus.

The potential energy due to electron-electron interaction ($\hat{V}_{ee}$) is equal to:

$$\hat{V}_{ee} = \sum_{i<j}^{N_e} \frac{e^2}{4\pi\epsilon_0 |\mathbf{r}_i - \mathbf{r}_j|}$$

where e is the elementary charge, ϵ_0 is the vacuum permittivity and $\mathbf{r}_i$ and $\mathbf{r}_j$ are the positions of the i-th and j-th electrons, respectively.

The potential energy due to nucleus-nucleus interaction ($\hat{V}_{nn}$) is:

$$\hat{V}_{nn} = \sum_{I<J}^{N_n} \frac{Z_I Z_J e^2}{4\pi\epsilon_0 |\mathbf{R}_I - \mathbf{R}_J|}$$

where Z_I and Z_J are the atomic numbers of the I-th and J-th nuclei and $\mathbf{R}_I$ and $\mathbf{R}_J$ are their positions.

The potential energy due to electron-nucleus interaction ($\hat{V}_{en}$) is represented by:

$$\hat{V}_{en} = -\sum_{i=1}^{N_e} \sum_{I=1}^{N_n} \frac{Z_I e^2}{4\pi\epsilon_0 |\mathbf{r}_i - \mathbf{R}_I|}$$

By reproducing equation 3.1, the full Hamiltonian for the system of electrons and nuclei can be written as:

$$\begin{aligned}\hat{H} = -\sum_{i=1}^{N_e} \frac{\hbar^2}{2m_e} \nabla_i^2 - \sum_{I=1}^{N_n} \frac{\hbar^2}{2M_I} \nabla_I^2 + \sum_{i<j}^{N_e} \frac{e^2}{4\pi\epsilon_0 |\mathbf{r}_i - \mathbf{r}_j|} \\ + \sum_{I<J}^{N_n} \frac{Z_I Z_J e^2}{4\pi\epsilon_0 |\mathbf{R}_I - \mathbf{R}_J|} - \sum_{i=1}^{N_e} \sum_{I=1}^{N_n} \frac{Z_I e^2}{4\pi\epsilon_0 |\mathbf{r}_i - \mathbf{R}_I|}\end{aligned} \tag{3.2}$$

The Born-Oppenheimer approximation simplifies the treatment of molecular systems by decoupling the nuclear and electronic motion due to their large mass difference. This approximation assumes that the nuclei move much more slowly compared to the electrons, allowing the electronic wavefunctions to be calculated for fixed nuclear positions. This way, the electronic Hamiltonian $\hat{H}_e$ for fixed nuclear positions $\{\mathbf{R}_I\}$ can be written as:

$$\hat{H}_e(\{\mathbf{r}_i\}; \{\mathbf{R}_I\}) = \hat{T}_e + \hat{V}_{ee} + \hat{V}_{en} \tag{3.3}$$

By using the electronic Hamiltonian the time independent Schrödinger equation can be solved for fixed nuclear positions:

$$\hat{H}_e(\{\mathbf{r}_i\}; \{\mathbf{R}_I\}) \psi_e(\{\mathbf{r}_i\}; \{\mathbf{R}_I\}) = E_e(\{\mathbf{R}_I\}) \psi_e(\{\mathbf{r}_i\}; \{\mathbf{R}_I\})$$

Although the Born-Oppenheimer approximation is very helpful in reducing the problem complexity, one must keep in mind that for a system with many electrons, each electron contributes three degrees of freedom (x, y, z). For N electrons, this results in a 3N-dimensional problem. The wavefunction ψ_e thus depends on 3N variables, making the solution of the Schrödinger equation computationally demanding.

3.1.2 Thomas-Fermi Approximation Model

In the late 1920s, Thomas [87] and Fermi [88] introduced in their works an approximation of a statistical model that simplifies the treatment of many-electron systems by considering the electron density $\rho(\mathbf{r})$ as a continuous variable. The model is based on the electron density $\rho(\mathbf{r})$ which represents the number of electrons per unit volume at position $\mathbf{r}$. The attractivity of the approximation model comes from the simplicity introduced by equation 3.4 when compared with the full many body solutions of the Schrödinger equation.

$$\rho(\mathbf{r}) = \frac{1}{3\pi^2} (2m_e)^{3/2} \left(\frac{1}{\hbar^2} (E_F - V(\mathbf{r})) \right)^{3/2} \tag{3.4}$$

where:

- m_e is the electron mass;
- $\hbar$ is the reduced Planck's constant;
- E_F is the Fermi energy;
- $V(\mathbf{r})$ is the potential energy at point $\mathbf{r}$.

Even though, their model provided a less accurate calculation of the kinetic energy of the system, the work represented the first step towards the DFT theory apparition. Later on, a few corrections were made, one in 1930 by Dirac [89] who introduced an exchange potential in order for the model to respect the Pauli exclusion principle. The second correction to the model was made by Weizsäcker in 1935 [90] in order to increase the accuracy in calculating the system kinetic energy.

Thomas and Fermi provided a method to describe the electron density in terms of the potential energy of the electrons due to the nuclei and the electrostatic repulsion between electrons. More interesting is that solving the approximation model requires successive iterations, which is quite similar to the modern DFT implementation: (I) Start with an initial guess for the potential $V(\mathbf{r})$, (II) Use the initial potential to calculate the electron density $\rho(\mathbf{r})$, (III) Solve Poisson's equation to update the potential $V(\mathbf{r})$ and (IV) Repeat steps II and III until self-consistency is achieved.

3.1.3 Hohenberg-Kohn Theorems

The first DFT breakthrough was made by Pierre Hohenberg and Walter Kohn in 1964 in their work entitled ”Inhomogeneous Electron Gas” [83], where the authors deal ”with the ground state of an interacting electron gas in an external potential $V(\mathbf{r})$”. They introduce two theorems which are fundamental results in density functional theory (DFT) that establish the relationship between the ground state properties of a many-electron system and its electron density.

Reformulated in Ref. [91], the first theorem states that ”for any system of interacting particles in an external potential $V(\mathbf{r})$, the potential $V(\mathbf{r})$ is determined uniquely, except for a constant, by the ground-state particle density $\rho(\mathbf{r})$.” This implies that all other ground state properties of the system are uniquely determined by $\rho(\mathbf{r})$.

$$\rho(\mathbf{r}) \longleftrightarrow V(\mathbf{r})$$

According to Richard M. Martin (2020), the second Hohenberg-Kohn theorem proves that ”a universal functional for the energy $E[\rho]$ in terms of the density $\rho(\mathbf{r})$ can be defined, valid for any external potential $V(\mathbf{r})$. For any particular $V(\mathbf{r})$, the exact ground-state energy of the system E_0 is the global minimum value of this functional ($E[\rho]$) and the density $\rho(\mathbf{r})$ that minimizes the functional is the exact ground-state density $\rho_0(\mathbf{r})$” (R.M. Martin, 2020 [91]). In this way, the total energy functional for a system of interacting electrons is given by:

$$E[\rho] = T[\rho] + V_{\mathrm{ee}}[\rho] + \int V(\mathbf{r})\rho(\mathbf{r})\, d\mathbf{r}$$

Here:

- $T[\rho]$ is the kinetic energy functional;
- $V_{\mathrm{ee}}[\rho]$ is the electron-electron interaction energy functional;
- $\int V(\mathbf{r})\rho(\mathbf{r})\, d\mathbf{r}$ is the potential energy due to the external potential $V(\mathbf{r})$.

3.1.4 Kohn-Sham Theorems

Although, Hohenberg and Kohn’s variational model is very appealing, they have not provided a practical example of a multi particle system that can be solved. For this reason, one year later W. Kohn and L.J. Sham [84] extend the Hohenberg-Kohn theorems by introducing a practical framework for calculating the ground state properties of many-electron systems. The key idea was to map the interacting electron system to a system of non-interacting electrons that yields the same ground state density.

The Kohn-Sham ansatz assumes that the complex many-body problem of interacting electrons can be mapped onto a system of non-interacting electrons that have the same ground state electron density $\rho(\mathbf{r})$. This way, the total energy functional in the Kohn-Sham approach for a system of N electrons becomes:

$$E[\rho] = T_s[\rho] + V_{\text{en}}[\rho] + V_{\text{H}}[\rho] + E_{\text{xc}}[\rho]$$

where:

- $T_s[\rho]$ is the kinetic energy of the non-interacting electrons,

$$T_s[\rho] = -\frac{1}{2}\sum_{i=1}^{N}\int \psi_i^*(\mathbf{r})\nabla^2\psi_i(\mathbf{r})\,d\mathbf{r}$$

- $V_{\text{en}}[\rho]$ is the electron-nucleus attraction,

$$V_{\text{en}}[\rho] = -\int V(\mathbf{r})\rho(\mathbf{r})\,d\mathbf{r}$$

- $V_{\text{H}}[\rho]$ is the Hartree (electron-electron repulsion) term,

$$V_{\text{H}}[\rho] = \frac{1}{2}\int\int \frac{\rho(\mathbf{r})\rho(\mathbf{r}')}{|\mathbf{r}-\mathbf{r}'|}\,d\mathbf{r}\,d\mathbf{r}'$$

- $E_{\text{xc}}[\rho]$ is the exchange-correlation energy functional.

Kohn-Sham Equations

The Kohn-Sham equations are a set of self-consistent single-particle equations that yield the same ground state density as the interacting system:

$$\left[-\frac{1}{2}\nabla^2 + V_{\text{eff}}(\mathbf{r})\right]\psi_i(\mathbf{r}) = \epsilon_i\psi_i(\mathbf{r})$$

where the effective potential $V_{\text{eff}}(\mathbf{r})$ is given by:

$$V_{\text{eff}}(\mathbf{r}) = V(\mathbf{r}) + \int \frac{\rho(\mathbf{r}')}{|\mathbf{r}-\mathbf{r}'|}\,d\mathbf{r}' + \frac{\delta E_{\text{xc}}[\rho]}{\delta\rho(\mathbf{r})}$$

The self-consistent loop for solving the Kohn-Sham equation represents the core method for DFT calculations. The computational approach required for solving the Kohn-Sham equation follows the next five steps:

1. **Initialize the electron density**: Start with an initial guess for the electron density $\rho(\mathbf{r})$;

2. **Calculate the Effective Potential**: Use the initial $\rho(\mathbf{r})$ to calculate the effective potential $V_{\text{eff}}(\mathbf{r})$;

3. **Solve Kohn-Sham Equation**: Solve Kohn-Sham equation to obtain $\psi_i(\mathbf{r})$;

4. **Calculate the electron density**: Using $\psi_i(\mathbf{r})$ calculate the associated $\rho(\mathbf{r})$;

5. **Reiterate**: Repeat steps 2, 3 and 4 until self-consistency is achieved (the initial and calculated density match).

At this moment in history, the DFT theory was completed and provides a proper approach in order to solve the many body problem. Now, a crucial role in the DFT calculations accuracy is represented by the exchange-correlation functional which can directly influence the predicted properties of materials, such as their electronic structure, total energy and response to external perturbations. In DFT, the exchange-correlation functional is part of the total energy functional that describes the complex interactions in the many body electron system. Since the exact form of $E_{\text{xc}}[\rho]$ is unknown, several approximations have been developed over time:

Local density approximation(LDA) assumes that the exchange-correlation energy at a point in space depends only on the electron density at that point and is given by:

$$E_{\text{xc}}^{\text{LDA}}[\rho] = \int \rho(\mathbf{r})\epsilon_{\text{xc}}(\rho(\mathbf{r}))\, d\mathbf{r}$$

where $\epsilon_{\text{xc}}(\rho)$ is the exchange-correlation energy density of a uniform electron gas with density ρ.

Generalized Gradient Approximation (GGA) improves upon LDA by considering not only the electron density but also its gradient and it has this form:

$$E_{\text{xc}}^{\text{GGA}}[\rho] = \int f(\rho(\mathbf{r}), \nabla\rho(\mathbf{r}))\, d\mathbf{r}$$

where f is a function that depends on both the density and its gradient.

With the recent development of the DFT methods, there are other functionals to mention like the Meta-GGA [92] functionals which include a higher-order derivative of the density or the hybrid functionals [93, 94] which incorporate a portion of the exact exchange energy from Hartree-Fock theory, combined with the exchange-correlation energy from an approximate functional.

3.2 SIESTA Implementation

SIESTA (Spanish Initiative for Electronic Simulations with Thousands of Atoms) method was developed in order to perform electronic structure calculations and *ab initio* molecular dynamics simulations of molecules and solids. The apparition of the SIESTA computational method can be dated to 1996 when P. Ordejon *et al.* [95] introduced "a method to perform fully self-consistent density-functional calculations that scales linearly with the system size"(P. Ordejon, 1996), based on some previous works [96, 97] the authors used the order-N algorithms [98] scalability to develop a fully self-consistent DFT approach.

The SIESTA algorithm implementation was fully described in 2002 in the work of Jose M Soler *et al.* in the article "The SIESTA method for *ab initio* order-N materials simulation" published in the Journal of Physics. The authors "have developed and implemented a selfconsistent density functional method using standard norm-conserving pseudopotentials and a flexible, numerical linear combination of atomic orbitals basis set, which includes multiple-zeta and polarization orbitals" (J.M. Soler, 2002). This way, they built the first selfconsistent DFT method that was linearly scaling the computational cost with the system size, compared with the other methods where the computational cost scales with N^3 or worse with the number of atoms.

In the framework of the standard Kohn-Sham version of DFT, the SIESTA code can use multiple exchange-correlation functionals, such as: the local (spin) density approximation (LDA/LSDA) or the generalized-gradient-corrections (GGA) and a new implementation allowing a functional for describing the Van der Waals interactions. Another important aspect is that SIESTA uses nonlocal norm-conserving pseudopotentials which offer a uniform grid implementation of a smooth (pseudo-) charge density[95]. The combined implementation of pseudopotentials with atomic basis sets eliminates the treatment requirement for core electrons.

By adding flexible linear combination of atomic orbitals basis sets[98] with the order-N scaling, it provided fast (scaling linearly with N) and accurate calculations even when using minimal basis sets. On the other hand, due to the sparsity of the Hamiltonian in order-N methods, the utilization of a strictly confined orbital was introduced (after a certain radius, the orbital is considered equal to zero). In this way, the orbital confinement further enhancies the SIESTA computational efficiency.

In the standard output, the SIESTA code provides the following information: total and partial forces; atomic, orbital and bond population; stress tensor; atomic forces; electric dipole moment; and the electron density. According to the SIESTA manual user guide [99], by specifying some system parameters and input requirements the code can also calculate the following properties:

"

- Geometry relaxation, fixed or variable cell;
- Constant temperature molecular dynamics (Nose thermostat);
- Variable cell dynamics (Parrinello-Rahman);
- Spin polarized calculations (collinear or not);
- k-sampling of the Brillouin zone;
- Local and orbital-projected density of states;
- COOP and COHP curves for chemical bonding analysis;
- Dielectric polarization;
- Vibrations (phonons);
- Band structure;
- Ballistic electron transport under non-equilibrium (through TranSIESTA).

"(Emilio Artacho, 2021).

In SIESTA the DFT+U formalism is also implemented using the LDA+U method which corrects the interaction between strongly correlated orbitals and treat the other valence electrons at the level of standard DFT. The DFT+U formalism emerged due to the "strongly correlated" electronic states in a system, where the localized d or f orbitals play a significant role. This formalism introduces a Hubbard-like model [100] where it uses a correction term U to account for the on-site Coulomb interaction that is inadequately described by standard DFT.

There are many recent developments of the SIESTA code. Among them, we find the following: new pseudopotential format (psml)[101], DFT+U correction for correlated systems [102], van der Waals functionals [103, 104], hybrid functionals [105], spin-orbit coupling[106, 107], time dependent DFT [108], TransSiesta method [109], Wannierization [110], utilities for post-processing and supplementary features [111], etc. All this new implementations show the versatility and reliability of the SIESTA method in calculating materials properties.

3.3 Equivalent Circuit Modeling of PSCs

In order to properly understand the dynamic hysteretic effects that are taking place during the PSCs operation, emerged the need for an equivalent circuit model which can simulate the PSC behaviour under illumination. Mainly, due to the ionic migration, the hysteresis effects induce an uncertainty in the evaluation of the power conversion efficiency (PCE) and can be one of the principal sources for the perovskite degradation mechanisms.

For a proper approach to perform ion migration analysis, we have developed a new multiscale dynamic electrical model (m-DEM) [79] by identifying the physical processes responsible for the degradation and correlating these with the structural elements of the device. In this way, the model is able to describe both large signal and small signal measurements, focusing on the main features that are observed in typical experiments.

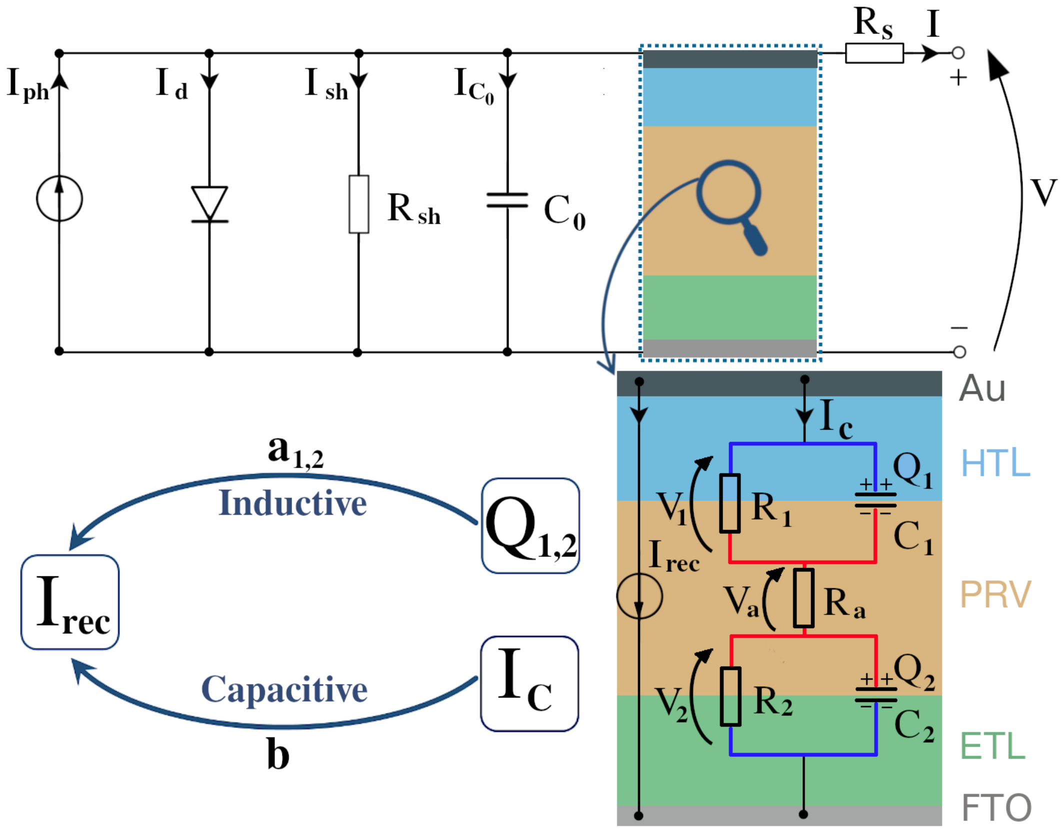

Figure 3.1: Equivalent PSC circuit model used for describing the capacitive and inductive effects. The colorful sections represent the PSC elements in standard configuration with FTO and gold electrodes. Reprinted with permission from Ref. [79]

Starting from the ionic conductor nature of the perovskite layer, we introduce an equivalent circuit model in order to underline the ionic charge current and ionic charge accumulation roles in modulating the recombination current. When a PSC is operating in normal conditions, the ions (halide ions or halide vacancies) are migrating due to the electric field established in the perovskite layer. The apparent huge capacitance was proven to be connected to the ionic current while the inductive effects are attributed to the ionic accumulations.

In the general equivalent circuit model from Fig. 3.1, we describe the solar cell operation starting from the standard equivalent circuit with a particular form for the recombination current, which is derived from the underlying elements. To this end, we consider a detailed partitioning of the device region into HTL, absorber and ETL, with the associated interfaces. The equivalent circuit model was constructed to reproduce the behaviour of a typical FTO/ETL/PRV/HTL/Au solar cell, which yields the time dependence of the current under illumination and bias conditions in a dynamic regime, showing the different roles of ionic charge current and ionic charge accumulation.

The m-DEM model, is composed of standard elements which can be classified in two groups. The first group contains the typical circuit elements of a PSC, like the current source which is equivalent with the photogenerated current $\mathrm{I_{ph}}$, the diode element introducing a current $\mathrm{I_d}$ of recombination, the shunt resistance $\mathrm{R_{sh}}$, with a recombination current $\mathrm{I_{sh}}$, the series resistance $\mathrm{R_s}$ and the output current I.

The second group contains the circuit elements which are introduced in the m-DEM model in order to replicate the PSC behaviour. Beyond the small geometrical capacitance $\mathrm{C_0}$, which is counting for the hysteretic effects, we have introduced two essential parts, namely the R-C circuit block and the additional current source corresponding to the ionic modulated recombination current ($\mathrm{I_{rec}}$). In the R-C circuit there are two parallel groups of resistances facing capacitors ($\mathrm{R_1}$-$\mathrm{C_1}$ and $\mathrm{R_2}$-$\mathrm{C_2}$), that are in series with a perovskite absorber ionic resistance $\mathrm{R_a}$.

The corresponding charges $\mathrm{Q_1}$ and $\mathrm{Q_2}$ for the capacitors $\mathrm{C_1}$ and $\mathrm{C_2}$, associated with the instantaneous applied voltages $\mathrm{V_1(t)}$ and $\mathrm{V_2(t)}$, are used to describe the ionic charge accumulation at the two interfaces (PRV-ETL and PRV-HTL). While, $\mathrm{R_1}$ and $\mathrm{R_2}$ resistances account for the electron- or hole-ion charge neutralization at the two interfaces and can be considered as loss resistances for the ionic capacitors. The I_c current represents the ionic current flowing inside the perovskite absorber layer.

A typical dynamic measurement consists of one reverse scan followed by a forward scan, with a scan rate α, which corresponds to the changing voltage V(t) (α=dV/dt).

3.3.1 Large Signal Model

The equivalent circuit model illustrated in Figure 3.1 effectively replicates the characteristic hysteretic effects observed in PSCs dynamic J-V measurements. The m-DEM model accurately simulates the current bump in the reverse characteristics following positive bias pre-poling, the dependence of hysteresis magnitude on the bias scan rate, as well as both normal hysteresis (NH) and inverted hysteresis (IH) behaviours. In the context of the m-DEM model, the dynamic J-V characteristics are described by the following system of equations:

$$\frac{\partial V_1}{\partial t} = -\frac{1}{C_1}\left(\frac{R_\mathrm{a}+R_1}{R_\mathrm{a}R_1}\right)V_1 + \frac{V+IR_\mathrm{s}-V_2}{R_\mathrm{a}C_1} \tag{3.5}$$

$$\frac{\partial V_2}{\partial t} = -\frac{1}{C_2}\left(\frac{R_\mathrm{a}+R_2}{R_\mathrm{a}R_2}\right)V_2 + \frac{V+IR_\mathrm{s}-V_1}{R_\mathrm{a}C_2} \tag{3.6}$$

$$I_\mathrm{ph} - I_\mathrm{d} - I_\mathrm{sh} - I_\mathrm{c0} - I_\mathrm{c} - I_\mathrm{rec} - I = 0 \tag{3.7}$$

The equations 3.5 - 3.7, provide the time-dependent behaviour of the state variables V_1, V_2 and I, with the applied voltage V(t) and initial conditions V_1(t=0), V_2(t=0) and I(t=0) as inputs. These initial conditions are typically set by applying a pre-poling voltage V_pol for a sufficient duration to achieve a steady state. Subsequently, a continuous reverse-forward scan is conducted, where the voltage V is varied from an initial voltage V_0 to short-circuit and back.

The last equation (3.7) contains different current contributions:

- I_d is the diode current and represents the effective junction recombination in the absence of ions, depending on the diode saturation current I_s and also on the solar cell ideality factor n_id. In this picture, the diode current can be expressed in the following form:

$$I_\mathrm{d} = I_\mathrm{s}\left[\exp\left(\frac{q_\mathrm{e}(V+IR_\mathrm{s})}{n_\mathrm{id}k_\mathrm{B}T}\right)-1\right]$$

- I_sh is the shunt recombination current, typically small for performant solar cells. It appears due to pinholes defects and metal diffusion which may induce junction short-circuits. It has the expression:

$$I_\mathrm{sh} = (V+IR_\mathrm{s})/R_\mathrm{sh}$$

- I_{C_0} is the current due to the geometrical capacitance,

$$I_{\mathrm{C}_0} = C_0\left(\frac{\partial V}{dt} + R_\mathrm{s}\frac{\partial I}{\partial t}\right)$$

- I_c is the current due to ionic capacitance,

$$I_\mathrm{c} = \frac{V + IR_\mathrm{s} - V_1 - V_2}{R_\mathrm{a}}$$

At the core of our circuit model is the assumption that the recombination current (I_rec) is controlled by the ion charge accumulation and ionic current. In this way, I_rec plays a major role in reproducing the hysteretic effects in the J-V characteristics, affecting also the inductive and capacitive effects.

$$I_\mathrm{rec} = I_\mathrm{rec0} + \sum_{i=1}^{2} a_i Q_i + bI_\mathrm{c} \tag{3.8}$$

In this picture, we describe the I_rec dependence to the ionic current and ionic charge accumulation, by adding to the reference recombination current I_rec0 the inductive current $I^\mathrm{L}_\mathrm{rec} = \sum_{i=1}^{2} a_i Q_i$ and the capacitive current $I^\mathrm{C}_\mathrm{rec} = bI_\mathrm{c}$, where the inductive or capacitive currents are controlled by a_i and b scalars.

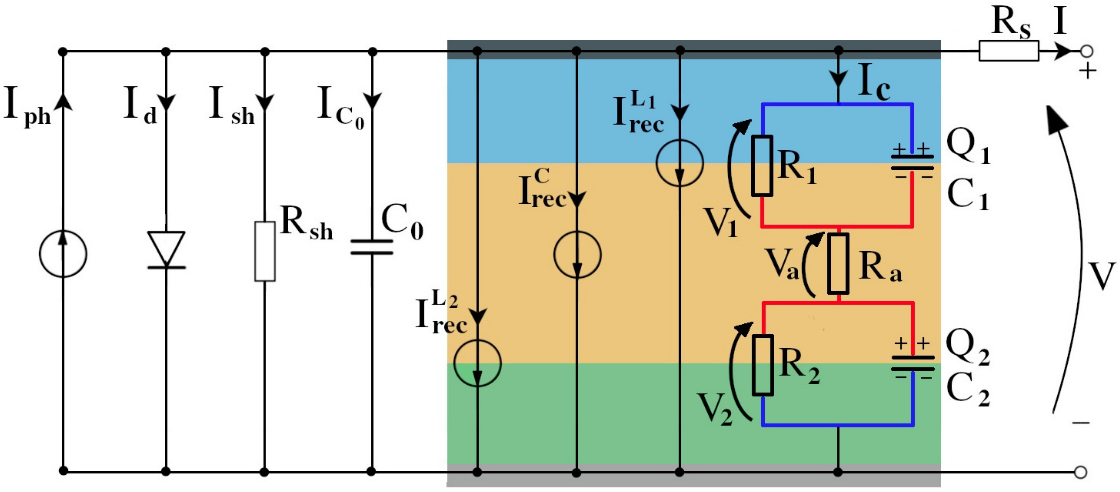

Figure 3.2: Detailed description of the ionic recombination current I_rec in the large signal circuit model, based on the ionic charge accumulations Q_i (i=1,2) and capacitive contributions related to the ionic current($J_\mathrm{c} = \sigma_\mathrm{ion}\mathcal{E}$, where σ_ion is ionic conductivity of the absorber). The blue and red colors on the circuit represents the ionic and electrons/holes pathways. Reprinted with permission from Ref. [79].

Another important aspect of our model are the ($C_0 \sim 0.1$ μF and $C_{1,2} \sim 10-100$ μF) small geometrical capacitances which are bellow the huge reported ones by using impedance spectroscopy measurements are $\sim 10-100$ mF. In this context, the ionic interface capacitances (C_1,C_2) are described as functions of voltage,

$$C_i(V_i) = \bar{C}_{0i} + \bar{C}_{1i} \exp\left(\frac{q_\mathrm{e} V_i}{n_c k_\mathrm{B} T}\right) \tag{3.9}$$

the ionic charges are also expressed as functions of voltage:

$$Q_i(V_i) = \bar{C}_{0i}V_i + \bar{C}_{1i}\frac{n_c k_{\mathrm{B}}T}{q_{\mathrm{e}}}\left[\exp\left(\frac{q_{\mathrm{e}}V_i}{n_c k_{\mathrm{B}}T}\right) - 1\right] \tag{3.10}$$

Where k_{B} and q_{e} are the Boltzmann constant and electron charge and V_i is used for the applied instantaneous voltages on the two capacitors. The $\bar{C}_{0i}$, $\bar{C}_{1i}$ and n_c are introduced to control the exponential behaviour [65].

With the help of equation 3.8, we have incorporated the two recombination currents corresponding to the ionic charge accumulation and ionic currents. Due to the ions migration and accumulation at the interfaces (PRV-ETL, PRV-HTL), there will be generated a high local density of defects, for which we expect a proportionally large electron-hole recombination current. This is controlled through a_i parameter in the second term in of Eq. 3.8 and is associated with the inductive effects.

The third term of the equation counts for the recombination current due to the electric field in the perovskite absorber layer. The parameter b was introduced in order to rescale the I_c ionic current. This way, the apparent huge capacitive effects are reconstructed when the capacitive current is driven in phase with the recombination current component.

3.3.2 Small Signal Model

The small-signal circuit can be obtained from the large signal model presented in Figure 3.2, by replacing the diode element with dynamic resistance R_{d} (where $R_{\mathrm{d}} = nk_{\mathrm{B}}T/(q_{\mathrm{e}}I_{\mathrm{d}})$) and excluding the constant current source element (I_{ph}).

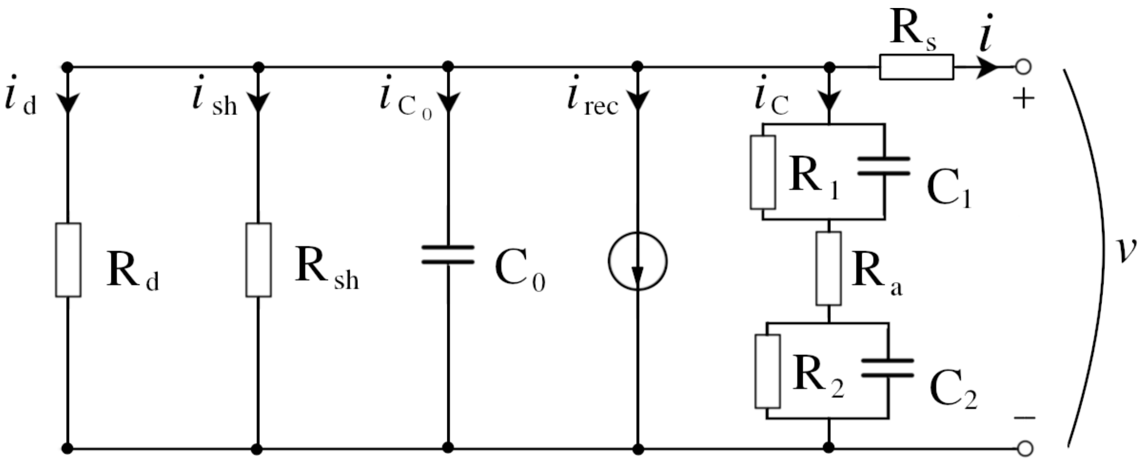

Figure 3.3: Small signal circuit model, in correspondence with Figure 3.2, where we have a two-interface circuit model with two ionic capacitances (C_1 and C_2), ionic capacitors' loss resistances (R_1 and R_2) and absorber ionic resistance (R_a). Incorporated with permission from Ref. [79].

The time dependent small current variation is obtained when a small-signal voltage $v(t)$ is applied for a given working point that is set through the external voltage $V = V_{\mathrm{wp}}$ with the help of (V_1, V_2, I). This way, the small current variation can be written:

$$-i = i_{\mathrm{d}} + i_{\mathrm{sh}} + i_{C_0} + i_C + i_{\mathrm{rec}} \tag{3.11}$$

In this context, the three standard parallel impedances can be grouped together into $Z_0 \equiv R_{\mathrm{d}} \parallel R_{\mathrm{sh}} \parallel Z_{C_0}$, in order to account for the diode element (R_{d}), shunt resistance (R_{sh}) and geometrical capacitor which is represented by $Z_{C_0} = 1/(j\omega C_0)$ (Z_{C_0} is the complex impedance associated with C_0 for the angular frequency ω):

$$Z_0 = \left[\frac{1}{R_{\mathrm{d}}} + \frac{1}{R_{\mathrm{sh}}} + \frac{1}{Z_{C_0}}\right]^{-1} \tag{3.12}$$

Therefore, the recombination current at the working point can be rewritten using Equation (3.8) into:

$$I_{\mathrm{rec}}(V) + i_{\mathrm{rec}} = I_{\mathrm{rec0}} + \sum_{i=1}^{2} a_i Q_i(V_i + v_i) + bI_{\mathrm{C}}(V + v) \tag{3.13}$$

which yields the small signal recombination current formula:

$$i_{\mathrm{rec}} = \left[\sum_{i=1}^{2} a_i C_i(V_i) Z_{R_i C_i} + b\right] \times i_C \tag{3.14}$$

Where Equation 3.14 components are:

- $Z_{R_i C_i}$ (i=1,2) are the equivalent impedances of the two R-C groups;

$$Z_{R_i C_i} = R_i/(j\omega R_i C_i + 1)$$

- v_i (i=1,2) are the small-signal voltages for the two R-C groups;

$$v_i = Z_{R_i C_i} i_C$$

- the inductive recombination component ($i_{\mathrm{rec}}^{\mathrm{L}}$) is given by:

$$i_{\mathrm{rec}}^{\mathrm{L}} = \sum_{i=1}^{2} a_i C_i(V_i) Z_{R_i C_i} \times i_C$$

- the capacitive recombination component ($i_{\mathrm{rec}}^{\mathrm{C}}$) is represented by:

$$i_{\mathrm{rec}}^{\mathrm{C}} = b \times i_C$$

On the other hand, we can express the equivalent impedance for the small signal model with the help of the total impedance coming from the ionic circuit block $Z_C = Z_{R_1C_1} + R_{\mathrm{a}} + Z_{R_2C_2}$ based on the small signal ionic current $i_C = (v + iR_{\mathrm{s}})/Z_C$. In this picture, the total impedance function is composed of the parallel group of impedances Z_0, $Z_{\mathrm{L}}^{\mathrm{eq}}$ and $Z_{\mathrm{C}}^{\mathrm{eq}}$, in series with R_{s}:

$$Z = \frac{v}{-i} = R_{\mathrm{s}} + \left[\frac{1}{Z_0} + \sum_{i=1}^{2} a_i C_i(V_i) \frac{Z_{R_iC_i}}{Z_C} + \frac{(b+1)}{Z_C}\right]^{-1} \tag{3.15}$$

where the inductive impedance component and the capacitive impedance components are given by:

$$\begin{aligned} Z_{\mathrm{L}}^{\mathrm{eq}} &= \left[\sum_{i=1}^{2} a_i C_i(V_i) \frac{Z_{R_iC_i}}{Z_C}\right]^{-1} && (3.16) \\ Z_{\mathrm{C}}^{\mathrm{eq}} &= \frac{Z_C}{(b+1)} && (3.17) \end{aligned}$$

Starting from the model shown in Figure 3.3, we can further simplify the two interface model by setting $R_1 \to \infty$, $R_2 \to 0$, which will reduce the two capacitor setup to a one capacitor model represented in Figure 3.4.

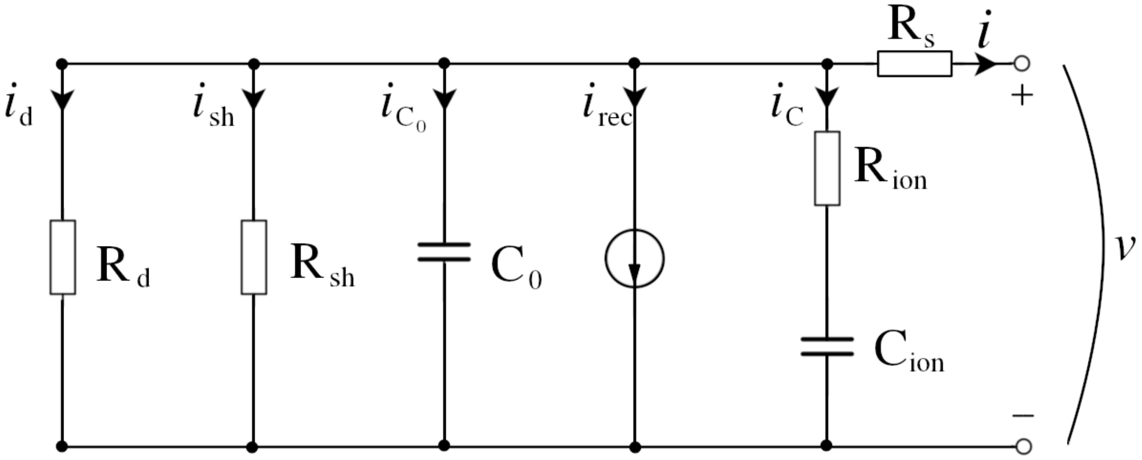

Figure 3.4: Small signal circuit model (in correspondence with Figure 3.3) where we have a simplified single interface model, which contains the ionic capacitance (C_{ion}) and the ionic resistance (R_{ion}) equal with the absorber ionic resistance (R_a). Included with permission from Ref. [79].

This way, by introducing the new notations $C_1 = C_{\mathrm{ion}}$, $R_a = R_{\mathrm{ion}}$, $a = a_1$, Eqs.

(3.14-3.17) can be rewritten as:

$$\begin{aligned} i_{\text{rec}} &= -j\frac{a}{\omega} \times i_C + b \times i_C && (3.18) \\ Z = \frac{v}{-i} &= R_{\text{s}} + \left[\frac{1}{Z_0} + \frac{1}{Z_{\text{RL}}} + \frac{1}{Z_{\text{RC}}}\right]^{-1} && (3.19) \\ Z_{\text{RL}} &= \frac{1}{aC_{\text{ion}}} + j\,\omega\frac{R_{\text{ion}}}{a} && (3.20) \\ Z_{\text{RC}} &= \frac{R_{\text{ion}}}{(b+1)} - j\frac{1}{\omega C_{\text{ion}}(b+1)} && (3.21) \end{aligned}$$

Where the inductive $i_{\text{rec}}^{\text{L}}$ and capacitive $i_{\text{rec}}^{\text{C}}$ parts in Equation (3.18) are represented by $i_{\text{rec}}^{\text{L}} = -j\frac{a}{\omega} \times i_C$ and $i_{\text{rec}}^{\text{C}} = b \times i_C$. On the other hand, one can identify the inductance $L = R_{\text{ion}}/a$, the capacitance $C_{\text{acc}} = (b+1)C_{\text{ion}}$ and the resistive components $R_{\text{L}} = 1/(aC_{\text{ion}})$, $R_{\text{acc}} = R_{\text{ion}}/(b+1)$ by using Eqs. (3.20) and (3.21).

Another important aspect of this approach is the possibility to define the apparent capacitance, which is typically measured by EIS, as it follows:

$$C_{\text{app}}(\omega) = \omega^{-1}\text{Im}(Z^{-1}) \qquad (3.22)$$

,which will further provide important aspects regarding the inductive and capacitive results.

3.3.3 Charge Collection and Charge Accumulation Models

The discovery of dynamic hysteretic effects in PSCs sparked a debate among researchers regarding whether this phenomenon should be classified under the *charge accumulation* (CA) or *charge collection* (CC) models. Initial studies based on impedance spectroscopy measurements attributed the observed large capacitances [112, 113, 59, 114] to the accumulation of charges and ions at the perovskite interfaces. These observations led to the development of CA models, which accurately describe the hysteretic effects [115, 62, 63, 64, 116]. In contrast, an alternative approach considered the influence of the electric field within the bulk of the perovskite on recombination and charge collection [117]. This led to the emergence of CC models, where the ionic-modulated recombination current depends on the internal electric field of the perovskite or results from modifications to the extraction barriers [68, 69].

In the context of these apparently opposite models, we compare our new CC model with a typical CA model (see Figure 3.5), this way, showing that both models can reproduce the dynamic hysteresis effects. Therefore, the one capacitor model described in Section 3.3.2 will be used to reproduce the core physics of the PSC device, while the implemented CA model resembles the circuit model used by Augustin Bou *et al.* [118]. Through this approach, we aim to set a bridging point between the CC and CA models. One can say that the microscopic picture of CC models is an alternative to the CA models, because they do not require a large charge accumulation, but rather a small ionic charge which can influence the charge collection properties.

(a) Charge accumulation (CA) model

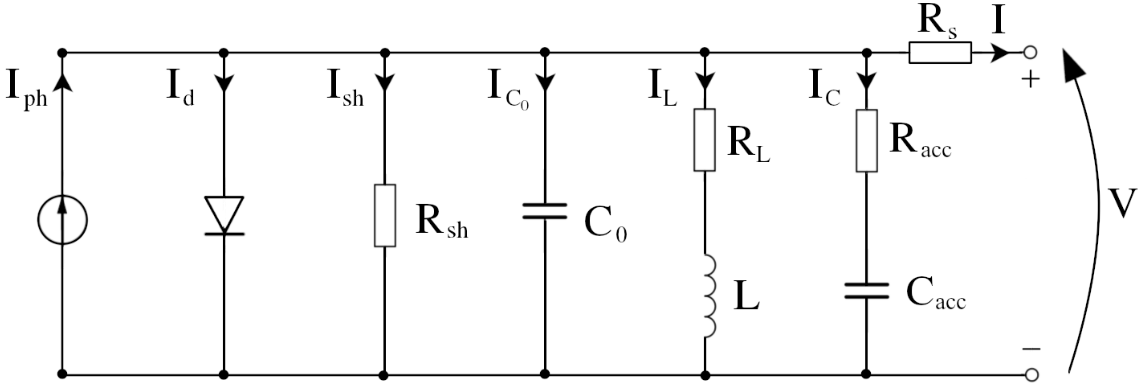

(b) Charge collection (CC) model

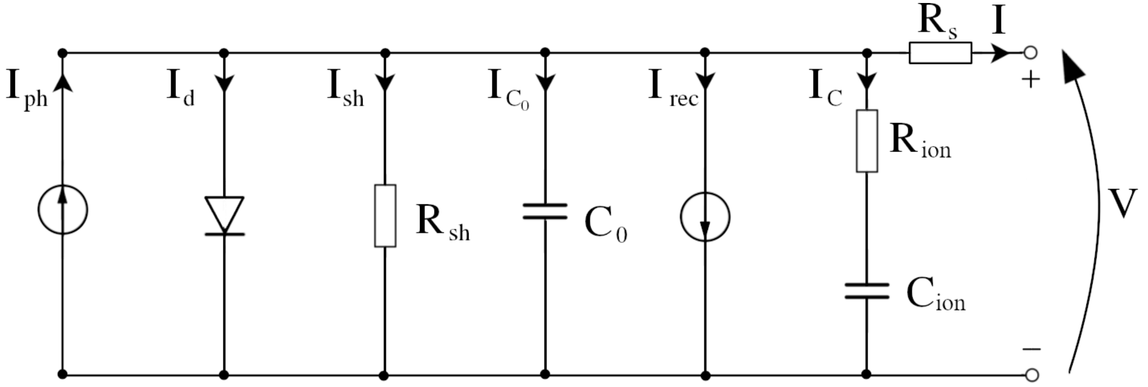

Figure 3.5: Comparison of the CA and CC models: (a) Charge accumulation model containing the inductive component (L). (b) Charge collection model which is based on ion modulated recombination, it does not contain an explicit inductive element. Used with permission from Ref.[79].

A key characteristic of hysteretic effects is the relatively large time constant τ, which typically ranges from a few seconds to several hundred seconds. In the context of an R-C circuit, this large time constant, $\tau = RC$, can result from either a large capacitance or a large resistance. The physical interpretation and magnitudes of these elements differ significantly between the two models. In the CA model, the accumulation capacitance, accounting for ions and photogenerated carriers, is considered large, $C_{\text{acc}} \sim 0.1$ F, with a relatively small resistance typical of electron/hole conduction, $R_{\text{acc}} \sim 100\ \Omega$. Conversely, in the CC model, these quantities are interpreted as a much smaller ionic capacitance, $C_{\text{ion}} \sim 100\ \mu$F and a much larger ionic resistance, $R_{\text{ion}} \sim 10^5\ \Omega$. Despite these differences, both models can be adjusted to produce the same time constant, $\tau = R_{\text{acc}}C_{\text{acc}} = R_{\text{ion}}C_{\text{ion}}$, making them formally equivalent.

We considered that the main contribution to the ionic current is coming from the migration of vacancies. This assumption is based on the estimation of the total vacancy concentration which is between $10^{17} - 10^{20}$ vacancies/cm^{-3} [119]. But in a real device, these numbers are affected by the vacancies traps which are between $10^{16} - 10^{18}$ vacancies/cm^{-3} [120] and are located in the close vicinity of the charge collecting interfaces. Therefore, the ionic charges are in minority and they have a minimal contribution to the ionic current.

When considering that a single ionic species is migrating and accumulating at one of the transporter layer interface, Eq. (3.8) can be rewritten as:

$$I_{\text{rec}} = I_{\text{rec0}} + aQ_{\text{c}} + bI_{\text{c}} = I_{\text{rec0}} + aQ_{\text{c}} + b\frac{\partial Q_{\text{c}}}{\partial t} \tag{3.23}$$

In the first step, by neglecting the inductance branch in the CA model depicted in Fig. 3.5(a), which corresponds to setting $a = 0$ in the CC model as given in Eq. (3.23), the two models become formally equivalent. During a typical reverse-forward scan, the relatively large current I_{c}^{CA} observed in the CA model, associated with the discharging and recharging of the capacitor C_{acc}, is exactly compensated in the CC model by the term $b \times I_{\text{c}}^{\text{CC}}$ in the recombination current I_{rec}. The net photogenerated currents are thus identical, i.e., $I_{\text{ph}}^{\text{CA}} = I_{\text{ph}}^{\text{CC}} - I_{\text{rec0}}$. Consequently, the ionic current I_{c}^{CC} remains small, yet it governs the recombination current, which is notably larger by a factor of $b \sim 10^3$. Therefore, in a small-signal analysis, the impedance of the $R_{\text{acc}} - C_{\text{acc}}$ branch in the CA model is equivalent to that of the $R_{\text{ion}} - C_{\text{ion}}$ branch in the CC model combined with the modulated current source I_{rec}, given by $Z_{\text{C}}^{\text{CC}} = Z_{\text{C}}^{\text{CA}}/(b+1)$. Moreover, the recombination current component aQ_{c} in the CC model corresponds to the R_{L}-L branch in the CA model. This indicates that a black-box approach like the CA model can effectively replicate the capacitive effects described by the CC model, which, due to its reliance on ionic modulated recombination, offers a more physically meaningful interpretation.

The beauty of the CC model consists in the direct physical interpretation of the inductive effects, which now depends majoritary on the ionic charge accumulation ($a \times Q_{\text{c}}$) instead of the ionic current ($b \times \frac{\partial Q_{\text{c}}}{\partial t}$). Furthermore, Eq. (3.23) is a tool to unify and describe the capacitive and inductive effects through the means of the recombination current.

3.4 SCAPS Simulations of Stationary J-V Characteristics

The Solar Cell Capacitance Simulator (SCAPS) program was primarily developed to analyze the solar cells families of $CuInSe_2$ and CdTe [121], through the current voltage simulations (IV) and capacitance voltage simulations (CV). The modern version of the program [122], received important updates [123, 124, 125, 126] which made it applicable to the crystalline and amorphous solar cells.

At the core of the SCAPS model are the two fundamental equations, represented by the Poisson equation and the continuity equation. Where, the Poisson equation 3.24 provides the relationship between the electrostatic potential and the charge density in the semiconductor, while the continuity equations for electrons and holes ensure the conservation of charge by accounting for current flow and recombination-generation processes.

The Poisson equation relates the electrostatic potential Φ to the charge density ρ. In the context of semiconductors, the charge density includes contributions from free electrons (n), holes (p) and ionized dopants. The equation is written as:

$$\nabla^2\Phi = -\frac{\rho}{\epsilon} \tag{3.24}$$

In this formalism, the gradient of the electrostatic potential (Φ) depends on the material permittivity (ϵ) and the charge density ρ.

$$\rho = q(p - n + N_D^+ - N_A^-)$$

Here, p is the hole concentration, n is the electron concentration, N_D^+ is the concentration of ionized donors, N_A^- is the concentration of ionized acceptors and q is the elementary charge.

The continuity equations describe the charge conservation of electrons and holes. They also account for the current flow and the recombination-generation processes in the semiconductor material. This way, the continuity equations for electrons and holes are written in the form:

$$\frac{\partial n}{\partial t} = \frac{1}{q}\nabla \cdot \mathbf{J}_n + G_n - R_n \tag{3.25}$$

$$\frac{\partial p}{\partial t} = -\frac{1}{q}\nabla \cdot \mathbf{J}_p + G_p - R_p \tag{3.26}$$

Where:

- n / p is the electron / hole concentration;
- $\mathbf{J}_n$ / $\mathbf{J}_p$ is the electron / hole current density;
- G_n / G_p is the generation rate of electrons / holes;
- R_n / R_p is the recombination rate of electrons / holes.

According to Marc Burgelman *et al.* in the article "Analysis of gradient band gap solar cells with SCAPS" from 2008, "SCAPS uses an exponentially fitted discretisation scheme to set up the equations for the electron and hole current $\mathbf{J}_n$ and $\mathbf{J}_p$ and for the continuity equation for electrons and holes, involving the Bernoulli function B(x) [127]" (Burgelman, 2008)[125].

The SCAPS program can efficiently simulate: the deep bulk levels, the optical generation, steady state direct current and alternating current, the interface states and band discontinuities. The IV and CV simulation of the solar cell is performed by specifying some typical parameters for the constituent layers: band gap (Eg) value, material permittivity (ϵ), conduction band effective density of states (N_C), valence band effective density of states (N_V), electron mobility μ_n, hole mobility μ_p, acceptor concentrations N_A, donor concentrations N_D, all traps (defects) N_t, etc.

Ab initio Investigation of Perovskite Materials and Interfaces

The materials and structures investigated in this thesis were anlized from the perspective of first principle calculations. The density functional theory (DFT) calculations were implemented with the help of the SIESTA code (see Chapter 3.2), which is the central method applied to perform material simulations and interface analysis among this chapter. The following sections will introduce the results regarding the 2D perovskite structures and the perovskite interfaces.

For the layered halide perovskites (2D), we analyze the electronic and stability properties due to the introduction of interlayer and small cations combined with different halogens. These results are published in the paper N. Filipoiu *et al., Optoelectronic and stability properties of quasi-2D alkylammonium based perovskites*, Physical Chemistry Chemical Physics, 25(4), 3323-3331 (2023), where we reveal a good agreement with the experimental results.

4.1 Low Dimensional Halide Perovskites (2D)

In the past decade, researchers have extensively analyzed 2D perovskites due to their enhanced stability when compared to the 3D perovskite materials. It was seen that by incorporating the large organic cations, the 2D structures were enforced with a higher hydrophobic resistance [46]. As mentioned in Section 2.1, there are two popular classes of layered perovskites. Here, we will focus this part of the study on the Ruddlesden-Popper (RP) halide perovskites.

The first principle calculations were performed using the SIESTA method [128], which relies on strictly localized basis sets, conferring this way a linear scaling of the system size with the computational time. For the system calculations, we employed the double-ζ polarized basis set combined with the local density approximation in the Ceperley and Alder [129] parametrization of the exchange-correlation functional.

The code uses the Troullier-Martins norm conserving pseudopotentials [130] accompanied by a k-space sampling of Monkhorst-Pack scheme of 5 × 1 × 5 with a 150 Ry mesh cutoff energy in the real space grid. The geometric relaxation of the atoms was performed until the forces decreased beyond the 0.15 eV/Å limit.

The electronic and stability properties of three 2D halide perovskites were investigated within three RP perovskite subclasses of the $(A)_2(A')_{n-1}Pb_nX_{3n+1}$ family (see Figure 4.1), where, we have analyzed the effects introduced by large interlayer cations (A) [butylammonium (BA), pentylammonium (PA), hexylammonium (HXA)] and small cations (A') [methylammonium (MA), formamidinium (FA), ethylammonium (EA), guanidinium (GA)].

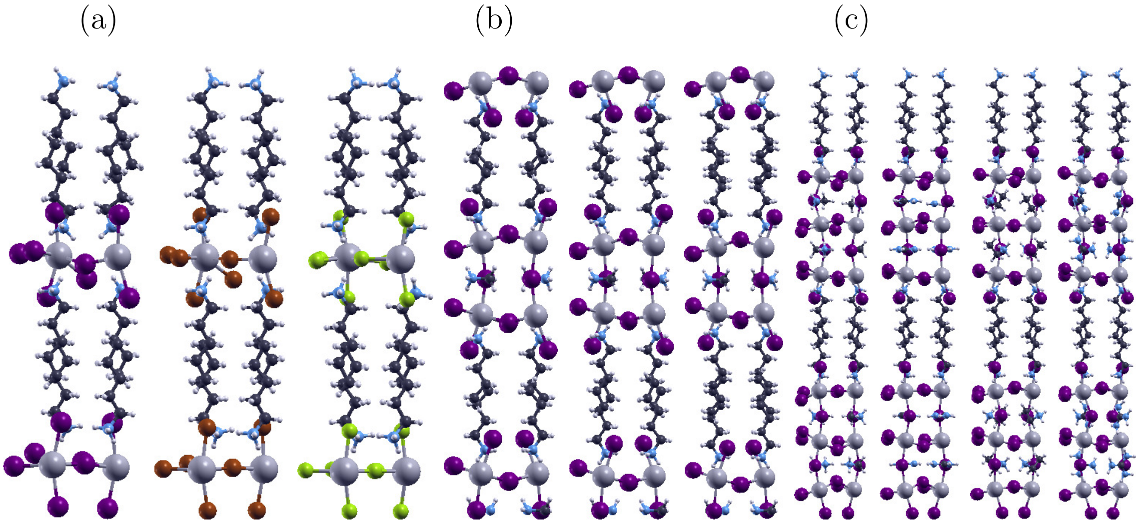

Figure 4.1: The three subclasses of 2D perovskite structures are: (a) $(PA)_2PbX_4$, with X = I, Br, Cl; (b) $(A)_2(MA)Pb_2I_7$, with A = BA, PA, HXA; (c) $(PA)_2(A')_2Pb_3I_{10}$, with A' = MA, FA, EA, GA. Reproduced with permission from Ref [131].

In order to properly represent the majority of the polycrystalline bulk perovskites, we have selected the orthorhombic centrosymmetric [132] space group for the three layered perovskites structures. The first group of structures is $(PA)_2PbX_4$ (X = I, Br, Cl) identified as X_4 and corresponds to the space group P_{bca}. The second group of structures is the $(A)_2(MA)Pb_2I_7$ where A = BA, PA, HXA, identified with the notation X_7, is corresponding to the C_{cmm} space group. The last group is the most complex and is represented by $(PA)_2(A')_2Pb_3I_{10}$ (A′ = MA, FA, EA, GA) identified with X_{10} and can be attributed to the A_{cam} space group. The number of atoms for the smallest unit cell is 180 (X_4) and the maximum number of atoms is found in the (PA-GA-X10) structure with 292 atoms.

Therefore, we intend to analyze the electronic properties by performing band structure calculations combined with partial density of state calculations (PDOS).

For the X_4 structures we observe the halogen effect, while for the X_7 we performed halogen, small cation and large cation substitutions. The obtained results are compared with the corresponding X_{10} structure calculations.

4.1.1 Electronic Properties of 2D Perovskites

The layered halide perovskite structures of X_4, X_7 and X_{10} groups allow a comprehensive study regarding the halogen, small cation and interlayer cation influence on the electronic properties. Starting with the projected band structures depicted in Figure 4.2 for the X_7 structures [$(PA)_2(MA)Pb_2X_7$ (X = I, Br, Cl)], which contain both small and long cations, we observe band structures that resemble previous reports on BA-based compounds [132]. The typical increase in the band gap with the halogen change from I→Br→Cl is present, showing in every case a direct band gap located at the Γ point.

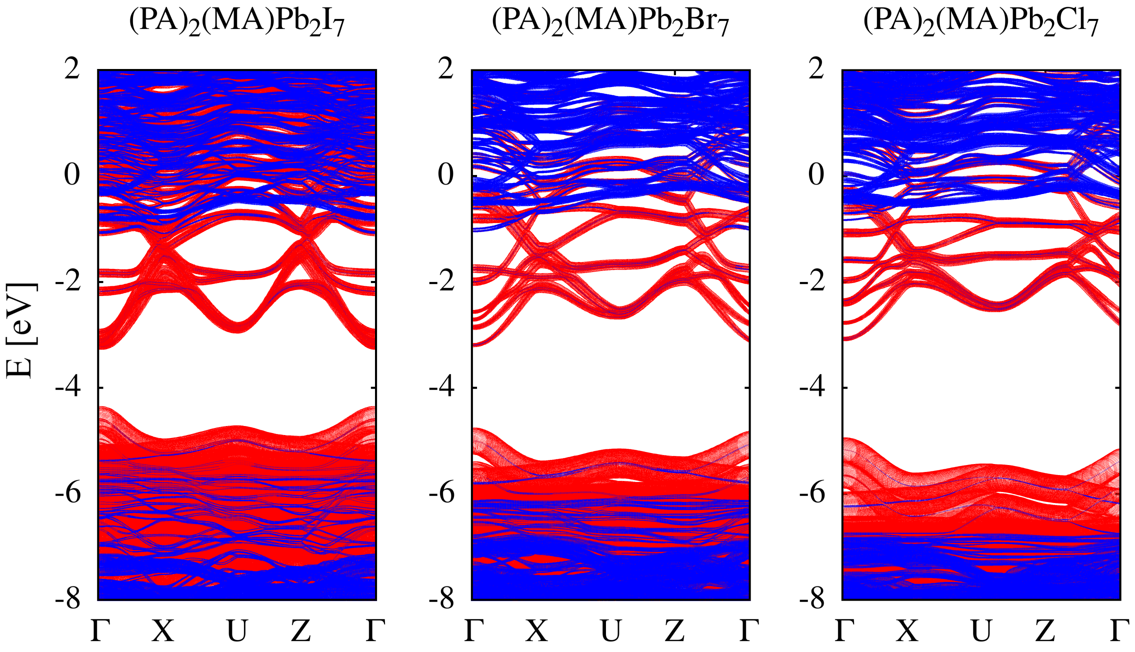

Figure 4.2: Projected band structures of $(PA)_2(MA)Pb_2X_7$ quasi-2D perovskites, showing the halogen influence on the band gap when changing X (I, Br, Cl). The red and blue colors represent the inorganic (Pb, X) and organic (C, N, H) contributions. Reprinted with permission from Ref [131].

Although the DFT methods tend to underestimate the band gap value, there is a clear trend regarding the predominant contribution of the inorganic component of the perovskite (represented in red) in the band gap, compared to the organic part contribution (represented in blue). Also, for the X_7 group of structures, one can observe the less recorded effect of the large cation on the band gap value.

In Figure 4.3 are represented the total PDOS results for the $(A)_2(MA)Pb_2X_7$

class of compounds where A = BA, PA, HXA and X = I, Br, Cl. By performing the partial density of states (PDOS) calculations for the X_7 group of structures with different long cations (BA, PA, HXA), mixed with different halogens (I, Br, Cl) we can see the band gap variation with the combined interlayer cation and halogen change.

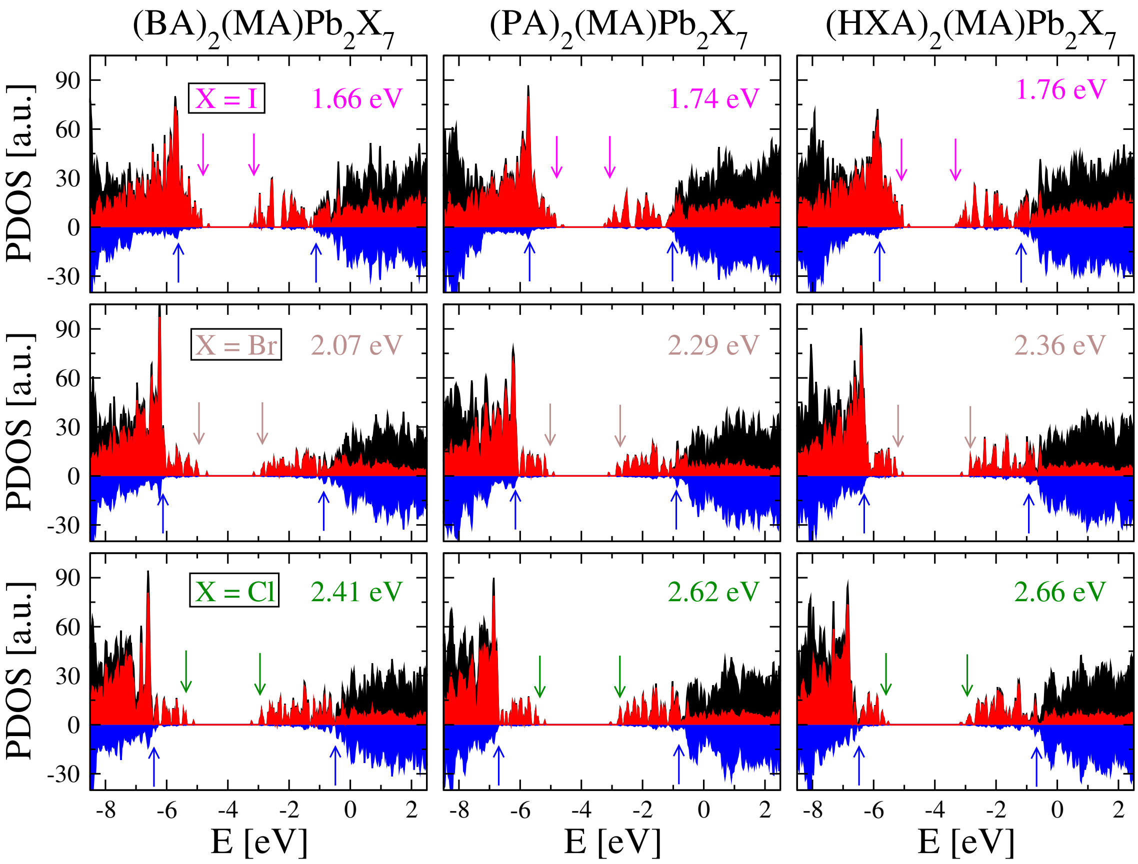

Figure 4.3: Partial density of states (PDOS) for $(A)_2(MA)Pb_2X_7$ structures (column-wise), with A = BA, PA, HXA and X = I, Br, Cl (row-wise): contributions from the inorganic layers (red) and organic layers (blue), the latter being mirrored for better visibility and the total DOS (black). The energy gaps in the PDOS are evidenced by arrows. These are strongly influenced by the halogen type, while they are slightly increasing as the size of the A-cation is getting larger. Included with permission from Ref [131].

Again, by marking the organic component with blue and the inorganic component with red, there are clear distinct energetic gaps when compared with the total contribution (with black). The two inorganic and organic parts of the 2D halide perovskite materials show that the inorganic part has a minimal contribution to the energetic gap of the total PDOS. These results are in perfect agreement with the ones presented in Fig. 4.2 and sustain the idea that the PDOS distribution of the 2D perovskites can also be tuned through the inorganic and organic component based on the mixture of halogen or small organic cations.

This way, the band gap of the 2D halide perovskites is highly influenced by the Pb-I inorganic contributions. On the other hand, one can also note two important aspects when substituting the long organic cations and the halogens. The first and most important energetic trend is due to the long cation substitution, where we observed a higher band gap value for the molecules with longer chains of C-H atoms. The second energetic trend is linked with the halogen substitution, the band gap will decrease when the atomic number of the halogen is increasing. These results can also sustain the band gap optimization for a suitable tandem PSC where the stability can be enhanced by the long organic cations.

When removing the small organic cations from the X_7 group of 2D perovskites, the X_4 group is obtained. This class of layered halide perovskites presents a higher quantum confinement when compared with the X_7 group, which can be linked with the removal of the MA small cations. In Figure 4.4 (a) is presented a more detailed effect, which also reveals the halogen effect on the energetic gap.

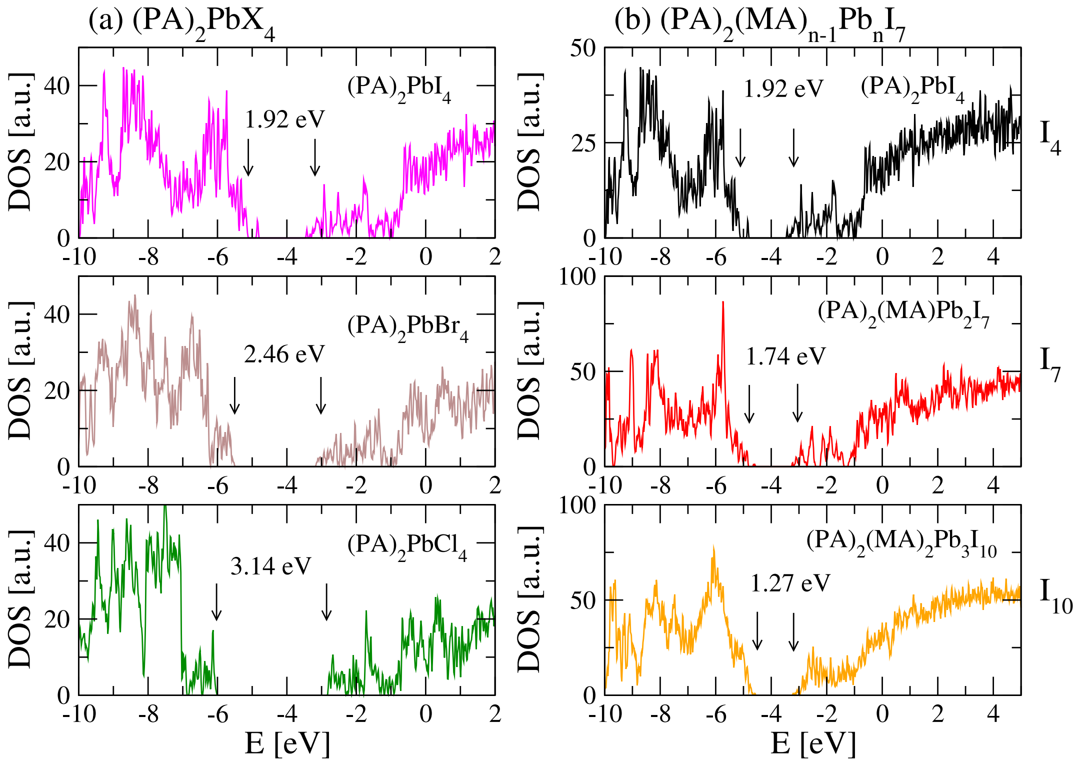

Figure 4.4: Comparing the band gap variation for X_4 and X_7 quasi-2D perovskite classes: (a) $(PA)_2PbX_4$, with X = I, Br, Cl and (b) $(PA)_2(MA)_{n-1}Pb_nI_{3n+1}$, with n = 1, 2, 3. The X_4 class shows a similar trend as for the X_7 class as the halogen is changed, while increasing n by the amount of MA the band gap is decreasing in the sequence $I_4 \searrow I_7 \searrow I_{10}$. Incorporated with permission from Ref [131].

Another important aspect is that the band gap is directly linked with the number of layers. These aspects can be seen in Figure 4.4 (b) where, the increasing number of layers $X_4 \rightarrow X_7 \rightarrow X_{10}$ reduces the quantum confinement and therefore the band gap is decreasing.

4.1.2 Stability Assessment in 2D Perovskites

Starting with the most probable degradation mechanism of the 3D organo-halide perovskites, the evaluation of layered organo-halide perovskites stability is revealed using the formation energy. The 3D perovskite degradation can be divided in *intrinsic* degradation and *extrinsic* degradation mechanisms [34, 133]. The intrinsic degradation mechanism accounts for the degradation mechanisms which occurs due to the electrical or thermal stress. On the other hand, the extrinsic mechanism is related to the processes where external elements like water molecules or oxygen are involved.

We address the degradation based on the *intrinsic* mechanism, by analyzing the two principal decomposition pathways which produces a solid precipitate and gaseous phase:

$$(\mathrm{A})_2(\mathrm{A}')_{n-1}\mathrm{Pb}_n\mathrm{X}_{3n+1} \rightarrow 2\tilde{\mathrm{A}} + (n-1)\tilde{\mathrm{A}}' + (n+1)\mathrm{HX} + n\mathrm{PbX}_2 \tag{4.1}$$

The reaction pathway for the *extrinsic* degradation mechanism considers the impact of molecular oxygen and is described using the equation:

$$\begin{aligned}(\mathrm{A})_2(\mathrm{A}')_{n-1}\mathrm{Pb}_n\mathrm{X}_{3n+1} + \left(\frac{n+1}{4}\right)\mathrm{O}_2 &\rightarrow 2\tilde{\mathrm{A}} + (n-1)\tilde{\mathrm{A}}' \\ &+ \left(\frac{n+1}{2}\right)\mathrm{H}_2\mathrm{O} + \left(\frac{n+1}{2}\right)\mathrm{X}_2 + n\mathrm{PbX}_2 \end{aligned} \tag{4.2}$$

Where, we associate for the deprotonated, electrically neutral molecules corresponding to the large and small cations the notations $\tilde{\mathrm{A}}$ and $\tilde{\mathrm{A}}'$.

According to C. Van de Walle [134], the formation energy (E_f) of a point defect can be defined using the equation:

$$E_\mathrm{f} = E_\mathrm{prv}^\mathrm{def} - E_\mathrm{prv}^\mathrm{ideal} - \sum_i n_i \mu_i \tag{4.3}$$

Here, the term $E_\mathrm{prv}^\mathrm{def}$ is the total energy of the system containing the defect and $E_\mathrm{prv}^\mathrm{ideal}$ is the ideal crystalline structure (without the defect). In this context, $n_i < 0$ represents the number of the removed atoms and μ_i accounts for the chemical potentials of the extracted species (i = I, Br, Cl or Pb). The μ_i upper limits are equal to half of the total energy of the X_2 molecule for a halogen ($\mu_\mathrm{X} \leq \mu_{\mathrm{X}[\mathrm{X}_2]}$)

or the chemical potential of bulk Pb ($\mu_{\mathrm{Pb}} \leq \mu_{\mathrm{Pb[bulk]}}$). In this way, we investigate single-vacancies, i.e. $n_i = -1$ and we consider halogen and Pb rich conditions for the respective vacant species, in order for the chemical potentials to become equal to $\mu_{\mathrm{X[X_2]}}$ and $\mu_{\mathrm{Pb[bulk]}}$.

The layered organo-halide perovskite (2D) structures represented by the family of $(\mathrm{A})_2(\mathrm{A'})_{n-1}\mathrm{Pb}_n\mathrm{X}_{3n+1}$ structures, are analyzed in accordance with the intrinsic and extrinsic degradation pathways. Therefore, Eqs.4.1-4.2 are implemented for the three subclasses X_4 , X_7 , X_{10} represented by $(\mathrm{PA})_2\mathrm{PbX}_4$, $(\mathrm{A})_2(\mathrm{MA})\mathrm{Pb}_2\mathrm{X}_7$ and $(\mathrm{PA})_2(\mathrm{A'})_2\mathrm{Pb}_3\mathrm{I}_{10}$ structures. In this way, we determine the measured endothermic reaction energies (from Tables 4.1 and 4.2), by considering a structure for every class as reference one can see the effect of the halogen, small or large organic cation on the degradation mechanism.

Table 4.1: Relative stability of X_4, X_7 and X_{10} quasi-2D perovskites with respect to the intrinsic degradation mechanism [Eq. (4.1)]. Reproduced with permission from Ref [131].

(a) Changing the halogen in X_4 structures:

2D perovskites (X_4)	**I**	**Br**	**Cl**
$(\mathrm{PA})_2\mathrm{PbX}_4$	REF	+5%	+3%

(b) Changing the large cation (A) in X_7 structures:

2D perovskites (X_7)	**I**	**Br**	**Cl**
$(\mathrm{BA})_2(\mathrm{MA})\mathrm{Pb}_2\mathrm{X}_7$	REF	+4%	-3%
$(\mathrm{PA})_2(\mathrm{MA})\mathrm{Pb}_2\mathrm{X}_7$	+3%	+8%	+2%
$(\mathrm{HXA})_2(\mathrm{MA})\mathrm{Pb}_2\mathrm{X}_7$	+4%	+7%	-3%

(c) Changing the small cation (A') in X_{10} structures:

2D perovskites (X_{10})	**MA**	**FA**	**EA**	**GA**
$(\mathrm{PA})_2(\mathrm{A'})_2\mathrm{Pb}_3\mathrm{I}_{10}$	REF	+6%	+1%	+9%

The approach is to use one compound as reference from each class and compare it to the corresponding systems. In this manner, we can point out the influence of the halogen, small and large cations on the degradation processes. For the intrinsic degradation mechanism in Table 4.1, we see that replacing I with Br leads to increased stability (4%–8%), which is also reported in the case of the extrinsic degradation mechanism (5%–7%) in Table 4.2. At the same time, by substituting iodine with chlorine induces a stability decrease, similarly to the intrinsic degradation pathway (-3%–2%) for the X_7 family.

Compared with the X_4 group, the stability of chlorine based compounds is located between the iodine and bromine based structures. This is in opposition with the extrinsic degradation mechanisms, where the chlorine utilization is beneficial and we see an improvement when comparing it to the iodine based systems, which is similar to the one of bromine based structures of (5%–6%).

Table 4.2: Complementary to Table 4.1, the relative stability of X_4, X_7 and X_{10} quasi-2D perovskites with respect to the extrinsic degradation mechanism [Eq. (4.2)], involving molecular O_2. Reproduced with permission from Ref [131].

(a) Changing the halogen in X_4 structures:

2D perovskites (X_4)	**I**	**Br**	**Cl**
$(PA)_2PbX_4$	REF	+5%	+6%

(b) Changing the large cation (A) in X_7 structures:

2D perovskites (X_7)	**I**	**Br**	**Cl**
$(BA)_2(MA)Pb_2X_7$	REF	+5%	+6%
$(PA)_2(MA)Pb_2X_7$	∼0%	+5%	+5%
$(HXA)_2(MA)Pb_2X_7$	+1%	+7%	+6%

(c) Changing the small cation (A’) in X_{10} structures:

2D perovskites (X_{10})	**MA**	**FA**	**EA**	**GA**
$(PA)_2(A')_2Pb_3I_{10}$	REF	+2%	∼0%	+3%

Although the studied structures are in the class of layered organo-halide perovskites(2D), there is a similar behaviour of the stability with respect to the halogen type to 3D perovskites [34] family: it was established for the intrinsic mechanism, that the stability evolves in the sequence I $\nearrow$ Cl $\nearrow$ Br [$(PA)_2PbX_4$] and Cl $\nearrow$ I $\nearrow$ Br [$(A)_2(MA)Pb_2X_7$], compared with the extrinsic mechanism where the increase starts from I $\nearrow$ Cl $\approx$ Br. The same behaviour was also reported by other theoretical and experimental investigations described in Ref. [34], where it is underlined the picture of an enhanced stability for Br-based perovskites in comparison to I-based ones. Similarly, the studies conducted by Pistor et al. [135], Brunetti et al. [136], Ciccioli et al. [137] and McGovern et al. [138] observed a similar behaviour for both 3D and 2D perovskites. Some 3D perovskite structures were shown to possess a lower stability (e.g. based on hydroxylammonium and hydrazinium), which was also experimentally confirmed. On the other side, a very recent theoretical and experimental study [139], confirms that the $MA_{1-x}EA_xPbI_3$ mixed perovskite system, identified in our previous study [34] is a strong candidate for improved stability and photovoltaic performance.

When comparing the stability results for the substitutions of the large cations in the sequence (BA, PA, HXA), there is minimal variation of the relative stability. What is clear is that replacing MA with other small cations (FA, EA, GA) will produce a stability increase. This observation can be related to the deprotonation energies of the small cations explained by the reaction: $\tilde{A}'X \rightarrow A' + HX$. When evaluating the deprotonation energy values for the small organic cations and the large interlayer organic molecules, we see that the small cations deprotonation energy values are fluctuating from 0.55 eV (MA), 1.24 eV (EA), 1.41 eV (FA) and 2.09 eV (GA), once for the large cations (BA, PA, HXA) we obtain a similar result, ∼0.75 eV. In this way, we can assume that there is a strong correlation between the stability of the 2D perovskites and the value obtained for the deprotonation energy in both intrinsic and extrinsic degradation mechanisms. In relation to these aspects, we may observe the principal role of the small organic cations which can introduce a higher stability state to the overall device.

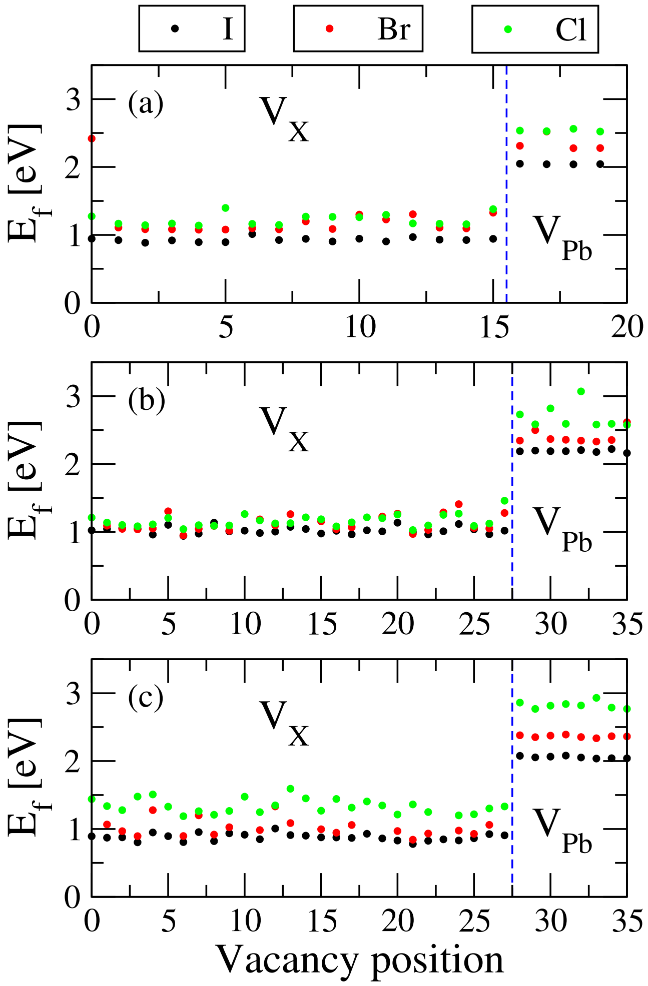

Figure 4.5: Formation energies of halogen (X = I, Br, Cl) combined with Pb single vacancies, for the 2D perovskite classes: (a) $(PA)_2PbX_4$, (b) $(PA)_2(MA)Pb_2X_7$ and (c) $(PA)_2(GA)Pb_2X_7$. Reprinted with permission from Ref.[131]

There are also other degradation mechanisms which can affect the stability. That is why the point defect analysis can reveal important aspects related to the ion migration or stability. To this end, we implement the investigation of the formation energies of single-vacancies of lead and halogens, this way revealing the trends attributed to the halogens and small cations. The formation energy, from Eq. (4.3), provides the probability for a certain type of defect to be formed. Figure 4.5 shows the formation energies for all possible halogen and lead vacancy sites for the $(PA)_2PbX_4$, $(PA)_2(MA)Pb_2X_7$ and $(PA)_2(GA)Pb_2X_7$ structures. Showing a small difference between the halogen types, the formation energies indicate a trend where: $E_\mathrm{f}^\mathrm{Cl} > E_\mathrm{f}^\mathrm{Br} > E_\mathrm{f}^\mathrm{I}$. This observation is more clearly visible in the structures containing GA, where a higher formation energies is revealed, as compared to MA molecule or the X_4 class. These results are also sustained by previous investigations concerning bromide/ iodide 3D halide perovskites [140]. Furthermore, the same behaviour is noticed for Pb vacancies, for bromine and chlorine based perovskites where the Pb vacancy will also increase the formation energy.

4.2 Interfaces with Perovskites

As already mentioned in Chapter 2, the interfaces play a crucial role in the PSCs functionality, the electron transporter layer (ETL) and hole transporter layer (HTL) together with the perovskite material are highly influencing the overall performance and stability of the solar cell. For these reasons, we stress these aspects by studying the point defect influence on the individual interfaces of ETL-PRV and PRV-HTL.

SIESTA was the selected DFT method for optimizing the bulk materials and also for simulating the defected and ideal interfaces. We have benefited from the linear time scalability of the SIESTA program with the number of atoms (in the system) in order to perform the calculations. For both type of simulations (bulk or interfaces) we have used the Ceperley and Alder [129] parametrization of the local density approximation (LDA) combined with the Troullier-Martins [130] norm-conserving pseudopotentials. The selected basis set was a double-ζ polarized (DZP) basis set with a meshcutoff energy of 300 Ry for bulk materials and 150 for interfaces, combined with a Brillouin zone sampling of $5 \times 5 \times 5$ Monkhorst-Pack grid. The relaxations were performed until the system residual forces where less than 0.04 eV/Å. Due to the typical DFT underestimation of the bang gap, we employed the DFT+U method for the structures where the underestimation impeded the analysis.

Beyond the clear role in charge collection and charge separation, the selection of the HTL and ETL materials can play a crucial role in ion migration reduction. As presented in Chapter 3.3, the ion migration is the principal degradation mechanism, associated with the intrinsic degradation of the PSCs. Due to the incorporated organic molecules in the halide perovskites, there was a common approach in using the organic Spiro-OMeTAD as HTL for PSCs. This was later proven to be a poor decision, not due to the high productions costs, but mainly due to the ion permeability. For these reasons, more recent studies introduced in their works the inorganic crystalline compounds (NiO, Cu_2O, etc) [141, 142].

Although there are other available materials with applications in the photovoltaic field [80, 81, 82], the advantages of the oxide materials, beyond the ion migration reduction, are also the procesability, being available for low temperature solution-based deposition techniques or, alternatively, can be included in inverted PSC structures [143]. One can note, that ionic migration is less effective in the ETL, which is typically made from crystalline materials like TiO_2, ZnO, SnO_2 etc. A clear aspect is that both ETL and HTL are equally responsible for the PSC performance.

4.2.1 Bulk Materials Optimizations

In this section, we will focus on the *ab initio* optimization of the constituent materials of the two principal interfaces of a PSC, namely the PRV-HTL reproduced with the MAPI@Cu_2O heterostructure and the PRV-ETL represented by MAPI@TiO_2 slab. Therefore, we start with the structural optimization and electronic band structure characterization of the interfaces constituent materials (MAPI, Cu_2O, TiO_2).

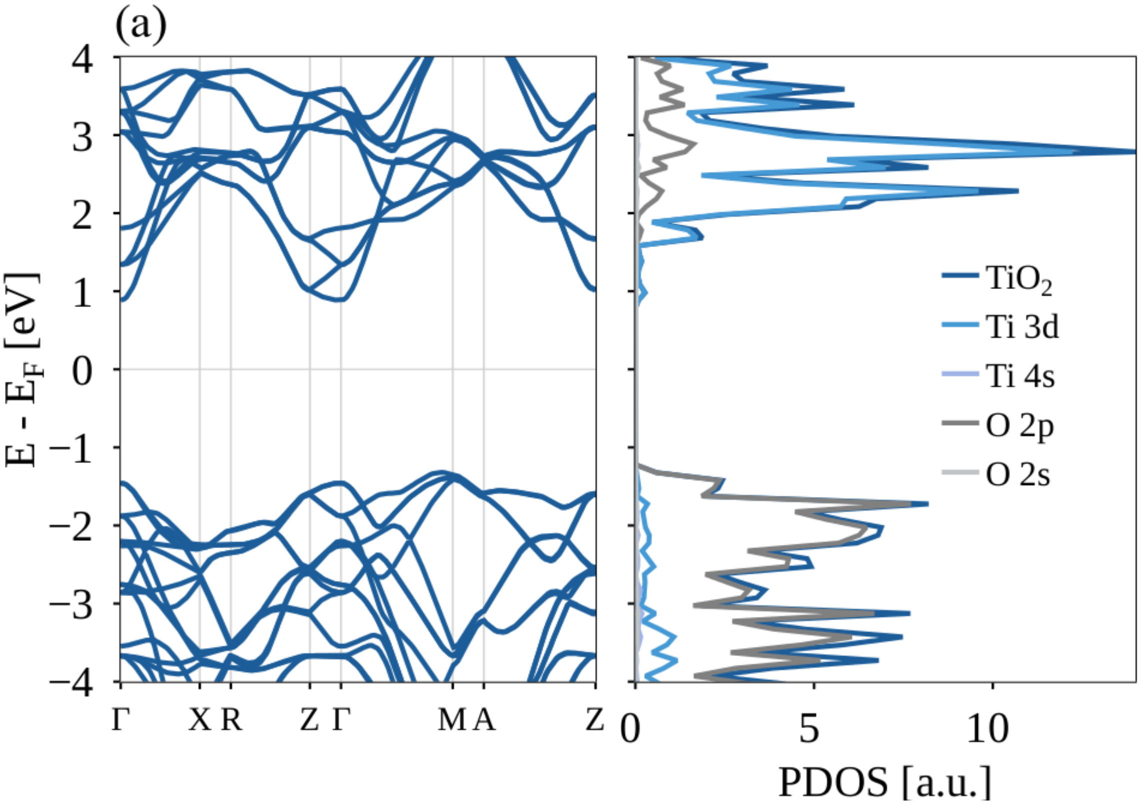

Figure 4.6: Band structure and PDOS simulations for the anatase phase of the TiO_2 material, showing an electronic band gap $E_g = 1.96$ eV. Reproduced with permission from Ref. [144].

From the three possible configurations of the titanium dioxide (TiO_2), we selected the anatase crystalline structure which is more commonly reported in the experimental studies. Compared with the rutile and brookite phases, the anatase phase has a unique tetragonal structure attributed to the $I4_1/amd$ space group, where the unit cell is composed of four titanium atoms and eight oxygen atoms. The TiO_2 oxide is a semiconductor material which shows an experimental band gap value of 3.22 eV [145].

In Figure 4.6, the titanium dioxide band structure shows an indirect alignment of the conduction and valence bands. Using plain DFT, the calculated energetic band gap value is $E_g = 1.96$ eV. The minimum value of the conduction band (CB) is situated at the Γ point, with the maximum value of the valence band (VB) located in the proximity of the M point which is in good agreement with other studies [146]. From the PDOS representation, we see the principal orbital contributions to the edges of the band gap are represented by Ti 3d for CB and O 2p for VB.

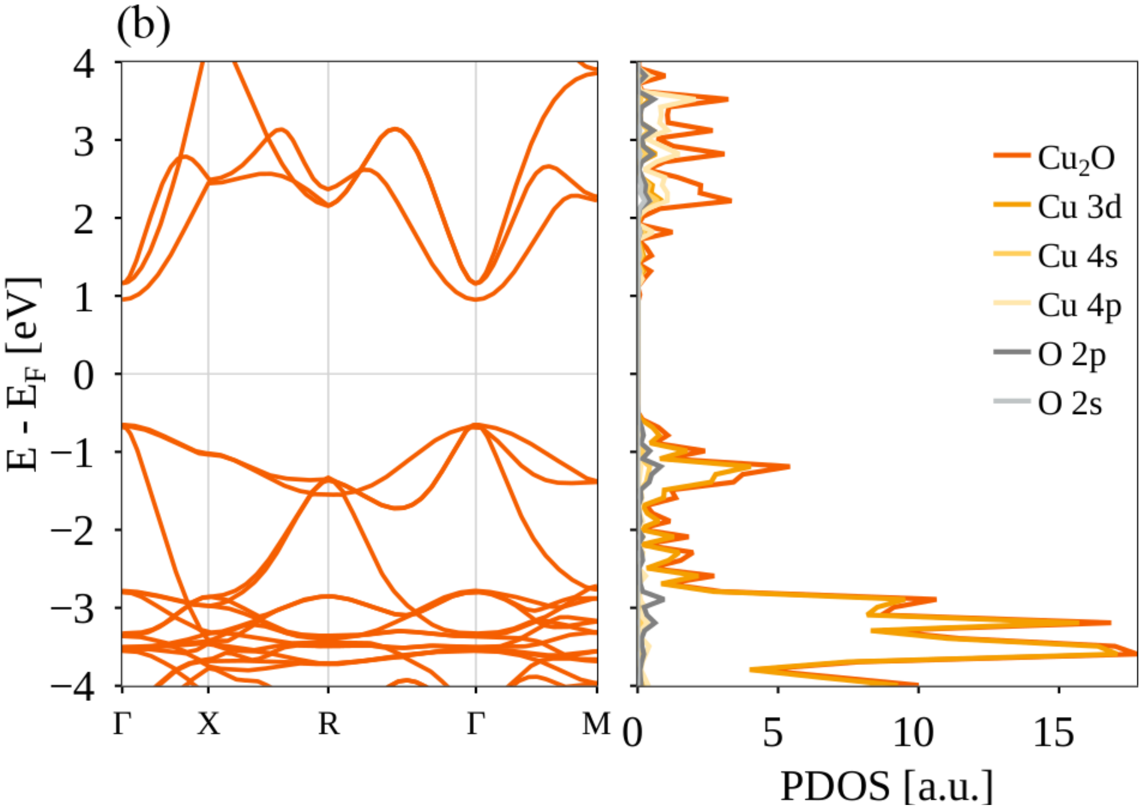

Figure 4.7: Band structure and PDOS simulations for the Cu_2O material, showing a band gap value of $E_g = 1.49$ eV. Reproduced with permission from Ref. [144].

For the cuprous oxide (Cu_2O), we have used the cubic crystalline structure associated to the $Pn\bar{3}m$ space group. Compared with the experimental band gap, the value of 2.1 eV [147] was partially reproduced by using the DFT+U method, where we applied U = 8 eV potential on the Cu 3d orbitals combined with an 12 eV on 2p Oxygen orbitals. The PDOS results from Figure 4.7 show that the Cu 3d and Cu

4s orbitals bring the highest contributions to the band edges, where the 3d orbitals are contouring the valence band and the 4s orbitals contour the conduction band.

MAPI perovskite is known to be crystallizing in three phases: cubic, orthorhombic and tetragonal. We have used the last two structures which possess 48 atoms in the unit cell and they show similar optoelectronic results (1.6 eV) when comparing the band gap values.

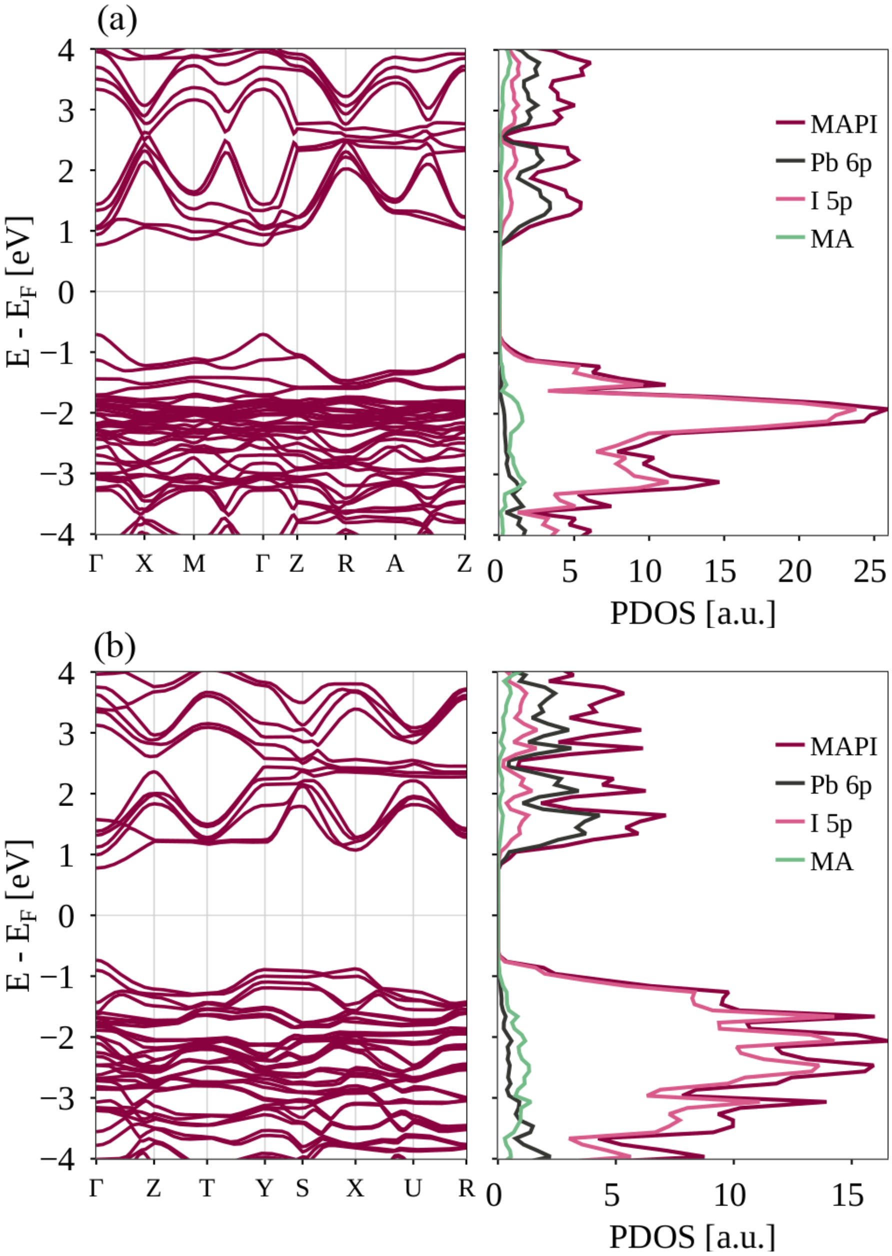

Figure 4.8: Band structure and PDOS calculations for tetragonal (a) and orthorhombic (b) MAPI ($CH_3NH_3PbI_3$) perovskite. Incorporated with permission from Ref. [144].

The calculated band gap value is in good agreement with the experimental work.

This behaviour results from a fortouis cancellation of the DFT (LDA) underestimation and the lack of spin orbit coupling [148]. For both phases the PDOS results show the principal contributions of the I-5p and Pb-6p orbitals.

4.2.2 Ideal Interfaces with Perovskite Materials

Based on the optimized materials (MAPI, TiO_2, Cu_2O), we reproduced the two active interfaces of a PSC. The first interface consists of a tetragonal MAPI perovskite layer containing 108 atoms interfaced with a titanium dioxide (TiO_2) layer comprising 135 atoms. This slab represents the PRV-ETL interface (I_1). The supercell dimensions for this interface are $a = b = 11.05$ Å and $c = 39.67$ Å, which were obtained by translating the unit cell of the MAPI tetragonal perovskite along the diagonal, aligning the Pb atoms at the corners of the 11.05 Å cube. The TiO_2 unit cell was then multiplied to match the new PRV unit cell dimensions.

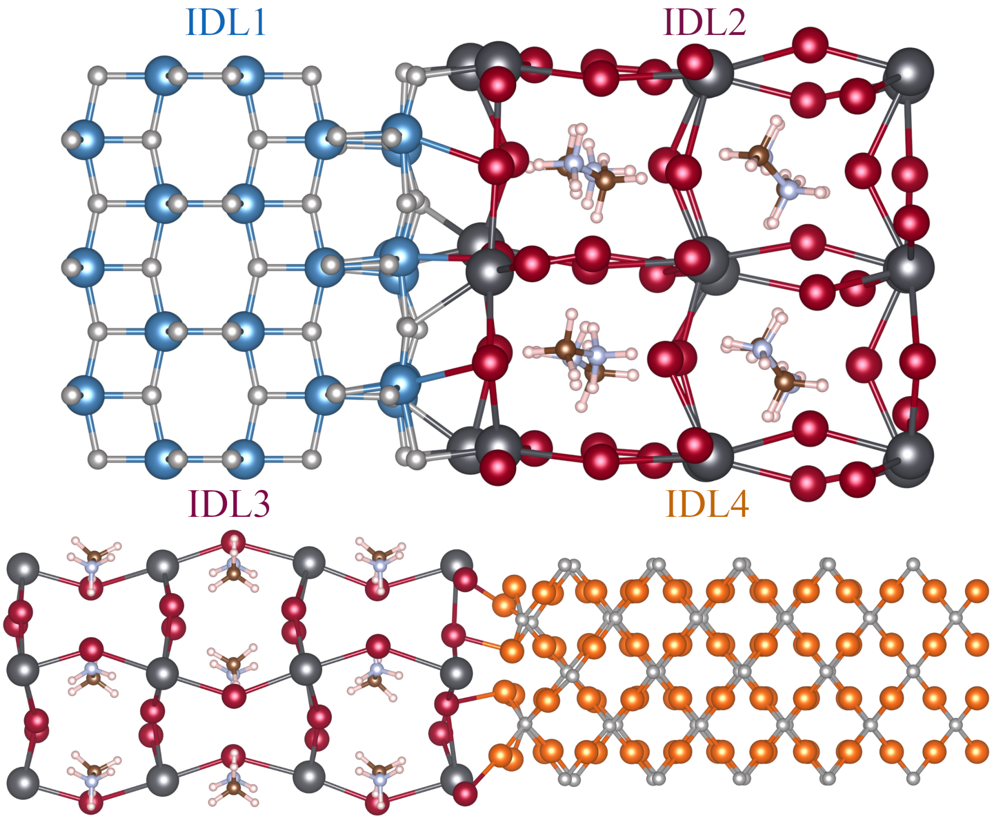

Figure 4.9: Geometry optimizations of heterostructures, for MAPI@TiO2 at the top and MAPI@Cu2O at the bottom of the figure. The IDL1, IDL2,IDL3 and IDL4 labels will be detailed in Chapter 6 where we correlate the DFT results with the device analysis. This figure is reproduced with permission from Ref. [144]

The second heterostructure reproduces the PRV-HTL interface (I_2), being composed of 78 atoms for the orthorhombic perovskite (MAPI) layer and 140 atoms in the cuprous oxide layer. The supercell dimensions after scaling the perovskite to the double value of the oxide unit cell dimensions are a=b=9.08 Å and c= 55 Å with 15 Å of vacuum. The geometrical relaxation of the interfaces was performed with SIESTA and following to the relaxation of these structures, we considered them as ideal interfaces where no point defects are present.

4.2.3 Influence of Defects on the Interfacial Band Alignment

Although PSC devices may inherently contain some unintentional point defects from the deposition process, these defects can be advantageous for inducing the material's *p/n* character. Therefore, carefully selecting the type and quantity of defects can enhance the overall stability of PSCs. *Ab initio* methods provide an opportunity to apply defect engineering techniques to ideal, relaxed interfaces. Starting from these ideal interfaces, we have analyzed the effect of vacancies on the PDOS band alignment, generating 20 random cases for each vacancy type.

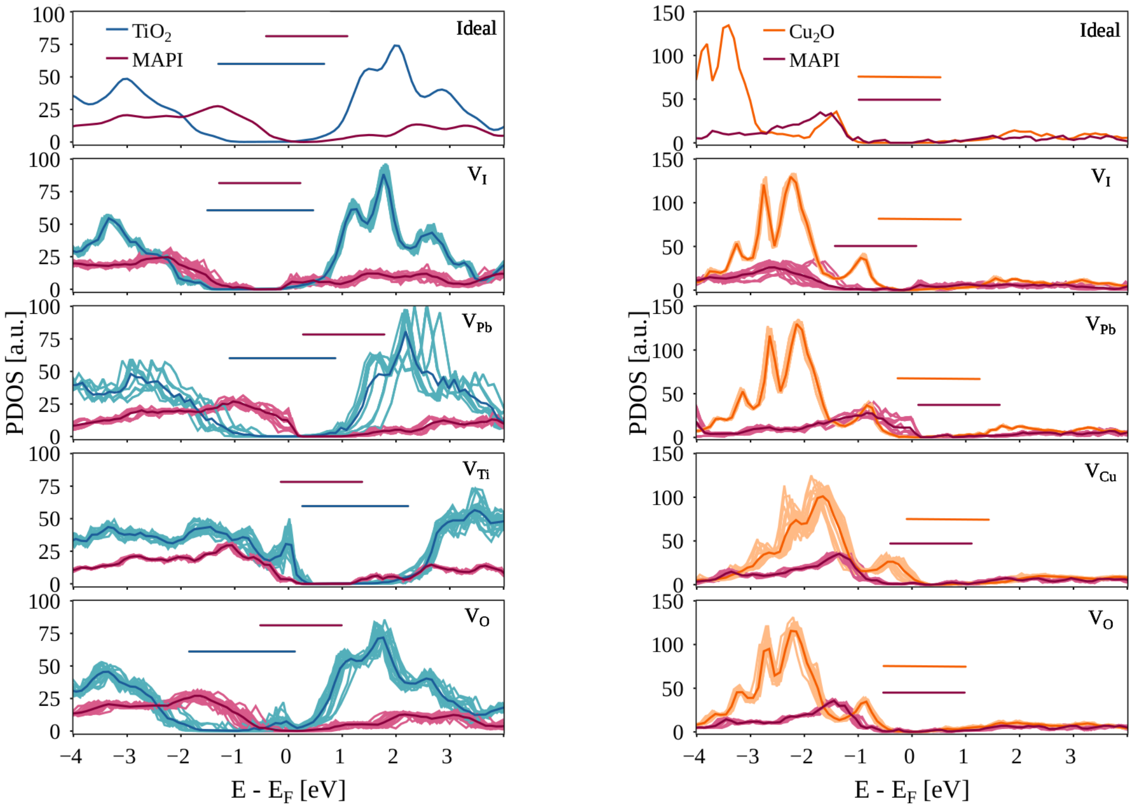
(a) MAPI@TiO_2 (b) MAPI@Cu_2O

Figure 4.10: Band alignment at (a) MAPI@TiO_2 and (b) MAPI@Cu_2O interfaces obtained from the PDOS of the materials: ideal systems (upper plots), followed by structures with V_I, V_{Pb}, V_{Ti} and V_O. A number of 20 disorder realizations are depicted together with the averaged PDOS. Reproduced with permission from Ref. [144].

For the perovskite material, we have analyzed the lead (V_{Pb}) and iodine (V_{I}) vacancies and for the oxides we have analyzed the titanium V_{Ti}, copper V_{Cu} and oxygen V_{O} vacancies. Based on the interface particularity, we have analyzed different vacancy concentrations, for the PRV-HTL interface: $1/12 = 8.33\%$ V_{Pb}, $2/32 = 6.25\%$ V_{I}, $2/45 = 4.44\%$ V_{Ti} and $4/90 = 4.44\%$ V_{O}, for the PRV-ETL the concentrations are: $1/8 = 12.5\%$ V_{Pb}, $1/22 = 4.55\%$ V_{I}, $5/96 = 5.26\%$ V_{Cu} and $2/44 = 4.55\%$ V_{O}.

Depending on the impurity type, there are different doping effects occurring in the interface. These effects can even change the n or p type character of the layers. In both oxides, the oxygen vacancies V_{O} generates donor centers, while the metal vacancies V_{Ti} and V_{Cu} creates acceptor centers. A similar trend is observed for the perovskite, where for MAPI perovskite, V_{Pb} induce a p-type character, while V_{I} introduce an n-type character.

When analyzing the different disorder calculations, it is clear that based on their relative position and the proximity to the interface, the PDOS results can reveal slightly different characteristics. What is important, is that for all the 20 cases calculated for each vacancy type, we see a consistent trend. If we perform a more detailed inspection of Fig. 4.10a and Fig. 4.10b we see that MAPI PDOS is shifted in opposite directions for V_{I} and V_{Pb}, followed by a similar effect observed for TiO_2 when V_{Ti} or V_{O} are present. High defect concentrations can enhance the band offsets or can even locally reverse the band alignment. The same behaviour is evidenced for the MAPI@Cu_2O interface in Fig. 4.10b.

Dynamic Hysteresis Effects and Small Signal Analysis in PSCs

Starting from the typical features observed in experimental measurements, we will perform both large- and small-signal analyzes. In the large-signal analysis, the effects of scan rate and characteristic time scales on the magnitude of hysteresis will be demonstrated using J-V simulations under varying voltage poling and illumination conditions. In contrast, the small-signal analysis reveals the capacitive and inductive effects, which are attributed to two distinct recombination processes: the influence of the bulk electric field and ionic-induced defect recombination, respectively. These J-V characteristics are supported by experimental data in Ref. [79].

In order to reproduce the hysteretic effects of a PSC, we defined a set of equivalent circuit parameters assigned with the reference PSC. In the following discussions, some of these parameters will be adjusted to highlight different behaviours related to capacitive and inductive effects. In the published paper (Filipoiu N. *et al.*, 2022), "the following circuit model parameters are used in the reference PSC configuration: series resistance $R_\mathrm{s} = 50\ \Omega$; shunt resistance $R_\mathrm{sh} = 6\ \mathrm{k}\Omega$; photogenerated current $I_\mathrm{ph} = 2$ mA; diode parameters $I_\mathrm{s} = 10^{-13}$ A and $n_\mathrm{id} k_\mathrm{B} T = 40$ meV; geometrical capacitance $C_0 = 0.079\ \mu$F; PSC area $\mathcal{A} = 0.09\ \mathrm{cm}^{-2}$; absorber (ionic) resistance $R_\mathrm{a} = 500\ \mathrm{k}\Omega$; ionic capacitor parametrization in Eq. (3.9) (one capacitor case) $\bar{C}_{01} = 10\ \mu$F, $\bar{C}_{11} = 10^{-14}\ \mu$F, $n_c k_\mathrm{B} T = 26$ meV. In this initial PSC configuration only the capacitive effects are accounted for ($a_i = 0$, $b = 1000$), while the ionic capacitor losses are initially neglected ($R_{1,2} \to \infty$). The parametrization of I_rec as a function of I_ph is given by: $\lambda_0 = 0.5$, $\lambda_{a_{0i}} = 10$ mA, $\lambda_{a_i} = 50$, $\lambda_b = 500\ \mathrm{mA}^{-1}$. A typical scan rate $\alpha = 20$ mV/s is used in the subsequent large signal analysis" [79].

5.1 Large Signal Analysis

When performing large-signal analysis, J-V simulations are crucial for understanding the effects of different voltage poling and illumination conditions. Typically, dynamic J-V measurements are conducted by recording the current at each voltage value during a reverse-forward (R-F) scan. This involves varying the applied voltage in a forward loop from the initial voltage to the short-circuit value and then returning from the short-circuit voltage to the initial value in the reverse loop. These J-V simulations are fundamental in evaluating the power conversion efficiency (PCE) of a PSC [149] and can also uncover significant degradation characteristics [150].

Different pre-poling conditions reveal opposite effects; when using a positive poling voltage V_{pol} the J-V curve poses a normal hysteresis, while the negative poling voltage $V_{\text{pol}} < 0$ can even invert the hysteresis.

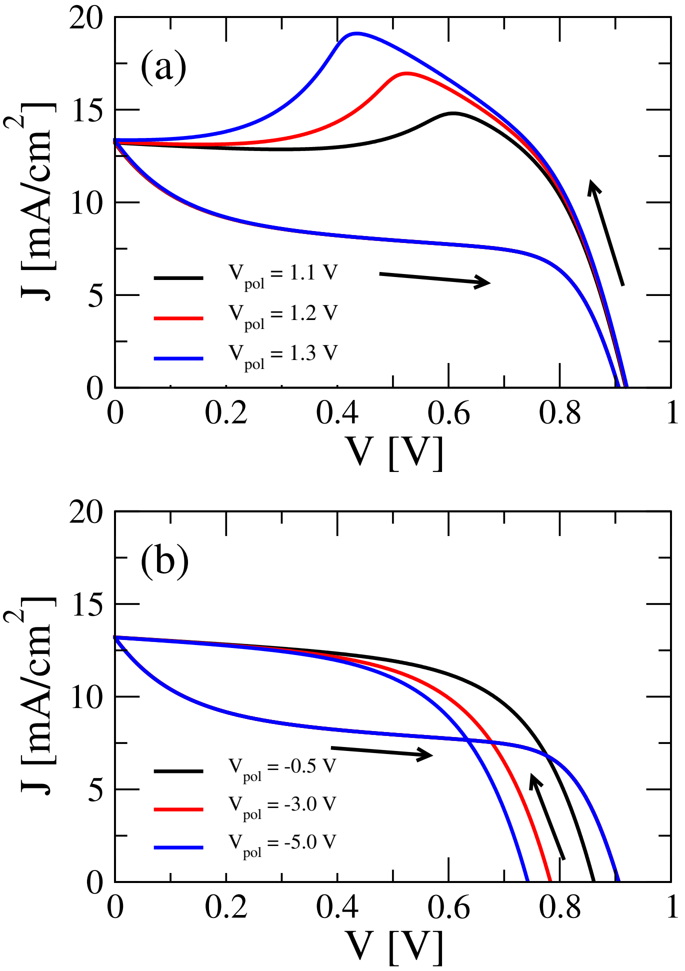

Figure 5.1: J-V calculations for positive and negative poling conditions: (a) $V_{\text{pol}} > V_{\text{oc}}$ and (b) $V_{\text{pol}} < 0$, showing normal and mixed (inverted) hysteresis, respectively. Incorporated with permission from Ref. [79].

In Figure 5.1 (a) we see the normal hysteretic effect, which reveals an increasing current bump on the reverse scan, when the applied V_{pol} takes values from 1.2 V to 1.6 V, which is in good agreement with other J-V measurements [61, 63, 62]. The negative poling from -1.5 V to -5 V (see Fig. 5.1 (b)) shows an inverted hysteresis which is induced by the large recombination, visible in the reduced reverse current. This inverted hysteresis emerged due to the unfavorable electric field produced by the initial ionic displacement during the pre-poling phase.

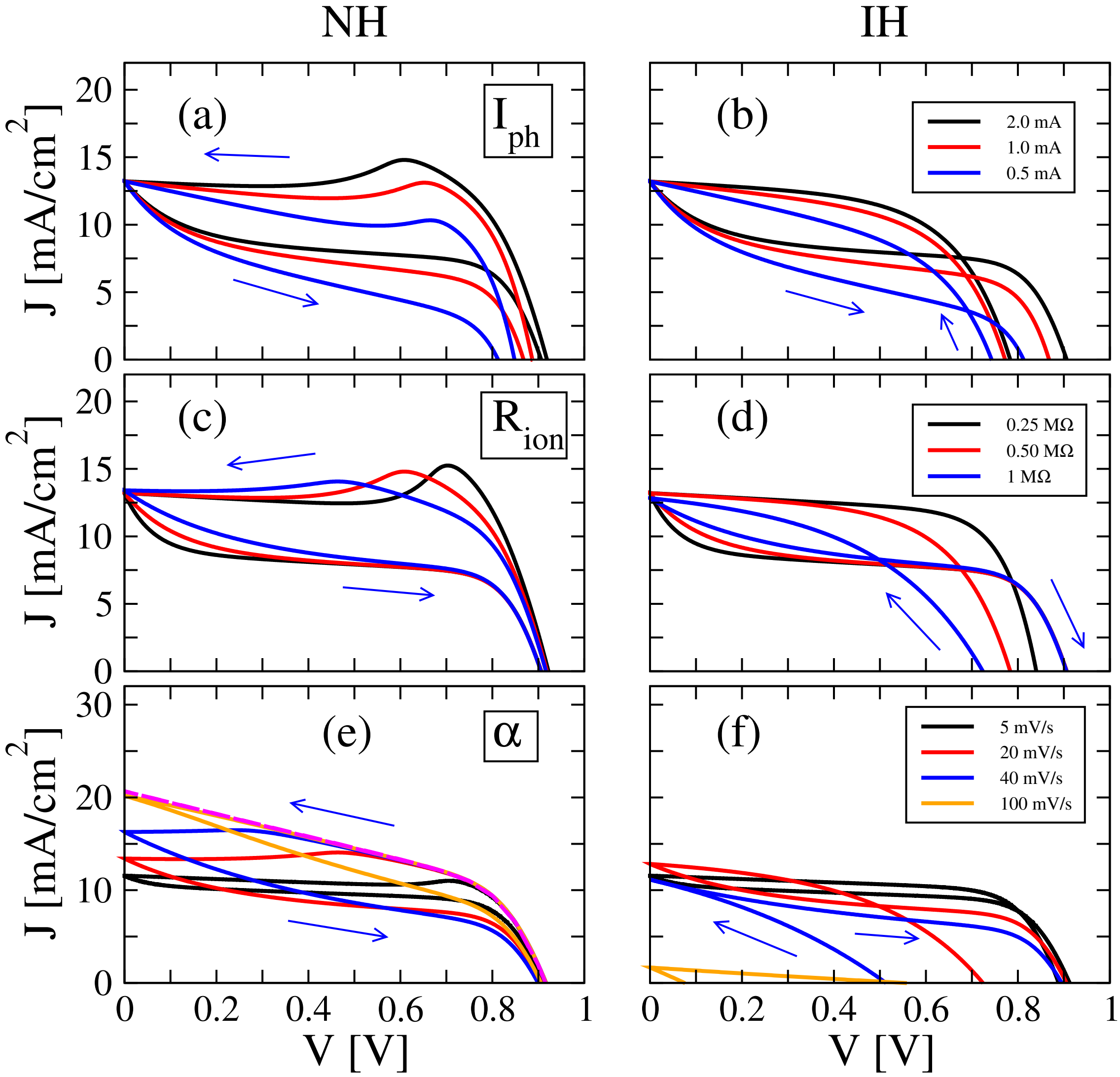

Figure 5.2: J-V analysis of the two dynamic hysteretic measurements for normal- and inverted hysteresis conditions when changing the: (a,b) illumination ($I_{\mathrm{ph}} = 0.5, 1, 2$ mA), where J has been rescaled for the lowest two illumination intensities by 4× and 2× ; (c,d) ionic resistance (R_{ion} = 0.25, 0.5, 1 MΩ); (e,f) scan rate (α = 5, 20, 40, 100 mV/s), for R_{ion} = 1 MΩ, where the limiting case of a very rapid scan (1V/s) is shown for NH (magenta). The color codes are the same for NH and IH. Reproduced with permission from Ref. [79]

The dynamic hysteretic effect is strongly linked to the illumination conditions. For different illumination conditions, a partial scaling with the J-V characteristics was revealed [117]. A similar behaviour was recorded by our model when changing the I_{ph} value from 2 mA to 1 mA and 0,5 mA (see Fig.5.2 (a) and (b)), where near the short circuit voltage value we witness a direct decrease of the collected curent with the photogenerated current I_{ph}. Being in good agreement with other studies [76], two other particularities can also be depicted from the scalar J-V dependence to the I_{ph}. The first observation regards the position of the current bump, which shifts towards lower voltage values when the photogenerated current is increasing. The second particularity involves the decreasing value of the short circuit voltage V_{oc} with the I_{ph} decrease.

The time step associated for a typical dynamical hysteretic effect ranges from seconds to a few hundred of seconds, the reason for this variation being the ionic migration. In our model, the ionic migration is controlled by the R_{ion}-C_{ion} circuit, where the slow process are given by $\tau = R_{\mathrm{ion}}C_{\mathrm{ion}}$. This way, there is a direct dependence between the C_{ion} and the voltage. When changing the R_{ion} values (0.25, 0.5, 1.0, MΩ) at a constant scan rate, there is a clear shift of the current bump under normal hysteresis conditions, while under inverted hysteresis conditions the current bump increases (see Fig.5.2 (c) and (d)).

Furthermore, the scan rate α has a strong effect on the J-V characteristics. When keeping the standard PSC parameters set and only changing the scan rate in the range of 5 mV/s to 1 V/s, this has a direct impact on the short circuit current and also on the hysteretic effect dimensions (see Fig.5.2 (e) and (f)). The effect is cancelled for very slow α rates, which are attributed to the point where the stationary case happens. The effect of cancellation was also seen at very fast α rates where the slow processes cannot follow the rapid voltage change.

The developed multiscale dynamic electrical model (m-DEM) can be used to reveal important information regarding the species types and the ion mobilities from the perovskite layer. At the same time, the model can account for the hysteresis effects observed in the current voltage measurements due to the different ETL ot HTL materials. In this concern, we have employed the Nelder-Mead (NM) [151] algorithm using the Python SciPy library to correlate the calculated J-V results from the m-DEM model with the experimental J-V measurements. By using the Nelder-Mead (NM) algorithm, we iteratively search the parameters values for which the model calculates a closely matched experimental J-V characteristic.

In the Ref. [152], the influence of the different ETL materials (TiO_2, SnO_2, SnO_2 QDs) on the PSC behaviour was analyzed. The resulting J-V experimental measurements show a relative large hysteresis and multiple values of the open circuit voltage. For these experimental results, we employed the search of some basic model parameters like: the series resistance (R_s), the shunt resistance (R_{sh}), the thermal voltage (V_{th}), the parametrization of the ionic capacitance (C_0, C_1) and of the recombination current (I_{rec0}, a, b).

Figure 5.3 presents the calculated J-V characteristics using the m-DEM model for the parameters provided by the (NM) algorithm in comparison with the experimental J-V measurements when considering different ETL materials. The coefficient of determination R^2 revealed at least 90% similarity between the calculated characteristics and the experimental ones.

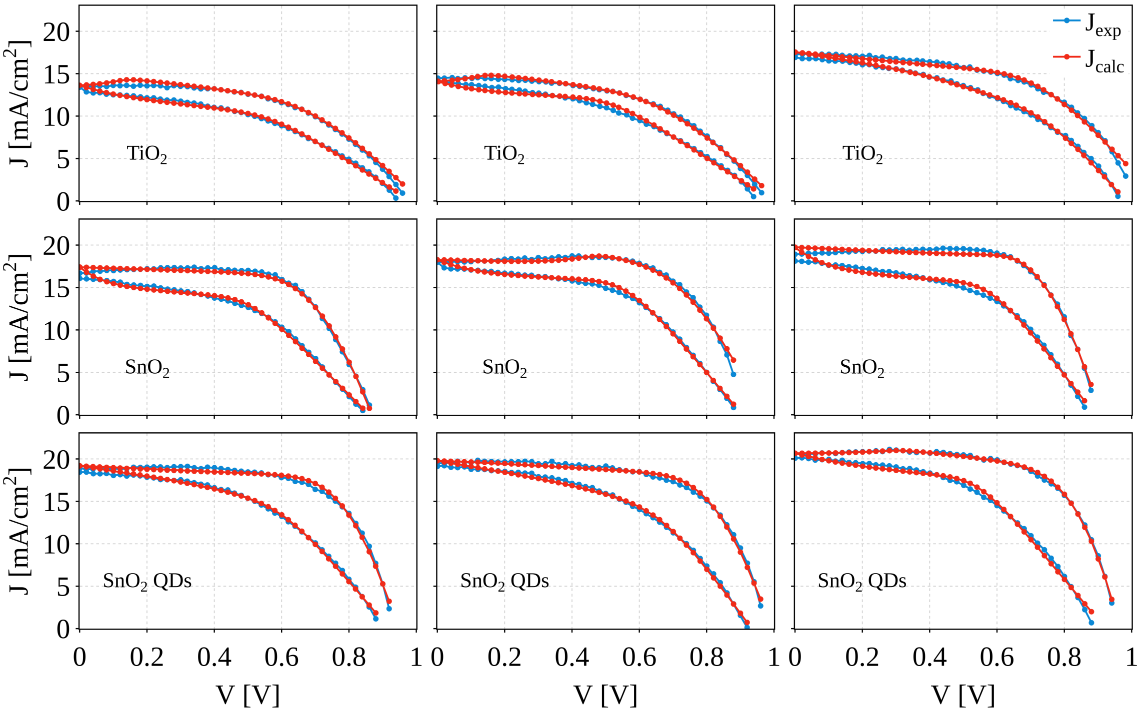

Figure 5.3: The J-V characteristics calculated with the m-DEM model (red dots) compared with the experimental J-V measurements (blue dots), for different ETL materials (TiO_2, SnO_2, SnO_2 QDs). Introduced with permission from Ref [152]

When comparing the key parameters of the m-DEM model, we show that they are in good agreement with the reported experimental values. For example, the series resistance follows the experimental decreasing trend, where (R_s) changes from 25 Ωcm^2 (TiO_2) to 17 Ωcm^2 (SnO_2) and 16 Ωcm^2 (SnO_2 QDs). The shunt resistances are in the same range of 200 Ωcm^2 to 600 Ωcm^2. The hysteretic effect was controlled with the help of the b parameter, which has the role to link the ionic current with the recombination current. On the other hand, we introduced a small V_{th}variation which parametrizes the diode recombination current by setting the open circuit voltage value.

The calculated J-V characteristics reveal the different voltage poling and illumination conditions effects on the hysteresis effect. The versatility of the m-DEM model in reproducing different hysteretic behaviours is evidenced in Fig. 5.3, which can be a useful tool for analyzing the influence of different ETL, HTL or PRV materials.

5.2 Small Signal Analysis

When conducting dynamic J-V measurements on a PSC, a hysteresis behaviour is observed between the reverse and forward voltage scans. This distinctive effect was primarily attributed to the apparent capacitive phenomena at the interfaces between the perovskite and the transporter layer materials. When performing EIS measurements under illumination, the results revealed even higher capacitance values, which were ascribed to a collection or recombination current that is modulated by the instantaneous electric field generated by ion migration within the perovskite.

Following the reports of these significant capacitive effects, inductive effects were also detected through EIS measurements. While the capacitive effects can be modelled using existing capacitive elements in the device structure, the reported inductive effects introduce a difficulty in assigning a physical inductor element. This highlighted the need to unify both concepts and provide a comprehensive description of the capacitive and inductive phenomena occurring within a PSC. Accordingly, the following sections are dedicated to discussing the small-signal analysis of the capacitive and inductive effects.

When performing EIS the Nyquist plot is a commonly used graphical representation to analyze the impedance of a system as a function of frequency. In this plot, the real part of the impedance is plotted versus the imaginary part. Unlike a typical frequency response plot, the Nyquist plot does not explicitly show frequency; instead, it presents the complex impedance at different frequencies as a series of data points that form arcs or semicircles.

For many electrochemical systems, including PSCs, the Nyquist plot can reveal crucial information about the underlying physical processes. The shape and position of the arcs in the plot can indicate different capacitive, resistive and inductive effects occurring within the device. For example, in PSCs, a low-frequency arc often represents the ionic capacitance, which is related to the slow movement of ions within the perovskite layer. Conversely, a high-frequency arc typically corresponds to the geometrical capacitance, which is associated with the dielectric properties of the material and the electrode interfaces.

5.2.1 Capacitive Effects

When using our m-DEM model, the best approach is to separately analyze the capacitive effects, that is why the inductive effects where canceled by setting $a = 0$ in Eq. (3.23). This way, in the performed EIS simulations, $b \times I_c$ controls the recombination current, which is essential for understanding the increasing apparent capacitance C_{app} with the illumination.

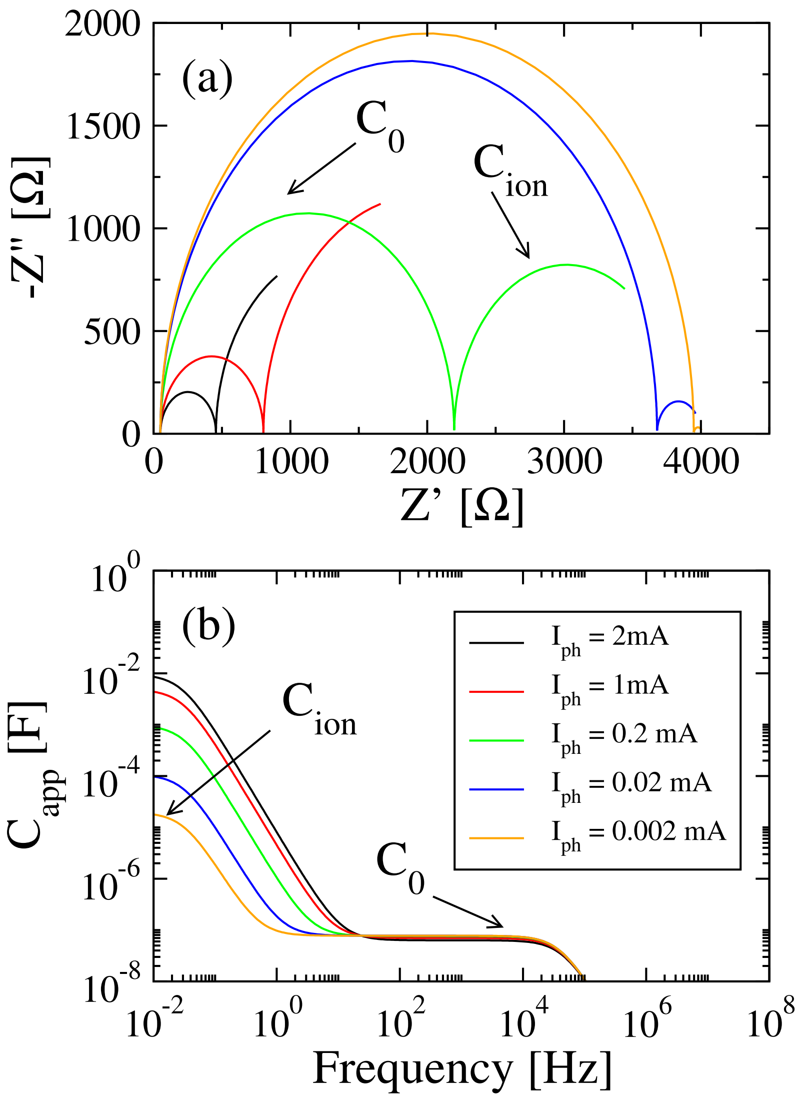

Figure 5.4: Different illumination conditions are simulated by changing the photogenerated current $I_{\text{ph}} = 2, 1, 0.2, 0.02, 0.002$ mA, the recorded capacitive effects are presented using: (a) Nyquist plot and (b) the apparent capacitance (C_{app}) as a function of frequency. When simulating the dark conditions ($I_{\text{ph}} = 0.002$ mA) the ionic capacitance (C_{ion}) is revealed at low frequencies, while at higher frequencies the geometrical capacitance (C_0) is evidenced. However, C_{app} increases sharply with illumination intensity, as in typical EIS experiments. Included with permission from Ref. [79].

In Figure 5.4 (a) is represented the Nyquist plot analysis and in subplot (b) the frequency dependence of C_{app}. In both representations we start from near-dark conditions ($I_{\mathrm{ph}} = 2 \times 10^{-3}$ mA) and extend to the maximum illumination intensity considered ($I_{\mathrm{ph}} = 2$ mA). The analysis is conducted at a working point of $V_{\mathrm{wp}} = 0.7$ V, which is close to the maximum power conversion efficiency (PCE) point, with the PSC in a steady-state regime.

When simulating the J-V under dark conditions, two plateaus can be observed: one corresponding to the ionic capacitance ($C_{\mathrm{ion}} \simeq 10$ μF) and the other to the geometrical capacitance ($C_0 \simeq 0.07$ μF). These findings are consistent with various EIS measurement reports under similar conditions, as well as with the experimental data presented in Ref. [79]. In the corresponding Nyquist plot, two distinct arcs are visible: one associated with the ionic capacitance at low frequencies and the other with the geometrical capacitance at high frequencies.

5.2.2 Inductive Effects

In some PSCs, the inductive effects are visible at intermediate frequencies, but typically the effect is recorded in a higher rate at small frequencies. In our dynamical model, we attributed the inductive behaviour to the ionic accumulation at the interfaces, which are produced by defect induced recombination of charge. The ionic accumulations associated with the inductive effects are represented in the m-DEM model through the $a \times Q_{\mathrm{C}}$ term in Eq. (3.23).

By following a procedure similar to the one described in the previous section, the capacitive effects introduced by charge recombination due to the electric field were mitigated by setting the parameter a. This adjustment serves to reduce the influence of the capacitive contribution to the overall system, which is often reflected in the imaginary part of the impedance, $\mathrm{Im}[Z]$.

The choice of $b = 100$ reproduces the typical behavior of a PSC, and captures the transition from capacitive effects to inductive ones. In many impedance measurements, especially in systems where recombination processes are significant, the imaginary component can exhibit complex behaviour, potentially leading to misleading interpretations if not properly accounted for. This approach, not only aids in better understanding the frequency-dependent behaviour of the system but also ensures that the sign of $\mathrm{Im}[Z]$, which is crucial for determining whether the system exhibits inductive or capacitive behaviour, is accurately captured.

In Fig. 5.5 we represented the Nyquist plot and $C_{\mathrm{app}} - f$ dependence for different $a = 0, 5, 10, 30, 40$ s^{-1}. As expected by setting the parameter $b = 100$, for small values of a, we still reproduce a capacitive behaviour, while for larger values the inductive effect becomes more visible at low frequencies and eventually the inductive effects will overpass the intrinsic capacitive behaviour.

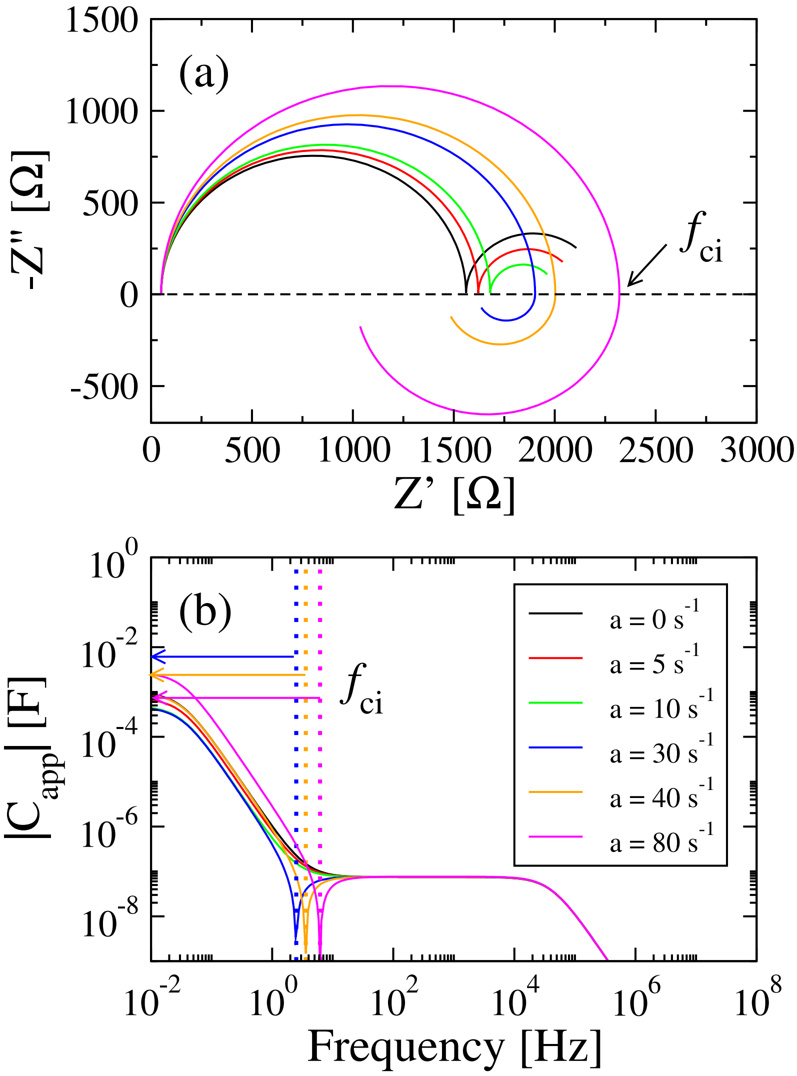

Figure 5.5: The transition between the capacitive and inductive behaviour, where the inductive effects are represented using the Nyquist plot (a) and they correspond to the frequencies ranges marked by arrows (b). For this representation, the parameter a is increased in the range of values: 0, 5, 10, 30, 40, 80 s^{-1}, which translates in a direct proportional effect with the recombination current, where for higher values the inductive effects are majoritary. Incorporated with permission from Ref. [79].

The EIS experiments performed under illumination reported significant apparent capacitances, while at a later time, the EIS measurements also reported relatively large inductances. The common point is that both phenomena originate from a modulated recombination current that increases markedly with illumination, as demonstrated by the experimental data presented in Ref. [79]. However, while the capacitive effects stem from the instantaneous electric field within the bulk of the perovskite, the inductive effects are primarily linked to ionic-induced defects, which are mostly concentrated at the interfaces. The mobility of ions and their tendency to induce defects are critical factors contributing to the inductive behaviour. Therefore, these inductive effects can serve as quantifiable indicators for defect analysis and recovery, offering the means to monitor PSC degradation.

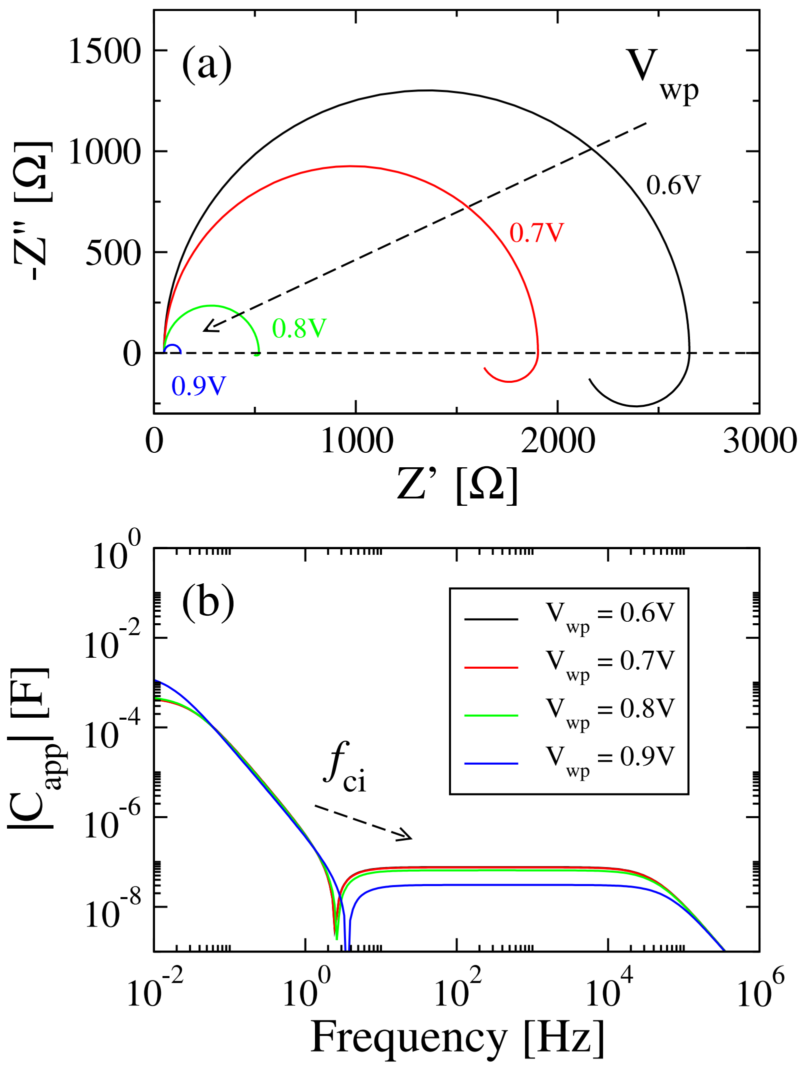

Figure 5.6: The inductive behaviour under the influence of the working point (V_{wp}) for different $a = 30\ \mathrm{s}^{-1}$: (a) Nyquist plot showing an enhancement in the sample conductivity; (b) The absolute value of the apparent capacitance, indicating an increase of the threshold frequency (f_{ci}) with V_{wp}, where the capacitive effect is switched into an inductive effect and, also, a small increase in the apparent inductive effect by increasing V_{wp} at low frequencies. Reprinted with permission from Ref. [79].

The inductive behaviour is also influenced by the working point V_{wp} pre-set in the EIS measurement, as illustrated in Fig. 5.6. Typically, the real part of the complex impedance decreases with increasing V_{wp}, indicating a transition towards more conductive behaviour. At higher V_{wp} and lower frequencies, the magnitude of the inductive effects increases due to larger ion accumulations. Additionally, the transition frequency between capacitive and inductive behaviour, denoted as f_{ci}, shifts towards higher frequencies. These observations are consistent with the experimental results presented in detail in the Ref. [79].

Moreover, the shift of f_{ci} with increasing V_{wp} highlights an intriguing conversion from capacitive to inductive behaviour, as recently reported in Ref. [77]. This conversion supports the hypothesis that significant ionic accumulations at positive voltages may trigger a type of recombination responsible for the observed inductive effects.

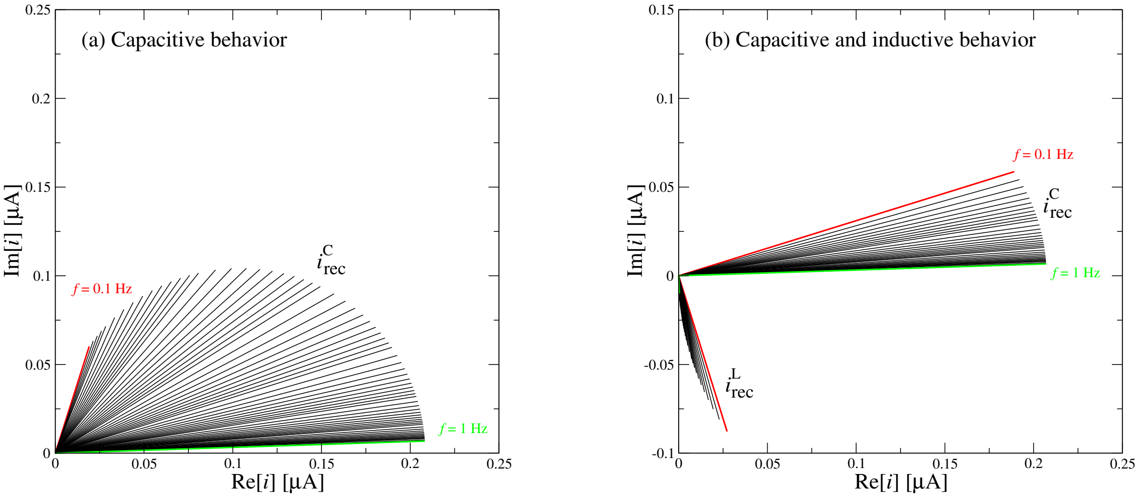

Figure 5.7: Phasor diagrams showing the dephasing of the recombination currents in the range of frequencies $f = 0.1 - 1$ Hz, for two types of PSCs, with: (a) capacitive effects only ($a = 0$, $b = 100$) and (b) capacitive and inductive effects ($a = 30\ \text{s}^{-1}$, $b = 100$). The diagrams correspond to the data sets shown in Fig. 5.5. The small signal voltage $v(t = 0)$ has zero phase, i.e. it is oriented along the x-axis ($i = 0$). In (b) subplot, the $\pi/2$ dephasing between $i_{\text{rec}}^{\text{C}}$ and $i_{\text{rec}}^{\text{L}}$ is evidenced. Incorporated with permission from Ref. [79].

The capacitive and inductive behaviours, as reflected by the two current components in Eq. (3.23), are suitably described by the phasor diagrams shown in Fig. 5.7. When a small signal with amplitude $v_0 = 1$ mV is applied, the resulting current i is dephased due to the different recombination mechanisms. The parallel impedances Z_{L}^{eq} and Z_{C}^{eq}, introduced in Eqs. (3.16) and (3.17), play a decisive role in this dephasing. The small signal recombination currents $i_{\text{rec}}^{\text{L}}$ and $i_{\text{rec}}^{\text{C}}$ are determined by the relations $v + iR_s = i_{\text{rec}}^{\text{L}} Z_{\text{L}}^{\text{eq}} = i_{\text{rec}}^{\text{C}} Z_{\text{C}}^{\text{eq}}$. These currents, $i_{\text{rec}}^{\text{L}}$ and $i_{\text{rec}}^{\text{C}}$, are dephased by $\pi/2$, as the former is proportional to Q_{c}, while the latter is proportional to $\partial Q_{\text{c}}/\partial t$. This phase relationship can be observed in Fig. 5.7(b). In the charge accumulation model, the impedance response is equivalent to large capacitive ($C_{\text{acc}} = 1.01$ mF) and inductive ($L = 16.6$ kH) elements, consistent with previous reports [64].

It is important to note the connection between the capacitive and inductive effects: the capacitive behaviour is influenced by the ionic current, $\partial Q_{\text{c}}/\partial t$, while the inductive behaviour is linked to ionic charge accumulation, Q_c. The total recombination current generally consists of a combination of these two components and the sample-specific parameters a and b determine which of the two behaviours dominates.

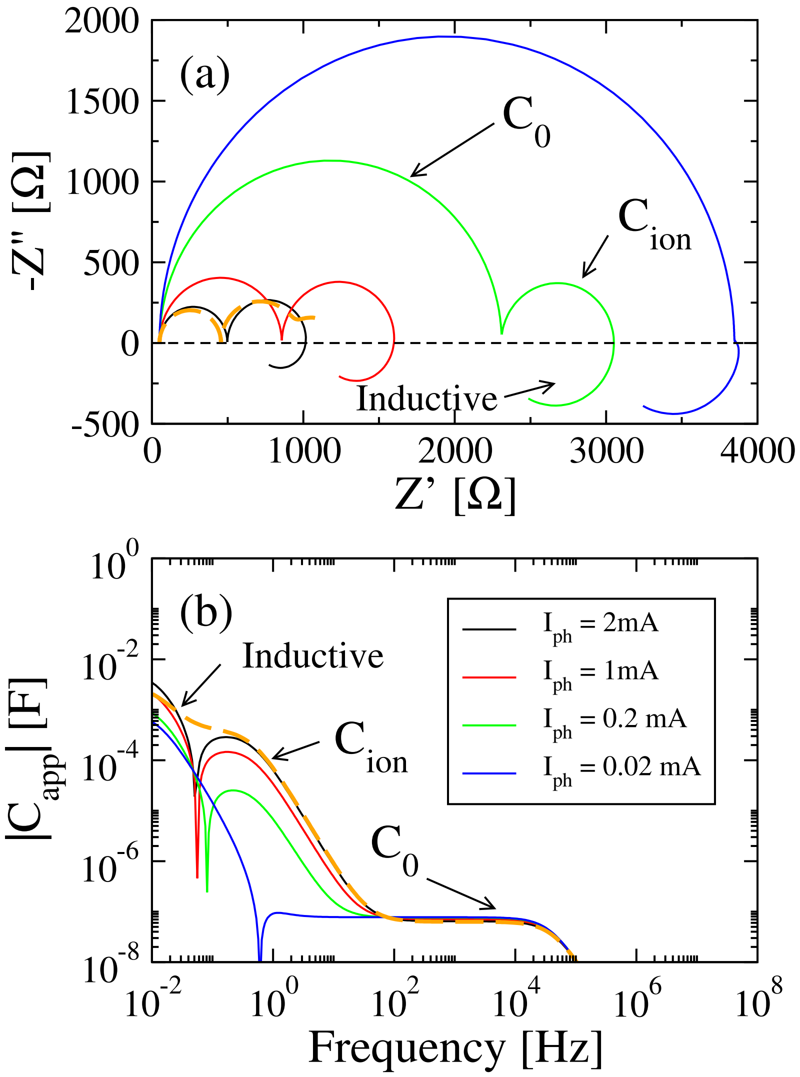

Figure 5.8: The inductive effects when using the two active interfaces model: (a) Nyquist plot and (b) $C_{\text{app}} - f$ plot. Where different illuminations conditions are used ($I_{\text{ph}} = 0.2, 1, 2$ mA). For the two interfaces, the capacitances have the ratio $C_1/C_2 = 20$. Consequently, the second semicircle, C_{ion}, corresponds to the C_2 capacitance, while the arc associated with C_1 shifts into the negative (inductive) region. The dashed lines represent the point where the inductive contribution vanishes for $I_{\text{ph}} = 2$ mA. Reproduced with permission from Ref [79].

When performing the EIS measurements, some PSCs reveal two or three arcs in the Nyquist plot [153], in addition to the low-frequency inductive behaviour. This observation indicates the presence of multiple relaxation time scales relevant to the capacitive behaviour. These distinct time scales may arise from the migration of various ionic species (e.g., iodine, methylammonium ions and their associated charged vacancies) and/or their accumulation at the interfaces. The capacitances associated with the two interfaces can differ significantly, considering the varying ionic diffusivities at the ETL-perovskite and HTM-perovskite interfaces and the resulting ion distributions.

Figure 5.8 illustrates a scenario with two ionic species (e.g., negatively charged iodine ions and positively charged iodine vacancies) migrating towards both interfaces, but with different time scales. The two capacitors are characterized by $\bar{C}_{01} = 20\ \mu\text{F}$, $\bar{C}_{11} = 2 \times 10^{-14}\ \mu\text{F}$, $\bar{C}_{02} = 1\ \mu\text{F}$, $\bar{C}_{12} = 10^{-15}\ \mu\text{F}$ and $n_c k_\text{B} T = 26$ meV, resulting in a capacitance ratio of $C_1/C_2 = 20$. In this case, Q_1 is the dominant component, generating the inductive effect at low frequencies, while Q_2 produces negligible inductive effects. The two capacitive arcs in the Nyquist plot correspond to C_0 and C_2.

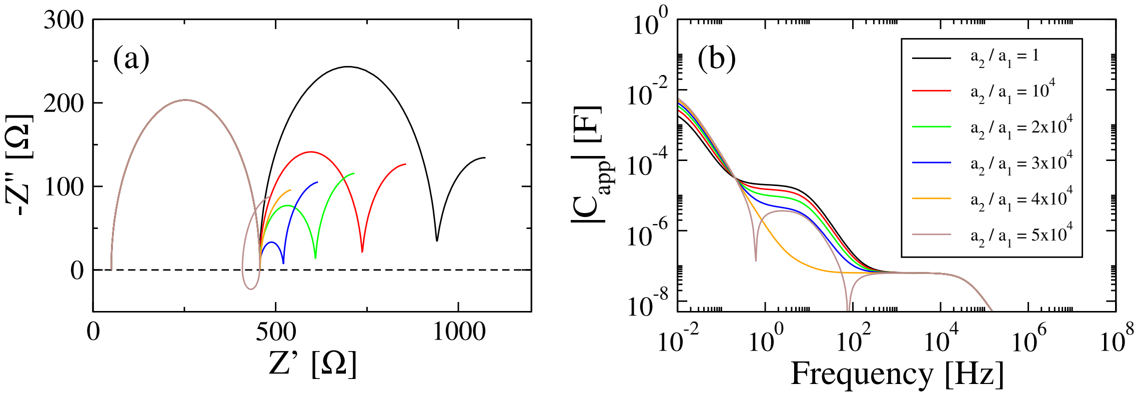

Figure 5.9: The two interface model showing the inductive loops at intermediate frequencies: (a) Nyquist and (b) C-f plots. Here, the two capacitors are parametrized by $\bar{C}_{01} = 20\ \mu\text{F}$, $\bar{C}_{11} = 20 \times 10^{-15}\ \mu\text{F}$, $\bar{C}_{02} = 0.05\ \mu\text{F}$, $\bar{C}_{12} = 0.05 \times 10^{-15}\ \mu\text{F}$, $n_c k_\text{B} T = 26$ meV, i.e. we have $C_1/C_2 = 400$. We consider in this case $a_1 = 1$ and a_2/a_1 in the sequence specified in the legend. A smaller C_2 capacitance drives the inductive effects at higher (intermediate) frequencies, producing the inductive loop. As Q_2 is correspondingly smaller, the ion-induced recombination effects become visible as a_2 is increased. Incorporated with permission from Ref. [79].

When the $a_2 \gg a_1$; the second interface shows a higher influence on the recombination current, this translates in the formation of intermediate-frequency current loops, as depicted in Fig. 5.9. The C-f plots in Fig. 5.9 (b), show that at higher values of the a_2/a_1 report the inductive behaviour is present even at intermediate frequencies. At the same time, the Nyquist plot sustain this picture where the ion induced recombination effects are visible at higher frequencies.

In the two-interface model depicted in Fig. 3.3, the electrical behaviour of the perovskite solar cell (PSC) is represented by two parallel resistor-capacitor (R-C) circuits. These two R-C circuits symbolize the two active interfaces within the PSC, typically corresponding to the interfaces between the perovskite layer and the electron/hole transport layers. The model helps to simulate and analyze the dynamic processes occurring at these interfaces, particularly the recombination of charge carriers electrons and holes that can significantly impact the efficiency of the solar cell.

In this context, the resistances $R_{1,2}$ in the model play a crucial role. These resistances represent the charge transfer resistance at each interface, which influences the rate of electron/hole -ion charge neutralization. Higher values of $R_{1,2}$ suggest a higher resistance to charge transfer, leading to reduced recombination rates. Conversely, smaller $R_{1,2}$ values imply lower resistance, which facilitates faster neutralization of photogenerated carriers and ions.

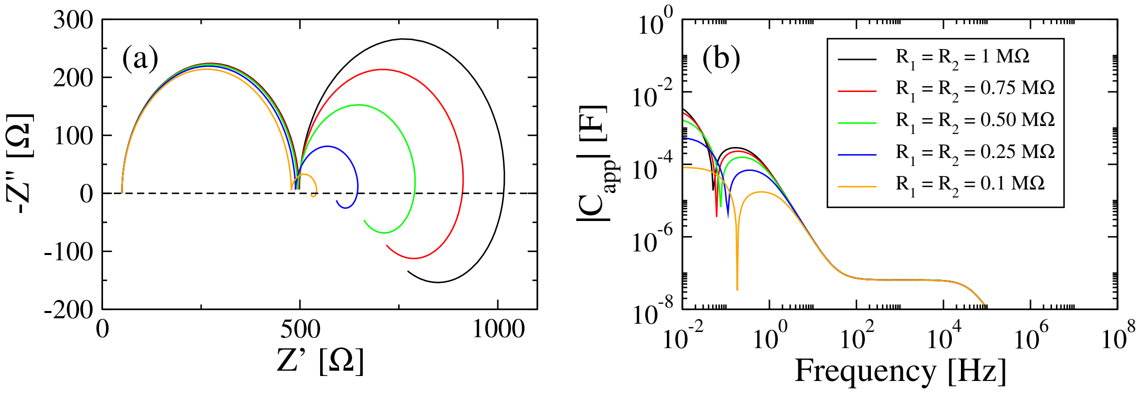

Figure 5.10: The influence of the ionic capacitors' loss resistances, R_1 and R_2: (a) Nyquist plots and (b) C-f dependence. Included with permission from Ref. [79].

As the values of $R_{1,2}$ decrease (which might happen if the interfaces become more conductive or the recombination rate increases), the inductive effects diminish. This reduction in the inductive behaviours at low frequencies can be interpreted as enhanced recombination, where charge carriers recombine more rapidly, reducing the overall charge build-up that would otherwise contribute to capacitive or inductive effects.

The trend becomes particularly noticeable when $R_{1,2}$ is less than a threshold value $R_a = 0.5$ MΩ. Below this threshold, the resistance is sufficiently low that the recombination processes dominate, making the inductive effects almost negligible. This observation suggests that the PSCs performance is highly sensitive to the resistance at the interfaces and controlling $R_{1,2}$ is crucial for optimizing the device's efficiency by minimizing unwanted recombination.

Device Modeling Using SCAPS

Starting from the DFT investigations performed in Chapter 4.2, where we have analyzed the band alignment dependence on the vacancy defect in the ETL, HTL and PRV, we calibrated four interface defect layers (IDLs), which will be used in SCAPS program to simulate the PSC performance. For each interface, we have two IDLs, this way at the ETL-PRV (I_1) interface, namely IDL1 and IDL2 which correspond to TiO_2 and MAPI (see Fig. 6.1). For the second interface (I_2), composed of PRV and HTL, we used the IDL3 and IDL4 to represent MAPI and Cu_2O materials.

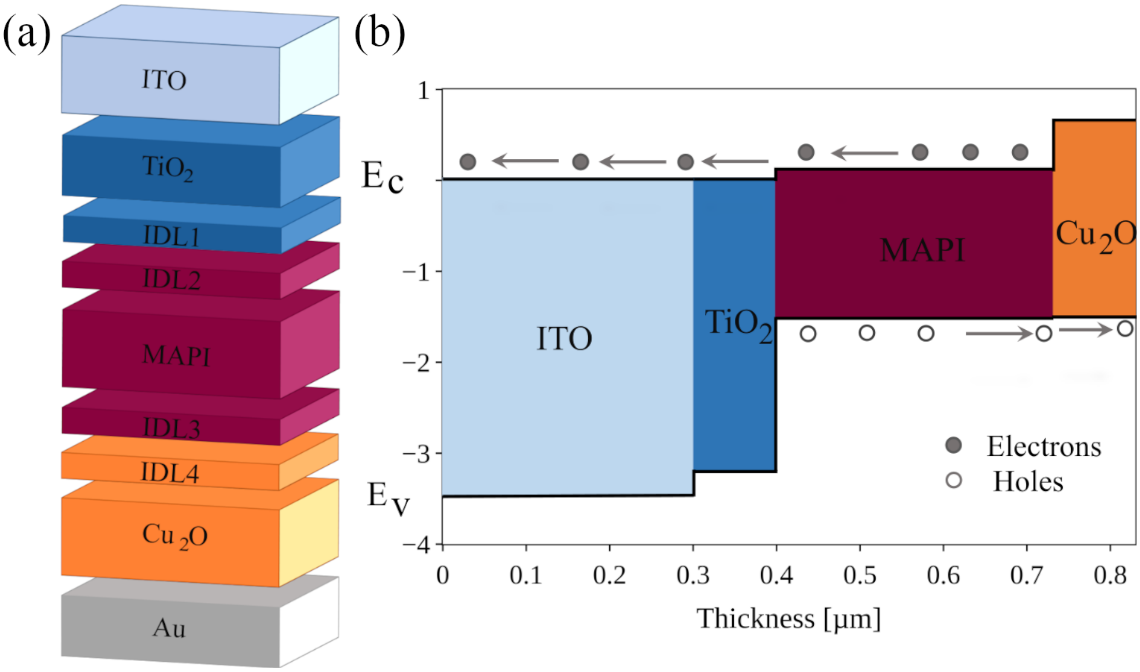

Figure 6.1: The reference PSC used for SCAPS calculations. Where (a) reproduces the PSC layered model and (b) is a schematic representation of the PSC band diagram. The four IDL layers are introduced to account for the vacancy defect calculations performed within DFT. Incorporated with permission from Ref. [144].

The influence of various defect types on the performance of perovskite solar cells (PSCs) is assessed through stationary current-voltage (J-V) characteristics, which

Table 6.1: SCAPS parameters used for the reference PSC [154]. The IDLs are part of the corresponding oxide or MAPI layers. Republished with permission from Ref. [144].

Parameters	ITO	TiO_2	IDL1	IDL2	MAPI	IDL3	IDL4	Cu_2O
Thickness [nm]	300	100	10	10	330	10	10	100
E_g [eV]	3.5	3.2	3.2	1.55	1.55	1.55	2.1	2.1
χ [eV]	4.0	4.0	4.0	3.9	3.9	3.9	3.2	3.2
ε_r	9	10	10	10	10	10	7.11	7.11
N_c [cm^{-3}]	2.2×10^{18}	2.0×10^{18}	2.0×10^{18}	2.75×10^{18}	2.75×10^{18}	2.75×10^{18}	2.2×10^{18}	2.2×10^{18}
N_v [cm^{-3}]	1.8×10^{19}	1.8×10^{19}	1.8×10^{19}	3.9×10^{18}	3.9×10^{18}	3.9×10^{18}	1.9×10^{19}	1.9×10^{19}
μ_n [cm^{2}V^{-1}s^{-1}]	20	20	20	10	10	10	200	200
μ_p [cm^{2}V^{-1}s^{-1}]	10	10	10	10	10	10	8600	8600
N_D [cm^{-3}]	1.0×10^{18}	1.0×10^{18}	1.0×10^{18}	1.0×10^{18}	1.0×10^{18}	1.0×10^{18}	-	-
N_A [cm^{-3}]	-	-	-	1.0×10^{18}	1.0×10^{18}	1.0×10^{18}	1.0×10^{18}	1.0×10^{18}
N_t [cm^{-3}]	-	-	-	1.0×10^{16}	1.0×10^{16}	1.0×10^{16}	-	-

are modeled using the SCAPS simulation software. SCAPS calculates energy band structures, carrier concentrations and current densities for devices that can consist of up to seven semiconductor layers. This is achieved by solving one-dimensional semiconductor equations, along with the relevant boundary conditions at the device contacts, as detailed in [122].

Each semiconductor layer in the model is defined by a set of physical parameters, including the band gap energy (E_g), electron affinity (χ), relative dielectric permittivity (ε_r), effective density of states in the conduction and valence bands (N_C and N_V, respectively), thermal velocities of electrons and holes ($v_\mathrm{th,n}$ and $v_\mathrm{th,p}$), mobilities of electrons and holes (μ_n and μ_p), donor and acceptor doping concentrations (N_D and N_A) and the overall defect density (N_t). These parameters, which are crucial in defining the behaviour and performance of each layer, are summarized in Table 6.1.

6.1 SCAPS Simulations

Using the model configuration from Fig. 6.1, the electron transport layer (ETL) and hole transport layer (HTL) are modeled with slight n-type and p-type doping, respectively, while the perovskite layer is considered to be intrinsic, meaning it has no intentional doping. The simulations are conducted under standard illumination conditions, specifically AM 1.5G, to mimic realistic sunlight exposure. In order to simulate the PSC with SCAPS, we specified typical parameters for every material layer, the used parameters are presented in Table 6.1 and they account for the ideal PSC. For the additional IDLs, the defect concentration was varied between zero and 5×10^{18} cm^{-3}, with either n- or p-type character for one interface at a time.

The reference solar cell exhibits a nearly flat band condition for electrons at interface I_1 and for holes at interface I_2, indicating minimal resistance to the collection of photogenerated carriers. From the simulated J-V characteristics, the following performance metrics are obtained: PCE = 19.25%, FF = 82%, $V_{oc} = 1.04$ V, $I_{sc} = 22.5$ mA for a solar cell with an area of 1 cm^2.

Vacancy-induced doping can significantly alter the performance of PSCs, with various combinations of defects being possible. However, for the structure under investigation, our analysis shows that only specific types of vacancies have a notable impact. Based on DFT analysis of the band alignment, it is expected that IDLs will induce local variations in the band edges near the interfaces. We consider vacancy defects with concentrations up to 5×10^{18} cm^{-3}, either of donor or acceptor type. The resulting band diagrams are presented in Fig. 6.2. At the I_1 interface, oxygen vacancies (V_O) and iodine vacancies (V_I) create small dips in the band structure, while titanium vacancies (V_Ti) and lead vacancies (V_Pb) produce small peaks. Given the slight conduction band offset, V_Ti and V_Pb in IDL1 and IDL2, respectively, will predominantly affect electron collection.

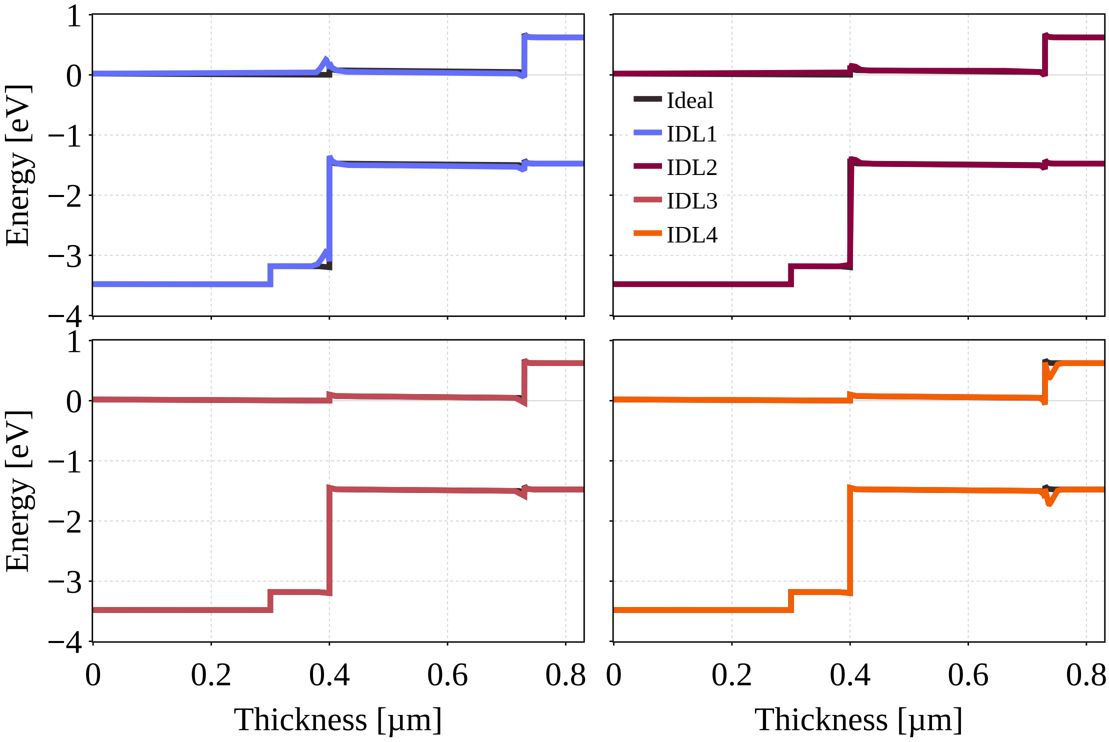

Figure 6.2: Band diagrams obtained by SCAPS simulations: IDL1 and IDL2 have p-type vacancies (V_Ti and V_Pb), while IDL3 and IDL4 have n-type vacancies (V_I and V_O). The vacancy defect concentration is 5×10^{18} cm^{-3}. Adapted with permission from Ref. [144].

The holes are blocked at this interface and the large band offset is less influenced by these defects. Conversely, the small dips caused by V_O and V_I have a much lesser effect on electron collection. This behaviour is mirrored at the I_2 interface, where holes are the collected carriers. Here, they are primarily affected by the *n*-type character of the IDLs, which corresponds to V_I and V_O in IDL3 and IDL4, respectively.

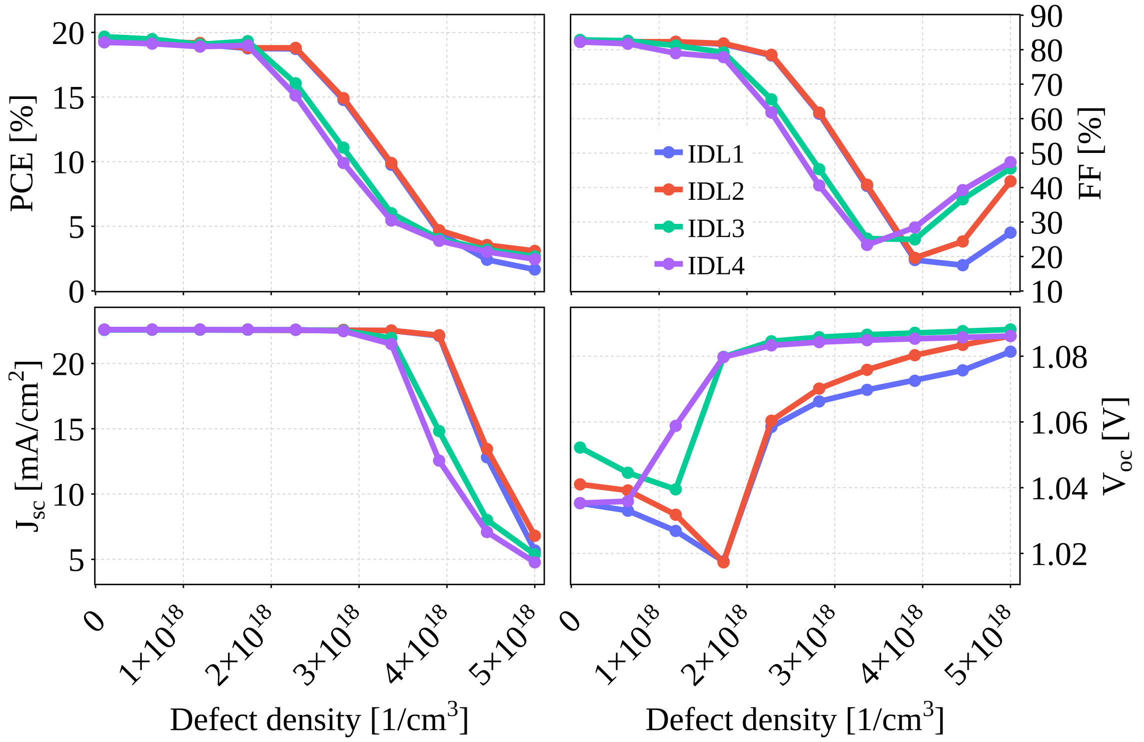

Figure 6.3: Performance of the PSCs with p-type IDL1/IDL2 and n-type IDL3/IDL4, as evidenced by PCE, FF, I_sc and V_oc. Incorporated with permission from Ref. [144].

The dependence of PSC performance on defect concentration is illustrated in Fig. 6.3, where several indicators such as: PCE, FF, I_sc and V_oc are monitored. As defect concentration increases, the performance of the solar cell declines, with the PCE dropping to less than 5%. The I_2 interface is found to be more sensitive to defects than the I_1 interface. A similar trend is observed for I_sc and FF, though FF shows an increase at higher defect concentrations, likely due to the reduction in I_sc. The open circuit voltage, V_oc, exhibits a slight non-monotonic increase, stabilizing around 1.07-1.09 V.

Naturally, the sensitivity to defect concentration can be modified by increasing the conduction band (CB) and valence band (VB) offsets at interfaces I_1 and I_2, respectively. In such cases, the impact of oxide-related defects on the J-V characteristics would be reduced.

Conclusions

In this study, we have performed a comprehensive investigation of the optoelectronic properties, stability, and performance of quasi-2D perovskites and PSCs through a combination of *ab initio* calculations, device simulation and circuit modeling. Our findings on quasi-2D perovskites reveal that the electronic structure and stability are significantly influenced by the choice of halogens and large alkylammonium cations. At the same time, we reported that the band gap increases with the size of the large cation and with a decrease in the halogen atomic number, highlighting the delicate balance between achieving optimal band gaps and ensuring material stability. Although the inherent quantum confinement in 2D perovskites leads to larger-than-ideal band gaps, bromine and chlorine-based perovskites exhibit enhanced stability against both intrinsic and extrinsic degradation mechanisms. Notably, further research into optimal mixtures of halogens and cations could offer a pathway to improved efficiency and stability.

Our equivalent circuit model for PSCs successfully reproduces the complex capacitive and inductive effects observed experimentally, such as: current bumps, hysteresis behaviors and variations in hysteretic effects under different conditions. The model bridges the gap between charge accumulation (CA) and charge collection (CC) approaches, showing that both can yield equivalent outcomes under certain conditions, though they differ fundamentally in the capacitance and resistance values they require. The CA model suggests an unrealistic large capacitance, while the CC model attributes the same time scale to smaller capacitance but larger resistance, correlating these to ionic currents and recombination processes modulated by the device's electric field.

The voltage dependence of capacitance was compared with the experimetal results, which is crucial for accurately describing J-V hysteresis. Our findings also underscore the relationship between capacitive and inductive effects, both of which are linked to the recombination of photogenerated carriers. The observed variation in inductive effects under illumination suggests that these effects are driven by recombination mechanisms associated with ionic accumulations, complementing the capacitive effects driven by local electric fields.

Moreover, our study on PSCs with Cu_2O as the inorganic HTL, coupled with DFT calculations and SCAPS simulations, highlighted the critical role of vacancy defects in determining the overall device performance. The alignment of band structures and the impact of vacancies in TiO_2, Cu_2O and MAPI layers were elucidated, emphasizing the need for passivating specific vacancies, particularly titanium vacancies in TiO_2 and oxygen vacancies in Cu_2O, to mitigate unintentional doping and performance degradation. SCAPS simulations further reinforced these findings by correlating power conversion efficiency with defect concentration and localization, offering strategies for optimizing device performance.

In conclusion, this study provides a robust framework for understanding and optimizing the optoelectronic properties, stability and performance of perovskite-based solar cells. The insights gained here serve as a foundation for future research aimed at improving material stability, mitigating defect-induced performance loss and enhancing the overall efficiency of these promising solar technologies.

Scientific Research

8.1 Publications

1. Nicolae Filipoiu and George Alexandru Nemnes, ”Prediction of equilibrium phase, stability and stress-strain properties in Co-Cr-Fe-Ni-Al high entropy alloys using artificial neural networks”. *Metals*, 10(12) (2020), 1569.
2. Claudiu Locovei, Nicolae Filipoiu, Andrei Kuncser, Anda-Elena Stanciu, Ştefan Antohe, Camelia-Florina Florica, Andreea Costas, Ionuţ Enculescu, Luc Piraux,Victor Kuncser and Vlad-Andrei Antohe, ”Unidirectional Magnetic Anisotropy in Dense Vertically-Standing Arrays of Passivated Nickel Nanotubes”. *Nanomaterials*, 10(12) (2021), 2444.
3. George Alexandru Nemnes, Nicolae Filipoiu and Valentin Sipica, ”Feature selection procedures for combined density functional theory—artificial neural network schemes”. *Physica Scripta*, 96(6) (2021), 065807.
4. Nicolae Filipoiu, Tudor Luca Mitran, Dragos Victor Anghel, Mihaela Florea, Ioana Pintilie, Andrei Manolescu, and George Alexandru Nemnes. “Investigation of opto-electronic properties and stability of mixed-cation mixed-halide perovskite materials with machine-learning implementation”. *Energies* 14.17 (2021), 5431.
5. Nicolae Filipoiu, Amanda Teodora Preda, Dragos-Victor Anghel, Roxana Patru, Rachel Elizabeth Brophy, Movaffaq Kateb, Cristina Besleaga, Andrei Gabriel Tomulescu, Ioana Pintilie, Andrei Manolescu, et al. “Capacitive and inductive effects in perovskite solar cells: The different roles of ionic current and ionic charge accumulation”. *Physical Review Applied* 18.6 (2022), 064087.
6. Calin-Andrei Pantis-Simut, Amanda Teodora Preda, Nicolae Filipoiu, Alaa Allosh, and George Alexandru Nemnes. “Electric-field control in phosphorene based heterostructures”. *Nanomaterials* 12.20 (2022), 3650.

7. Nicolae Filipoiu, Anca G Mirea, Sarah Derbali, Calin-Andrei Pantis-Simut, Dragos-Victor Anghel, Andrei Manolescu, Ioana Pintilie, Mihaela Florea, and George Alexandru Nemnes. “Optoelectronic and stability properties of quasi-2D alkylammonium based perovskites”. *Physical Chemistry Chemical Physics* 25.4 (2023), 332-3331.

8. Mihaela Cosinschi, Amanda Teodora Preda, Calin Pantis-Simut, Nicolae Filipoiu, Ioan Ghitiu, Mihnea Alexandru Dulea, Lucian Ion, Andrei Manolescu, and George Alexandru Nemnes. “Collective dynamics of Ca atoms encapsulated in C60 endohedral fullerenes”. *Physical Chemistry Chemical Physics* (2024).

9. Alaa Allosh, Calin-Andrei Pantis-Simut, Nicolae Filipoiu, Amanda Teodora Preda, George Necula, Ioan Ghitiu, Dragos-Victor Anghel, Mihnea Alexandru Dulea, and George Alexandru Nemnes. “Tuning phosphorene and MoS2 2D materials for detecting volatile organic compounds associated with respiratory diseases”. *RSC Advances* 14.3 (2024), 1803-1812.

10. Anca G. Mirea, Ioana D. Vlaicu, Sarah Derbali, Florentina Neatu, Andrei G.Tomulescu, Cristina Besleaga, Monica Enculescu, Andrei C. Kuncser, Alexandra C. Iacoban, Nicolae Filipoiu, Marina Cuzminschi, George A. Nemnes, Andrei Manolescu, Mihaela Florea, and Ioana Pintilie. Electron transporting bilayers for perovskite solar cells: spray coating deposition of c-TiO_2/m-SnO_2 quantum dots. 2024. arXiv: 2406.18261.

8.2 Conferences

1. Nicolae Filipoiu, Marina Cuzminschi, Tudor Luca Mitran, Dragos Victor Anghel, George E. Stan, Cristina Besleaga, Ioana Pintilie, Kristinn Torfason, Andrei Manolescu and George Alexandru Nemnes, ”Optimizing the band alignment in Methylammonium lead iodide - $Cu_xNi_{1-x}O$ interface”, *International Balkan Workshop on Applied Physics*, Oral presentation(2022).

2. Nicolae Filipoiu,Calin-Andrei Pantis-Simut, Marina Cuzminschi, Dragos Victor Anghel, George E. Stan, Cristina Besleaga, Ioana Pintilie, Kristinn Torfason, Andrei Manolescu and George Alexandru Nemnes, ”Investigation of the band alignment in mixed halide perovskite- Cu_2O Interfaces”, *International Balkan Workshop on Applied Physics*, Poster presentation(2023).

3. Calin-Andrei Pantis Simut, Alaa Allosh, Amanda Teodora Preda, Mihaela Cosinschi, Nicolae Filipoiu, and George Alexandru Nemnes. “Enhancing Biomarker

Detection Using Artificial Neural Networks". *2023 International Conference on Advanced Scientific Computing (ICASC)*. IEEE. 2023, pp. 1-5.

4. Rachel Elizabeth Brophy, Movaffaq Kateb, Ioan Ghitiu, Nicolae Filipoiu, Kristinn Torfason, H.G. Svavarsson, George Alexandru Nemnes, Ioana Pintilie and Andrei Manolescu, 2023, October. "OH^- ions can reduce the iodide migration in MAPI". In *2023 International Semiconductor Conference (CAS)* (pp. 139-142). IEEE.

8.3 Books

1. Tudor Luca Mitran, Rachel Elizabeth Brophy, Marina Cuzminschi, Nicolae Filipoiu, Movaffaq Kateb, Ioana Pintilie, Andrei Manolescu, and George Alexandru Nemnes. "Ab initio studies on perovskites". *Low-Dimensional Halide Perovskites*. Elsevier, 2023, pp. 153-185.

8.4 Work in progress

1. Nicolae Filipoiu, Neculai Plugaru, Titus Sandu, Rodica Plugaru, and George Alexandru Nemnes. "First principles electron transport in magnetoelectric $SrRuO_3/BaTiO_3/SrTiO_3/SrRuO_3$ interfaces", preprint (2024).

2. Nicolae Filipoiu, Marina Cuzminschi, Calin-Andrei Pantis-Simut, Kristinn Torfason, Rachel Elizabeth Brophy, Andrei Manolescu, Roxana E Patru, Cristina Besleaga, George E Stan, Ioana Pintilie, et al. "Impact of interface defects on the band alignment and performance of TiO_2/MAPI/Cu_2O perovskite solar cells". *arXiv preprint* arXiv:2406.19594 (2024).

Bibliography

[1] Hannah Ritchie and Pablo Rosado. “Electricity Mix”. *Our World in Data* (2020). https://ourworldindata.org/electricity-mix.

[2] Flavio Odoi-Yorke and Atchou Woenagnon. “Techno-economic assessment of solar PV/fuel cell hybrid power system for telecom base stations in Ghana”. *Cogent Engineering* 8.1 (2021), 1911285.

[3] Pablo Rosado and Hannah Ritchie. “Energy Mix”. *Our World in Data* (2020). https://ourworldindata.org/energy-mix.

[4] Jose Jonathan Rubio Arias, Jinsang Kim, Bianca Pedroso Silva Santos, Lais Schmidt Albuquerque, Isabela Custodio Mota, and Maria de Fatima Vieira Marques. “Solution processing of polymer solar cells: towards continuous vacuum-free production”. *Journal of Materials Science: Materials in Electronics* 32 (2021), 11367–11392.

[5] Fatemeh Rahmani, Mark Alan Robinson, and MR Barzegaran. “Cool roof coating impact on roof-mounted photovoltaic solar modules at texas green power microgrid”. *International Journal of Electrical Power & Energy Systems* 130 (2021), 106932.

[6] Shuhui Li, Timothy A Haskew, Dawen Li, and Fei Hu. “Integrating photovoltaic and power converter characteristics for energy extraction study of solar PV systems”. *Renewable Energy* 36.12 (2011), 3238–3245.

[7] Hector Cotal, Chris Fetzer, Joseph Boisvert, Geoffrey Kinsey, Richard King, Peter Hebert, Hojun Yoon, and Nasser Karam. “III–V multijunction solar cells for concentrating photovoltaics”. *Energy & Environmental Science* 2.2 (2009), 174–192.

[8] Masafumi Yamaguchi, Tatsuya Takamoto, Kenji Araki, and Nicholas Ekins-Daukes. “Multi-junction III–V solar cells: current status and future potential”. *Solar Energy* 79.1 (2005), 78–85.

[9] Brendan M Kayes, Hui Nie, Rose Twist, Sylvia G Spruytte, Frank Reinhardt, Isik C Kizilyalli, and Gregg S Higashi. “27.6% conversion efficiency, a new record for single-junction solar cells under 1 sun illumination”. *2011 37th IEEE photovoltaic specialists conference*. IEEE. 2011, pp. 000004–000008.

[10] Corsin Battaglia, Andres Cuevas, and Stefaan De Wolf. “High-efficiency crystalline silicon solar cells: status and perspectives”. *Energy & Environmental Science* 9.5 (2016), 1552–1576.

[11] Taesoo D Lee and Abasifreke U Ebong. “A review of thin film solar cell technologies and challenges”. *Renewable and Sustainable Energy Reviews* 70 (2017), 1286–1297.

[12] Arvind Shah, P Torres, Reto Tscharner, N Wyrsch, and H Keppner. “Photovoltaic technology: the case for thin-film solar cells”. *science* 285.5428 (1999), 692–698.

[13] Zach M Beiley and Michael D McGehee. “Modeling low cost hybrid tandem photovoltaics with the potential for efficiencies exceeding 20%”. *Energy & Environmental Science* 5.11 (2012), 9173–9179.

[14] Martin A Green, Anita Ho-Baillie, and Henry J Snaith. “The emergence of perovskite solar cells”. *Nature photonics* 8.7 (2014), 506–514.

[15] Nam-Gyu Park. “Perovskite solar cells: an emerging photovoltaic technology”. *Materials today* 18.2 (2015), 65–72.

[16] Jin Young Kim, Jin-Wook Lee, Hyun Suk Jung, Hyunjung Shin, and Nam-Gyu Park. “High-efficiency perovskite solar cells”. *Chemical reviews* 120.15 (2020), 7867–7918.

[17] Robert M Hazen. “Perovskites”. *Scientific American* 258.6 (1988), 74–81.

[18] Wen-Bo Li, Di Zhou, Ran Xu, Da-Wei Wang, Jin-Zhan Su, Li-Xia Pang, Wen-Feng Liu, and Guo-Hua Chen. “BaTiO3-based multilayers with outstanding energy storage performance for high temperature capacitor applications”. *ACS Applied Energy Materials* 2.8 (2019), 5499–5506.

[19] Bartlomiej Szafraniak, Lukasz Fusnik, Jie Xu, Feng Gao, Andrzej Brudnik, and Artur Rydosz. “Semiconducting metal oxides: $SrTiO_3$, $BaTiO_3$ and $BaSrTiO_3$ in gas-sensing applications: A review”. *Coatings* 11.2 (2021), 185.

[20] Manjusha Passi and Bonamali Pal. “A review on CaTiO3 photocatalyst: Activity enhancement methods and photocatalytic applications”. *Powder Technology* 388 (2021), 274–304.

[21] Bostjan Jancar, Danilo Suvorov, Matjaz Valant, and Goran Drazic. "Characterization of $CaTiO_3$-$NdAlO_3$ dielectric cerntesamics". *Journal of the European Ceramic Society* 23.9 (2003), 1391–1400.

[22] Vu Thanh Tra, Jhih-Wei Chen, Po-Cheng Huang, Bo-Chao Huang, Ye Cao, Chao-Hui Yeh, Heng-Jui Liu, Eugene A Eliseev, Anna N Morozovska, Jiunn-Yuan Lin, et al. "Ferroelectric control of the conduction at the $LaAlO_3/SrTiO_3$ heterointerface". *Advanced Materials* 25.24 (2013), 3357–3364.

[23] Neculai Plugaru, Titus Sandu, Rodica Plugaru, Nicolae Filipoiu, and George Alexandru Nemnes. "First principles electron transport in magnetoelectric $SrRuO_3/BaTiO_3/SrTiO_3/SrRuO_3$ interfaces". *preprint* (2024).

[24] Akihiro Kojima, Kenjiro Teshima, Yasuo Shirai, and Tsutomu Miyasaka. "Organometal halide perovskites as visible-light sensitizers for photovoltaic cells". *Journal of the american chemical society* 131.17 (2009), 6050–6051.

[25] Aldo Di Carlo, N Yaghoobi Nia, A Agresti, S Pescetelli, F Matteocci, L Vesce, and LA Castriotta. "On the scaling of perovskite photovoltaics to modules and panels". *2021 IEEE 48th Photovoltaic Specialists Conference (PVSC)*. IEEE. 2021, pp. 2290–2292.

[26] Abdulaziz SR Bati, Yu Lin Zhong, Paul L Burn, Mohammad Khaja Nazeeruddin, Paul E Shaw, and Munkhbayar Batmunkh. "Next-generation applications for integrated perovskite solar cells". *Communications Materials* 4.1 (2023), 2.

[27] *Best Research-Cell Efficiency Chart*. `https://www.nrel.gov/pv/cell-efficiency.html`. Accessed on: 11/07/2024. National Renewable Energy Laboratory (NREL), 2024.

[28] Zhibin Yang, Adharsh Rajagopal, and Alex K-Y Jen. "Ideal bandgap organic–inorganic hybrid perovskite solar cells". *Advanced Materials* 29.47 (2017), 1704418.

[29] Nir Kedem, Thomas M Brenner, Michael Kulbak, Norbert Schaefer, Sergiu Levcenko, Igal Levine, Daniel Abou-Ras, Gary Hodes, and David Cahen. "Light-induced increase of electron diffusion length in a p–n junction type $CH_3NH_3PbBr_3$ perovskite solar cell". *The journal of physical chemistry letters* 6.13 (2015), 2469–2476.

[30] Silver-Hamill Turren-Cruz, Michael Saliba, Matthew T Mayer, Hector Juarez-Santiesteban, Xavier Mathew, Lea Nienhaus, Wolfgang Tress, Matthew P Erodici, Meng-Ju Sher, Moungi G Bawendi, et al. "Enhanced charge carrier

mobility and lifetime suppress hysteresis and improve efficiency in planar perovskite solar cells". *Energy & Environmental Science* 11.1 (2018), 78–86.

[31] Zhenyuan Wu, Xin Xu, Yujia Gao, Zhengli Lu, Yating Cai, Yating Qu, Ang Li, Xi Huang, Weiwei Meng, Tingting Shi, et al. "Remarkable stability and optoelectronic properties of an all-inorganic $CsSn_{0.5}Ge_{0.5}I_3$ perovskite solar cell". *The Journal of Physical Chemistry Letters* 14.1 (2023), 302–309.

[32] Shanshan Zhang, Martin Stolterfoht, Ardalan Armin, Qianqian Lin, Fengshuo Zu, Jan Sobus, Hui Jin, Norbert Koch, Paul Meredith, Paul L Burn, et al. "Interface engineering of solution-processed hybrid organohalide perovskite solar cells". *ACS applied materials & interfaces* 10.25 (2018), 21681–21687.

[33] EL Unger, Lukas Kegelmann, K Suchan, D Sorell, Lars Korte, and Susanne Albrecht. "Roadmap and roadblocks for the band gap tunability of metal halide perovskites". *Journal of Materials Chemistry A* 5.23 (2017), 11401–11409.

[34] Nicolae Filipoiu, Tudor Luca Mitran, Dragos Victor Anghel, Mihaela Florea, Ioana Pintilie, Andrei Manolescu, and George Alexandru Nemnes. "Investigation of opto-electronic properties and stability of mixed-cation mixed-halide perovskite materials with machine-learning implementation". *Energies* 14.17 (2021), 5431.

[35] George Alexandru Nemnes, Cristina Besleaga, Viorica Stancu, Daniela Emilia Dogaru, Lucia Nicoleta Leonat, Lucian Pintilie, Kristinn Torfason, Marjan Ilkov, Andrei Manolescu, and Ioana Pintilie. "Normal and inverted hysteresis in perovskite solar cells". *The Journal of Physical Chemistry C* 121.21 (2017), 11207–11214.

[36] Yongbo Yuan, Zhengguo Xiao, Bin Yang, and Jinsong Huang. "Arising applications of ferroelectric materials in photovoltaic devices". *J. Mater. Chem. A* 2 (2014), 6027–6041.

[37] Alessandro Stroppa, Claudio Quarti, Filippo De Angelis, and Silvia Picozzi. "Ferroelectric Polarization of $CH_3NH_3PbI_3$: A Detailed Study Based on Density Functional Theory and Symmetry Mode Analysis". *The Journal of Physical Chemistry Letters* 6.12 (2015), 2223–2231.

[38] Zhen Fan, Juanxiu Xiao, Kuan Sun, Lei Chen, Yating Hu, Jianyong Ouyang, Khuong P. Ong, Kaiyang Zeng, and John Wang. "Ferroelectricity of $CH_3NH_3PbI_3$ Perovskite". *The Journal of Physical Chemistry Letters* 6 (2015), 1155–1161.

[39] Jarvist M. Frost, Keith T. Butler, Federico Brivio, Christopher H. Hendon, Mark van Schilfgaarde, and Aron Walsh. "Atomistic Origins of High-Performance in Hybrid Halide Perovskite Solar Cells". *Nano Letters* 14 (2014), 2584–2590.

[40] G. A. Nemnes, C. Goehry, T. L. Mitran, Adela Nicolaev, L. Ion, S. Antohe, N. Plugaru, and A. Manolescu. "Band alignment and charge transfer in rutile-$TiO_2/CH_3NH_3PbI_{3-x}Cl_x$ interfaces". *Phys. Chem. Chem. Phys.* 17 (2015), 30417–30423. DOI: `10.1039/C5CP05466D`.

[41] Tudor Luca Mitran, Rachel Elizabeth Brophy, Marina Cuzminschi, Nicolae Filipoiu, Movaffaq Kateb, Ioana Pintilie, Andrei Manolescu, and George Alexandru Nemnes. "Ab initio studies on perovskites". *Low-Dimensional Halide Perovskites*. Elsevier, 2023, pp. 153–185.

[42] Zhaosheng Zhang, Wei-Hai Fang, Run Long, and Oleg V. Prezhdo. "Exciton Dissociation and Suppressed Charge Recombination at 2D Perovskite Edges: Key Roles of Unsaturated Halide Bonds and Thermal Disorder". *Journal of the American Chemical Society* 141 (2019), 15557–15566.

[43] Zhaosheng Zhang, Wei-Hai Fang, Marina V. Tokina, Run Long, and Oleg V. Prezhdo. "Rapid Decoherence Suppresses Charge Recombination in Multi-Layer 2D Halide Perovskites: Time-Domain Ab Initio Analysis". *Nano Letters* 18 (2018), 2459–2466.

[44] E. A. Muljarov, S. G. Tikhodeev, N. A. Gippius, and Teruya Ishihara. "Excitons in self-organized semiconductor/insulator superlattices: PbI-based perovskite compounds". *Phys. Rev. B* 51 (1995), 14370–14378.

[45] Bat-El Cohen, Malgorzata Wierzbowska, and Lioz Etgar. "High Efficiency and High Open Circuit Voltage in Quasi 2D Perovskite Based Solar Cells". *Advanced Functional Materials* 27 (2017), 1604733.

[46] Carmen Ortiz-Cervantes, Paulina Carmona-Monroy, and Diego Solis-Ibarra. "Two-Dimensional Halide Perovskites in Solar Cells: 2D or not 2D?" *ChemSusChem* 12.8 (2019), 1560–1575. DOI: `https://doi.org/10.1002/cssc.201802992`. eprint: `https://chemistry-europe.onlinelibrary.wiley.com/doi/pdf/10.1002/cssc.201802992`. URL: `https://chemistry-europe.onlinelibrary.wiley.com/doi/abs/10.1002/cssc.201802992`.

[47] Zhaosheng Zhang, Wei-Hai Fang, Run Long, and Oleg V Prezhdo. "Exciton dissociation and suppressed charge recombination at 2D perovskite edges: key roles of unsaturated halide bonds and thermal disorder". *Journal of the American Chemical Society* 141.39 (2019), 15557–15566.

[48] Lingling Mao, Rhys M Kennard, Boubacar Traore, Weijun Ke, Claudine Katan, Jacky Even, Michael L Chabinyc, Constantinos C Stoumpos, and Mercouri G Kanatzidis. “Seven-layered 2D hybrid lead iodide perovskites”. *Chem* 5.10 (2019), 2593–2604.

[49] Calin-Andrei Pantis Simut, Alaa Allosh, Amanda Teodora Preda, Mihaela Cosinschi, Nicolae Filipoiu, and George Alexandru Nemnes. “Enhancing Biomarker Detection Using Artificial Neural Networks”. *2023 International Conference on Advanced Scientific Computing (ICASC)*. IEEE. 2023, pp. 1–5.

[50] Inas Bouzateur, Mohammed Assam Ouali, Hamza Bennacer, Mohamed Ladjal, Fadoua Khmaissia, Mohd Amiruddin Abd Rahman, and Abdelkader Boukortt. “Perovskite lattice constant prediction framework using optimized artificial neural network and fuzzy logic models by metaheuristic algorithms”. *Materials Today Communications* 37 (2023), 107021.

[51] Rafael S. Sanchez, Victoria Gonzalez-Pedro, Jin-Wook Lee, Nam-Gyu Park, Yong Soo Kang, Ivan Mora-Sero, and Juan Bisquert. “Slow Dynamic Processes in Lead Halide Perovskite Solar Cells. Characteristic Times and Hysteresis”. *The Journal of Physical Chemistry Letters* 5 (2014), 2357–2363.

[52] E. L. Unger, E. T. Hoke, C. D. Bailie, W. H. Nguyen, A. R. Bowring, T. Heumuller, M. G. Christoforo, and M. D. McGehee. “Hysteresis and transient behavior in current–voltage measurements of hybrid-perovskite absorber solar cells”. *Energy Environ. Sci.* 7 (2014), 3690–3698.

[53] Ajay Kumar Jena and Tsutomu Miyasaka. “Hysteresis characteristics and device stability”. *Organic-Inorganic Halide Perovskite Photovoltaics: From Fundamentals to Device Architectures* (2016), 255–284.

[54] W. Tress, N. Marinova, T. Moehl, S. M. Zakeeruddin, Mohammad Khaja Nazeeruddin, and M. Gratzel. “Understanding the rate-dependent J–V hysteresis, slow time component, and aging in $CH_3NH_3PbI_3$ perovskite solar cells: the role of a compensated electric field”. *Energy Environ. Sci.* 8 (2015), 995–1004.

[55] Jarvist M. Frost, Keith T. Butler, and Aron Walsh. “Molecular ferroelectric contributions to anomalous hysteresis in hybrid perovskite solar cells”. *APL Materials* 2 (2014), 081506.

[56] Jing Wei, Yicheng Zhao, Heng Li, Guobao Li, Jinlong Pan, Dongsheng Xu, Qing Zhao, and Dapeng Yu. “Hysteresis Analysis Based on the Ferroelectric

Effect in Hybrid Perovskite Solar Cells". *The Journal of Physical Chemistry Letters* 5 (2014), 3937–3945.

[57] Jin-Wook Lee, Seul-Gi Kim, Sang-Hoon Bae, Do-Kyoung Lee, Oliver Lin, Yang Yang, and Nam-Gyu Park. "The Interplay between Trap Density and Hysteresis in Planar Heterojunction Perovskite Solar Cells". *Nano Letters* 17 (2017), 4270–4276.

[58] Emilio J. Juarez-Perez, Rafael S. Sanchez, Laura Badia, Germa Garcia-Belmonte, Yong Soo Kang, Ivan Mora-Sero, and Juan Bisquert. "Photoinduced Giant Dielectric Constant in Lead Halide Perovskite Solar Cells". *The Journal of Physical Chemistry Letters* 5 (2014), 2390–2394.

[59] Isaac Zarazua, Juan Bisquert, and Germa Garcia-Belmonte. "Light-Induced Space-Charge Accumulation Zone as Photovoltaic Mechanism in Perovskite Solar Cells". *The Journal of Physical Chemistry Letters* 7 (2016), 525–528.

[60] Stephan van Reenen, Martijn Kemerink, and Henry J. Snaith. "Modeling Anomalous Hysteresis in Perovskite Solar Cells". *The Journal of Physical Chemistry Letters* 6 (2015), 3808–3814.

[61] Giles Richardson, Simon E. J. OKane, Ralf G. Niemann, Timo A. Peltola, Jamie M. Foster, Petra J. Cameron, and Alison B. Walker. "Can slow-moving ions explain hysteresis in the current–voltage curves of perovskite solar cells?" *Energy Environ. Sci.* 9 (2016), 1476–1485.

[62] G. A. Nemnes, Cristina Besleaga, A. G. Tomulescu, Ioana Pintilie, L. Pintilie, K. Torfason, and A. Manolescu. "Dynamic electrical behavior of halide perovskite based solar cells". *Sol. Energy Mater. Sol. Cells* 159 (2017), 197–203.

[63] Sandheep Ravishankar, Osbel Almora, Carlos Echeverria-Arrondo, Elnaz Ghahremanirad, Clara Aranda, Antonio Guerrero, Francisco Fabregat-Santiago, Arie Zaban, Germa Garcia-Belmonte, and Juan Bisquert. "Surface Polarization Model for the Dynamic Hysteresis of Perovskite Solar Cells". *The Journal of Physical Chemistry Letters* 8 (2017), 915–921.

[64] Elnaz Ghahremanirad, Agustin Bou, Saeed Olyaee, and Juan Bisquert. "Inductive Loop in the Impedance Response of Perovskite Solar Cells Explained by Surface Polarization Model". *The Journal of Physical Chemistry Letters* 8 (2017), 1402–1406.

[65] D V Anghel, G A Nemnes, Ioana Pintilie, and A Manolescu. "Modelling J-V hysteresis in perovskite solar cells induced by voltage poling". *Physica Scripta* 94 (2019), 125809.

[66] N. E. Courtier, J. M. Foster, S. E. J. O'Kane, A. B. Walker, and G. Richardson. "Systematic derivation of a surface polarisation model for planar perovskite solar cells". *European Journal of Applied Mathematics* 30 (2019), 427–457.

[67] Antonio J. Riquelme, Karen Valadez-Villalobos, Pablo P. Boix, Gerko Oskam, Ivan Mora-Sero, and Juan A. Anta. "Understanding equivalent circuits in perovskite solar cells. Insights from drift-diffusion simulation". *Phys. Chem. Chem. Phys.* 24 (26 2022), 15657–15671.

[68] Daniel A. Jacobs, Heping Shen, Florian Pfeffer, Jun Peng, Thomas P. White, Fiona J. Beck, and Kylie R. Catchpole. "The two faces of capacitance: New interpretations for electrical impedance measurements of perovskite solar cells and their relation to hysteresis". *Journal of Applied Physics* 124 (2018), 225702.

[69] Davide Moia, Ilario Gelmetti, Phil Calado, William Fisher, Michael Stringer, Onkar Game, Yinghong Hu, Pablo Docampo, David Lidzey, Emilio Palomares, Jenny Nelson, and Piers R. F. Barnes. "Ionic-to-electronic current amplification in hybrid perovskite solar cells: ionically gated transistor-interface circuit model explains hysteresis and impedance of mixed conducting devices". *Energy Environ. Sci.* 12 (2019), 1296–1308.

[70] Agustin O. Alvarez, Ramon Arcas, Clara A. Aranda, Loengrid Bethencourt, Elena Mas-Marza, Michael Saliba, and Francisco Fabregat-Santiago. "Negative Capacitance and Inverted Hysteresis: Matching Features in Perovskite Solar Cells". *The Journal of Physical Chemistry Letters* 11 (2020), 8417–8423.

[71] Antonio Guerrero, Germa Garcia-Belmonte, Ivan Mora-Sero, Juan Bisquert, Yong Soo Kang, T. Jesper Jacobsson, Juan-Pablo Correa-Baena, and Anders Hagfeldt. "Properties of Contact and Bulk Impedances in Hybrid Lead Halide Perovskite Solar Cells Including Inductive Loop Elements". *The Journal of Physical Chemistry C* 120 (2016), 8023–8032.

[72] Firouzeh Ebadi, Nima Taghavinia, Raheleh Mohammadpour, Anders Hagfeldt, and Wolfgang Tress. "Origin of apparent light-enhanced and negative capacitance in perovskite solar cells". *Nature Communications* 10 (2019), 1574.

[73] Mohd Taukeer Khan, Peng Huang, Abdullah Almohammedi, Samrana Kazim, and Shahzada Ahmad. "Mechanistic origin and unlocking of negative capacitance in perovskites solar cells". *iScience* 24 (2021), 102024.

[74] Juan Bisquert and Antonio Guerrero. “Chemical Inductor”. *Journal of the American Chemical Society* 144 (2022), 5996–6009.

[75] Laura Munoz-Diaz, Alvaro J. Rosa, Agustin Bou, Rafael S. Sanchez, Beatriz Romero, Rohit Abraham John, Maksym V. Kovalenko, Antonio Guerrero, and Juan Bisquert. “Inductive and Capacitive Hysteresis of Halide Perovskite Solar Cells and Memristors Under Illumination”. *Frontiers in Energy Research* 10 (2022).

[76] Enrique Hernandez-Balaguera and Juan Bisquert. “Negative Transient Spikes in Halide Perovskites”. *ACS Energy Letters* 7 (2022), 2602–2610.

[77] Cedric Gonzales, Antonio Guerrero, and Juan Bisquert. “Transition from capacitive to inductive hysteresis: A neuron-style model to correlate I–V curves to impedances of metal halide perovskites”. *The Journal of Physical Chemistry C* 126.32 (2022), 13560–13578.

[78] Antonio Guerrero, Juan Bisquert, and Germa Garcia-Belmonte. “Impedance Spectroscopy of Metal Halide Perovskite Solar Cells from the Perspective of Equivalent Circuits”. *Chemical Reviews* 121 (2021), 14430–14484.

[79] Nicolae Filipoiu, Amanda Teodora Preda, Dragos-Victor Anghel, Roxana Patru, Rachel Elizabeth Brophy, Movaffaq Kateb, Cristina Besleaga, Andrei Gabriel Tomulescu, Ioana Pintilie, Andrei Manolescu, et al. “Capacitive and inductive effects in perovskite solar cells: The different roles of ionic current and ionic charge accumulation”. *Physical Review Applied* 18.6 (2022), 064087.

[80] Mihaela Cosinschi, Amanda Teodora Preda, Calin Pantis-Simut, Nicolae Filipoiu, Ioan Ghitiu, Mihnea Alexandru Dulea, Lucian Ion, Andrei Manolescu, and George Alexandru Nemnes. “Collective dynamics of Ca atoms encapsulated in C_{60} endohedral fullerenes”. *Physical Chemistry Chemical Physics* (2024).

[81] Alaa Allosh, Calin-Andrei Pantis-Simut, Nicolae Filipoiu, Amanda Teodora Preda, George Necula, Ioan Ghitiu, Dragos-Victor Anghel, Mihnea Alexandru Dulea, and George Alexandru Nemnes. “Tuning phosphorene and MoS_2 2D materials for detecting volatile organic compounds associated with respiratory diseases”. *RSC advances* 14.3 (2024), 1803–1812.

[82] Calin-Andrei Pantis-Simut, Amanda Teodora Preda, Nicolae Filipoiu, Alaa Allosh, and George Alexandru Nemnes. “Electric-field control in phosphorene-based heterostructures”. *Nanomaterials* 12.20 (2022), 3650.

[83] P. Hohenberg and W. Kohn. “Inhomogeneous Electron Gas”. *Phys. Rev.* 136 (3B Nov. 1964), B864–B871. DOI: `10.1103/PhysRev.136.B864`. URL: `https://link.aps.org/doi/10.1103/PhysRev.136.B864`.

[84] W. Kohn and L. J. Sham. “Self-Consistent Equations Including Exchange and Correlation Effects”. *Phys. Rev.* 140 (1965), A1133–A1138. DOI: `10.1103/PhysRev.140.A1133`.

[85] Attila Szabo and Neil S Ostlund. *Modern quantum chemistry: introduction to advanced electronic structure theory.* Courier Corporation, 2012.

[86] Erwin Schrodinger. “An undulatory theory of the mechanics of atoms and molecules”. *Physical review* 28.6 (1926), 1049.

[87] Llewellyn H Thomas. “The calculation of atomic fields”. *Mathematical proceedings of the Cambridge philosophical society.* Vol. 23. 5. Cambridge University Press. 1927, pp. 542–548.

[88] Enrico Fermi. “Un metodo statistico per la determinazione di alcune priorieta dellatome”. *Rend. Accad. Naz. Lincei* 6.602-607 (1927), 32.

[89] P. A. M. Dirac. “Note on Exchange Phenomena in the Thomas Atom”. *Mathematical Proceedings of the Cambridge Philosophical Society* 26.3 (1930), 376–385. DOI: `10.1017/S0305004100016108`.

[90] CF v Weizsacker. “Zur theorie der kernmassen”. *Zeitschrift fur Physik* 96.7 (1935), 431–458.

[91] Richard M Martin. *Electronic structure: basic theory and practical methods.* Cambridge university press, 2020.

[92] Roberto Peverati and Donald G Truhlar. “Improving the accuracy of hybrid meta-GGA density functionals by range separation”. *The Journal of Physical Chemistry Letters* 2.21 (2011), 2810–2817.

[93] Jochen Heyd, Gustavo E Scuseria, and Matthias Ernzerhof. “Hybrid functionals based on a screened Coulomb potential”. *The Journal of chemical physics* 118.18 (2003), 8207–8215.

[94] Aliaksandr V Krukau, Oleg A Vydrov, Artur F Izmaylov, and Gustavo E Scuseria. “Influence of the exchange screening parameter on the performance of screened hybrid functionals”. *The Journal of chemical physics* 125.22 (2006).

[95] Pablo Ordejon, Emilio Artacho, and Jose M. Soler. “Self-consistent order-N density-functional calculations for very large systems”. *Phys. Rev. B* 53 (16 Apr. 1996), R10441–R10444. DOI: `10.1103/PhysRevB.53.R10441`. URL: `https://link.aps.org/doi/10.1103/PhysRevB.53.R10441`.

[96] Pablo Ordejon, David A Drabold, Matthew P Grumbach, and Richard M Martin. “Unconstrained minimization approach for electronic computations that scales linearly with system size”. *Physical Review B* 48.19 (1993), 14646.

[97] Pablo Ordejon, David A Drabold, Richard M Martin, and Matthew P Grumbach. “Linear system-size scaling methods for electronic-structure calculations”. *Physical Review B* 51.3 (1995), 1456.

[98] Daniel Sanchez-Portal, Pablo Ordejon, Emilio Artacho, and Jose M Soler. “Density-functional method for very large systems with LCAO basis sets”. *International journal of quantum chemistry* 65.5 (1997), 453–461.

[99] Emilio Artacho, Jose-Maria Cela, Julian D. Gale, Alberto Garcia, Javier Junquera, Richard M. Martin, Pablo Ordejon, Nick Rubner Papior, Daniel Sanchez-Portal, and Jose M Soler. *SIESTA 4.1.5.* https://siesta-project.org. Open source, 2021.

[100] Burak Himmetoglu, Andrea Floris, Stefano De Gironcoli, and Matteo Cococcioni. “Hubbard-corrected DFT energy functionals: The LDA+ U description of correlated systems”. *International Journal of Quantum Chemistry* 114.1 (2014), 14–49.

[101] Alberto Garcia, Matthieu J Verstraete, Yann Pouillon, and Javier Junquera. “The psml format and library for norm-conserving pseudopotential data curation and interoperability”. *Computer Physics Communications* 227 (2018), 51–71.

[102] Vladimir I Anisimov, Jan Zaanen, and Ole K Andersen. “Band theory and Mott insulators: Hubbard U instead of Stoner I”. *Physical Review B* 44.3 (1991), 943.

[103] Kristian Berland and Per Hyldgaard. “Exchange functional that tests the robustness of the plasmon description of the van der Waals density functional”. *Physical Review B* 89.3 (2014), 035412.

[104] Max Dion, Henrik Rydberg, Elsebeth Schroder, David C Langreth, and Bengt I Lundqvist. “Van der Waals density functional for general geometries”. *Physical review letters* 92.24 (2004), 246401.

[105] Honghui Shang, Zhenyu Li, and Jinlong Yang. "Implementation of screened hybrid density functional for periodic systems with numerical atomic orbitals: Basis function fitting and integral screening". *The Journal of chemical physics* 135.3 (2011).

[106] Lucas Fernandez-Seivane, Miguel A Oliveira, Stefano Sanvito, and Jaime Ferrer. "On-site approximation for spin–orbit coupling in linear combination of atomic orbitals density functional methods". *Journal of Physics: Condensed Matter* 18.34 (2006), 7999.

[107] R Cuadrado and JI Cerda. "Fully relativistic pseudopotential formalism under an atomic orbital basis: spin–orbit splittings and magnetic anisotropies". *Journal of Physics: Condensed Matter* 24.8 (2012), 086005.

[108] William Dawson and Takahito Nakajima. "Massively parallel sparse matrix function calculations with NTPoly". *Computer Physics Communications* 225 (2018), 154–165.

[109] Mads Brandbyge, Jose-Luis Mozos, Pablo Ordejon, Jeremy Taylor, and Kurt Stokbro. "Density-functional method for nonequilibrium electron transport". *Physical Review B* 65.16 (2002), 165401.

[110] Giovanni Pizzi, Valerio Vitale, Ryotaro Arita, Stefan Blugel, Frank Freimuth, Guillaume Geranton, Marco Gibertini, Dominik Gresch, Charles Johnson, Takashi Koretsune, et al. "Wannier90 as a community code: new features and applications". *Journal of Physics: Condensed Matter* 32.16 (2020), 165902.

[111] Nick Papior. *sisl: v 0.12.2*. 2024. DOI: `10.5281/zenodo.597181`. URL: `https://doi.org/10.5281/zenodo.597181`.

[112] Hui-Seon Kim, In-Hyuk Jang, Namyoung Ahn, Mansoo Choi, Antonio Guerrero, Juan Bisquert, and Nam-Gyu Park. "Control of I–V hysteresis in $CH_3NH_3PbI_3$ perovskite solar cell". *The journal of physical chemistry letters* 6.22 (2015), 4633–4639.

[113] Sandheep Ravishankar, Saba Gharibzadeh, Cristina Roldan-Carmona, Giulia Grancini, Yonghui Lee, Maryline Ralaiarisoa, Abdullah M Asiri, Nobert Koch, Juan Bisquert, and Mohammad Khaja Nazeeruddin. "Influence of charge transport layers on open-circuit voltage and hysteresis in perovskite solar cells". *Joule* 2.4 (2018), 788–798.

[114] Pankaj Yadav, Silver-Hamill Turren-Cruz, Daniel Prochowicz, Mohammad Mahdi Tavakoli, Kavita Pandey, Shaik M Zakeeruddin, Michael Gratzel, Anders Hagfeldt, and Michael Saliba. "Elucidation of charge recombination and

accumulation mechanism in mixed perovskite solar cells". *The Journal of Physical Chemistry C* 122.27 (2018), 15149–15154.

[115] Kazuhiko Seki. "Equivalent circuit representation of hysteresis in solar cells that considers interface charge accumulation: Potential cause of hysteresis in perovskite solar cells". *Applied Physics Letters* 109.3 (2016).

[116] Pilar Lopez-Varo, Juan A Jimenez-Tejada, Manuel Garcia-Rosell, Sandheep Ravishankar, Germa Garcia-Belmonte, Juan Bisquert, and Osbel Almora. "Device physics of hybrid perovskite solar cells: theory and experiment". *Advanced Energy Materials* 8.14 (2018), 1702772.

[117] Wolfgang Tress, Nevena Marinova, Thomas Moehl, Shaik Mohammad Zakeeruddin, Mohammad Khaja Nazeeruddin, and Michael Gratzel. "Understanding the rate-dependent J–V hysteresis, slow time component, and aging in $CH_3NH_3PbI_3$ perovskite solar cells: the role of a compensated electric field". *Energy & Environmental Science* 8.3 (2015), 995–1004.

[118] Agustin Bou, Adam Pockett, Dimitrios Raptis, Trystan Watson, Matthew J Carnie, and Juan Bisquert. "Beyond impedance spectroscopy of perovskite solar cells: insights from the spectral correlation of the electrooptical frequency techniques". *The Journal of Physical Chemistry Letters* 11.20 (2020), 8654–8659.

[119] Aron Walsh, David O Scanlon, Shiyou Chen, XG Gong, and Su-Huai Wei. "Self-regulation mechanism for charged point defects in hybrid halide perovskites". *Angewandte Chemie* 127.6 (2015), 1811–1814.

[120] Sergiu Draguta, Siddharatha Thakur, Yurii V Morozov, Yuanxing Wang, Joseph S Manser, Prashant V Kamat, and Masaru Kuno. "Spatially nonuniform trap state densities in solution-processed hybrid perovskite thin films". *The journal of physical chemistry letters* 7.4 (2016), 715–721.

[121] Alex Niemegeers and Marc Burgelman. "Numerical modelling of ac-characteristics of CdTe and CIS solar cells". *Conference Record of the Twenty Fifth IEEE Photovoltaic Specialists Conference-1996*. IEEE. 1996, pp. 901–904.

[122] Marc Burgelman, Peter Nollet, and Stefaan Degrave. "Modelling polycrystalline semiconductor solar cells". *Thin solid films* 361 (2000), 527–532.

[123] Marc Burgelman, Koen Decock, Samira Khelifi, and Aimi Abass. "Advanced electrical simulation of thin film solar cells". *Thin solid films* 535 (2013), 296–301.

[124] Koen Decock, Pawel Zabierowski, and Marc Burgelman. “Modeling metastabilities in chalcopyrite-based thin film solar cells”. *Journal of Applied Physics* 111.4 (2012).

[125] Marc Burgelman and Jonas Marlein. “Analysis of graded band gap solar cells with SCAPS”. *Proceedings of the 23rd European Photovoltaic Solar Energy Conference, Valencia*. Citeseer. 2008, pp. 2151–2155.

[126] Stefaan Degrave, Marc Burgelman, and Peter Nollet. “Modelling of polycrystalline thin film solar cells: new features in SCAPS version 2.3”. *3rd World Conference onPhotovoltaic Energy Conversion, 2003. Proceedings of*. Vol. 1. IEEE. 2003, pp. 487–490.

[127] Siegfried Selberherr. *Analysis and simulation of semiconductor devices*. Springer Science & Business Media, 2012.

[128] Jose M Soler, Emilio Artacho, Julian D Gale, Alberto Garcia, Javier Junquera, Pablo Ordejon, and Daniel Sanchez-Portal. “The SIESTA method for ab initio order-N materials simulation”. *Journal of Physics: Condensed Matter* 14.11 (Mar. 2002), 2745. DOI: `10.1088/0953-8984/14/11/302`. URL: `https://dx.doi.org/10.1088/0953-8984/14/11/302`.

[129] David M Ceperley and Berni J Alder. “Ground state of the electron gas by a stochastic method”. *Physical review letters* 45.7 (1980), 566.

[130] Norman Troullier and Jose Luis Martins. “Efficient pseudopotentials for plane-wave calculations”. *Physical review B* 43.3 (1991), 1993.

[131] N Filipoiu, Anca G Mirea, Sarah Derbali, C-A Pantis-Simut, D-V Anghel, A Manolescu, Ioana Pintilie, Mihaela Florea, and GA Nemnes. “Optoelectronic and stability properties of quasi-2D alkylammonium based perovskites”. *Physical Chemistry Chemical Physics* 25.4 (2023), 3323–3331.

[132] Constantinos C Stoumpos, Duyen H Cao, Daniel J Clark, Joshua Young, James M Rondinelli, Joon I Jang, Joseph T Hupp, and Mercouri G Kanatzidis. “Ruddlesden–Popper hybrid lead iodide perovskite 2D homologous semiconductors”. *Chemistry of Materials* 28.8 (2016), 2852–2867.

[133] Alessandro Senocrate, Gee Yeong Kim, Michael Grätzel, and Joachim Maier. “Thermochemical stability of hybrid halide perovskites”. *ACS Energy Letters* 4.12 (2019), 2859–2870.

[134] Chris G Van de Walle and Jorg Neugebauer. “First-principles calculations for defects and impurities: Applications to III-nitrides”. *Journal of applied physics* 95.8 (2004), 3851–3879.

[135] Paul Pistor, Thomas Burwig, Carlo Brzuska, Bjorn Weber, and Wolfgang Franzel. “Thermal stability and miscibility of co-evaporated methyl ammonium lead halide ($MAPbX_3$, X= I, Br, Cl) thin films analysed by in situ X-ray diffraction”. *Journal of Materials Chemistry A* 6.24 (2018), 11496–11506.

[136] Bruno Brunetti, Carmen Cavallo, Andrea Ciccioli, Guido Gigli, and Alessandro Latini. “On the thermal and thermodynamic (in) stability of methylammonium lead halide perovskites”. *Scientific reports* 6.1 (2016), 1–10.

[137] Andrea Ciccioli and Alessandro Latini. “Thermodynamics and the intrinsic stability of lead halide perovskites $CH_{33}PbX_3$”. *The journal of physical chemistry letters* 9.13 (2018), 3756–3765.

[138] Lucie McGovern, Moritz H Futscher, Loreta A Muscarella, and Bruno Ehrler. “Understanding the stability of $MAPbBr_3$ versus $MAPbI_3$: suppression of methylammonium migration and reduction of halide migration”. *The journal of physical chemistry letters* 11.17 (2020), 7127–7132.

[139] Mantas Simenas, Sergejus Balciunas, Anna Gagor, Agnieszka Pieniazek, Kasper Tolborg, Martynas Kinka, Vytautas Klimavicius, Sarunas Svirskas, Vidmantas Kalendra, Maciej Ptak, et al. “Mixology of $MA_{1-x}EA_xPbI_3$ Hybrid Perovskites: Phase Transitions, Cation Dynamics, and Photoluminescence”. *Chemistry of Materials* 34.22 (2022), 10104–10112.

[140] Erkki Alarousu, Ahmed M El-Zohry, Jun Yin, Ayan A Zhumekenov, Chen Yang, Esra Alhabshi, Issam Gereige, Ahmed AlSaggaf, Anton V Malko, Osman M Bakr, et al. “Ultralong radiative states in hybrid perovskite crystals: compositions for submillimeter diffusion lengths”. *The journal of physical chemistry letters* 8.18 (2017), 4386–4390.

[141] Sajid Sajid, Salem Alzahmi, Imen Ben Salem, Jongee Park, and Ihab M Obaidat. “Inorganic hole transport materials in perovskite solar cells are catching up”. *Materials Today Energy* (2023), 101378.

[142] Cristina Besleaga, Laura Elena Abramiuc, Viorica Stancu, Andrei Gabriel Tomulescu, Marian Sima, Liliana Trinca, Neculai Plugaru, Lucian Pintilie, George Alexandru Nemnes, Mihaiela Iliescu, et al. “Iodine migration and degradation of perovskite solar cells enhanced by metallic electrodes”. *The journal of physical chemistry letters* 7.24 (2016), 5168–5175.

[143] Gowri Manohari Arumugam, Santhosh Kumar Karunakaran, Chong Liu, Cuiling Zhang, Fei Guo, Shaohang Wu, and Yaohua Mai. “Inorganic hole transport layers in inverted perovskite solar cells: A review”. *Nano Select* 2.6 (2021), 1081–1116.

[144] Nicolae Filipoiu, Marina Cuzminschi, Calin-Andrei Pantis-Simut, Kristinn Torfason, Rachel Elizabeth Brophy, Andrei Manolescu, Roxana E Patru, Cristina Besleaga, George E Stan, Ioana Pintilie, et al. “Impact of interface defects on the band alignment and performance of TiO_2/MAPI/Cu_2O perovskite solar cells”. *arXiv preprint arXiv:2406.19594* (2024).

[145] Zhanhong Ma, Fengzhang Ren, Zhouya Yang, and Alex A Volinsky. “Theoretical and experimental studies on electronic structure and optical properties of Bi-doped anatase TiO2”. *Optik* 241 (2021), 167107.

[146] Raphael Shirley, Markus Kraft, and Oliver R Inderwildi. “Electronic and optical properties of aluminium-doped anatase and rutile TiO_2 from ab initio calculations”. *Physical Review B—Condensed Matter and Materials Physics* 81.7 (2010), 075111.

[147] Markus Heinemann, Bianca Eifert, and Christian Heiliger. “Band structure and phase stability of the copper oxides Cu_2O, CuO, and Cu_4O_3”. *Physical Review B—Condensed Matter and Materials Physics* 87.11 (2013), 115111.

[148] Wan-Jian Yin, Ji-Hui Yang, Joongoo Kang, Yanfa Yan, and Su-Huai Wei. “Halide perovskite materials for solar cells: a theoretical review”. *Journal of Materials Chemistry A* 3.17 (2015), 8926–8942.

[149] George Alexandru Nemnes, Cristina Besleaga, Andrei Gabriel Tomulescu, Alexandra Palici, Lucian Pintilie, Andrei Manolescu, and Ioana Pintilie. “How measurement protocols influence the dynamic JV characteristics of perovskite solar cells: Theory and experiment”. *Solar Energy* 173 (2018), 976–983.

[150] George Alexandru Nemnes, Cristina Besleaga, Andrei Gabriel Tomulescu, Lucia Nicoleta Leonat, Viorica Stancu, Mihaela Florea, Andrei Manolescu, and Ioana Pintilie. “The hysteresis-free behavior of perovskite solar cells from the perspective of the measurement conditions”. *Journal of Materials Chemistry C* 7.18 (2019), 5267–5274.

[151] Fuchang Gao and Lixing Han. “Implementing the Nelder-Mead simplex algorithm with adaptive parameters”. *Computational Optimization and Applications* 51.1 (2012), 259–277.

[152] Anca G. Mirea, Ioana D. Vlaicu, Sarah Derbali, Florentina Neatu, Andrei G. Tomulescu, Cristina Besleaga, Monica Enculescu, Andrei C. Kuncser, Alexandra C. Iacoban, Nicolae Filipoiu, Marina Cuzminschi, George A. Nemnes, Andrei Manolescu, Mihaela Florea, and Ioana Pintilie. *Electron transporting bilayers for perovskite solar cells: spray coating deposition of c-TiO_2/m-SnO_2-*

quantum dots. 2024. arXiv: `2406.18261 [physics.app-ph]`. URL: `https://arxiv.org/abs/2406.18261`.

[153] Boer Tan, Sonia R Raga, Kevin James Rietwyk, Jianfeng Lu, Sebastian O Furer, James C Griffith, Yi-Bing Cheng, and Udo Bach. “The impact of spiro-OMeTAD photodoping on the reversible light-induced transients of perovskite solar cells”. *Nano Energy* 82 (2021), 105658.

[154] Mahananda Baro and Parijat Borgohain. “SCAPS-1D device simulation of highly efficient perovskite solar cells using diverse charge transport layers”. *Journal of Electronic Materials* 52.11 (2023), 7623–7644.